Characterization and optimization of laser cooling of an atomic ensemble for a quantum memory

Anthony C. Leung

A thesis submitted for the degree of
Bachelor of Science with Honours in Physics of
The Australian National University

October, 2016

Declaration

This thesis is an account of research undertaken between February 2016 and October 2016 at The Department of Physics, Faculty of Science, The Australian National University, Canberra, Australia.

Except where acknowledged in the customary manner, the material presented in this thesis is, to the best of my knowledge, original and has not been submitted in whole or part for a degree in any university.

Anthony C. Leung
October, 2016

Acknowledgements

It has been a great Honours year where I have learnt a great deal from working with amazing people and it was great fun every step of the way.

I would like to first thank my supervisor Ben Buchler for giving me this opportunity to work on the GEM project. The support and advice I have received from him the past year was incredibly valuable including the many suggestions you have made after proof reading this thesis. It has been the most enjoyable and educational experience working in the GEM team with Geoff Campbell, Aaron Tranter and Jesse Everett. I can't thank Geoff enough for always being there to answer my numerous questions and I have learnt a lot from his technical expertise. Thanks to Aaron and his tireless work on programming the digital system, my project was able to progress smoothly and rapidly.

Everyone in the quantum optics group has been the most welcoming and I must thank you all for making this hectic year great fun. Ping Koy, none of this would be possible without your tireless support for all of us. To Ruvi and Siobhan, whom I share an office with, our regular conversations on just about everything was a necessary distraction that I was grateful for.

I must thank everyone who has helped me over my past few years as an undergraduate at ANU including all my friends and everyone I have met from the Physics department. In particular, special thanks to Jong Chow for all the help and advice he gave me over the last few years.

I would like to thank my parents for their unconditional support for me to pursue my interests. Finally, thank you to Emily who has been a great source of support during this time.

Abstract

Quantum memories are essential to many quantum information processing systems like the quantum repeater which is required to achieve long distance quantum communications. The quantum memory scheme of interest, Gradient echo memory, stores optical quantum information in an inhomogeneously broadened ensemble of atoms which leads to high bandwidth and efficiency. To improve both the efficiency and storage lifetime of this memory the rubidium-87 atoms used as the medium are prepared at cryogenic temperatures through laser cooling and trapping. The goal of this thesis is to characterize and to better understand the cooling and trapping processes and thereby optimize the ensemble preparation sequence to improve the system's performance as a quantum memory.

Firstly, the necessary theory to understanding the relevant laser cooling and trapping techniques like optical molasses, magneto-optical trap and polarization gradient cooling was presented. This included theory on atomic fine and hyperfine structure, Zeeman shifts, the optical Bloch equations and the scattering and dipole forces.

The experimental procedure for preparing the necessary beams and magnetic fields used to prepare the rubidium atoms was discussed along with the absorption imaging system used to measure the density and temperature of the atoms. Using this system, a time dependent model for the cross sectional intensity profile of the absorption images was obtained and used to extract the temperature of the atoms from images of the cloud's free expansion. By performing parameter sweeps on the trapping frequency detuning and repump intensity in the steady state magneto-optical trap configuration, the temperature was observed to have strong dependence on the trapping frequency; the more red detuned the beam was, the lower the temperatures at the cost of lower cloud density. At a frequency detuning of -41 MHz, the atoms reached temperatures of 253 ± 4 μK. At smaller detunings below -20 MHz, radiation trapping was dominant and caused dynamic instabilities. The repump intensity improved the cloud density by increasing it at low intensities but it was quickly found to have saturated its transition at 5 mW/cm^2 and changing it above that had little effect on the atoms. Using these observations, changes were made to the original cooling and trapping sequence and its temperature was measured to be 0.20 ± 0.05 mK. Significant improvement in the temperature was not really observed compared to previous sequences but it was likely due to the more aggressive compression now used to create a denser cloud.

Finally, coherent emission from the trapped cloud in the axial direction was observed and characterized. Its frequency was determined to be the same as the trapping frequency which suggested that the atoms formed an atomic density grating which coherently scattered light from the trapping beams. By retro-reflecting the emission from one direction back through the cloud, large oscillations in the emission power was observed. There is no conclusion as to the mechanism behind these oscillations but it is hypothesized to be a result of competition between heating and cooling processes.

Contents

List of Figures

Chapter 1

Introduction and motivation

1.1 Introduction to quantum information systems

Modern day information communications and processing are dominated by digital systems and protocols. Digital information had provided the ideal platform for accelerating technological development on faster and faster processors which vastly increased the size of data sets that could be manipulated and improving both the speed and reliability of communications. However, as development of these systems start to slow down, new ideas have emerged taking advantage of quantum mechanics to achieve results theoretically unachievable using digital systems.

Some of the more prominent examples are quantum computation [1] and quantum communications [2]. Quantum computers, in theory, are significantly more powerful than any known information processing system and can be used to simulate other quantum systems directly which is not possible with digital systems. The key advantage quantum communications has over digital is that information can be transmitted completely securely; no eavesdropping can happen undetected. For both of these devices, much of their development have been made using optical systems since optical quantum states like single photon states and entangled photon states can be easily created. In addition, photons offer the ideal medium of communications as they are fast and may be transmitted over long distances with minimal loss.

Unlike in digital systems, long distance optical quantum communications are not as straightforward. For digital signals to be successfully transmitted, the only real requirement is that at the other end of communications, an appreciable pulse in light is resolved. If the distances are so long such that only noise gets to the other end, optical amplification may be used to boost the signal. For a digital signal, this process introduces very little noise but for an optical quantum state, such processes cannot be used as even that tiny amount of noise will still change the quantum state and thereby altering the information being sent. This demonstrates how delicate quantum states are; not only does any measurement on the state collapses it, any sort of losses in transmission will affect and change the state.

One of the proposed solutions to this issue is to place a source of entangled photons between the sender and the receiver [3]. The source sends the two entangled photons in opposite directions towards the two ends of communications where both the sender and receiver make a measurement on their photon's quantum state. They would know if they had measured the photon in the same basis and over many successful measurements in the same basis, an encryption key may be generated. This key would then allow for secure communications between them. To solve the issue of transmitting quantum states over long distances, one may divide up the distance into segments that are separated by nodes.

Between these nodes, an entangled photon source will be placed and these photons will be sent to the nodes where quantum repeaters [4] will be placed. Bell measurements will be made at these nodes between photons from different entangled states to push the quantum state repeatedly from one end of communications to the other.

To many quantum information devices, like the quantum repeater, a quantum memory is an useful if not essential piece to the system [5]. A quantum memory, as its name suggests, is a system that allows the storage and preservation of quantum states. Unlike digital memories, measurement of the state and then recording the result is not a feasible method. Working with delicate quantum states brings about many difficulties. For example, long storage times are difficult to achieve as it requires the state to be well isolated from environmental disruptions to avoid changing the quantum state. To this date, a wide variety of quantum memory protocols have been proposed and demonstrated. From simple systems like an optical fibre delay line or optical cavities up to complex systems that offer control over the time of quantum state retrieval without severely compromising performance.

There are many aspects to a quantum memory system that may be measured to determine its performance. Efficiency determines how many photons sent to the memory may then be retrieved when recalled. Storage times indicate how long quantum states may be stored without being lost. Having a large bandwidth to make it compatible with pulses with a spectrum of frequency components can also be desirable. Some of the most successful schemes in these categories, like electromagnetically-induced transparency, have used atoms as the storage medium just like the system of interest in this thesis: Gradient echo memory (GEM). A detailed discussion of GEM can be found in chapter 5.

1.2 Thesis outline

A key component to GEM is in the preparation of the atomic ensemble. To improve the memory's performance both in efficiency and storage times, the system is operated in cryogenic temperatures on the order of a few hundred μK. The goal of this thesis is to improve the understanding and to optimize the cooling and trapping procedures used to prepare the atoms for quantum memory experiments. Firstly, necessary theory to understanding the mechanism of the trapping and cooling techniques used are presented. Next, a literature review of some of the existing cold atom quantum memory systems is provided along with a brief discussion of their strengths and weaknesses. Information on how to set up a magneto-optical trap and the absorption imaging system used to measure properties of the cloud of atoms is detailed next. By sweeping various parameters of the system, attempts to optimize the cooling and trapping processes is described and the results suggested that lower temperatures in the trap could be achieved by increasing the detuning of the trapping beam from the trapping transition at the expense of the density of the cloud. Control over the density could also be achieved at low intensities of the repump beam. Finally, a brief investigation into an axial coherent emission from the cloud is presented. It demonstrated that the trapped atoms formed an optical lattice which coherently scattered light from the trapping beams. It did not seem to have a strong effect on the temperature or density of the cloud but further investigations are required to understand its influence.

Chapter 2

Atomic structure

The Rutherford gold foil experiment was one of the real first steps into the development of the atomic model that is known today. His experiment showed that atoms were consisted of mostly empty space with matter concentrated into charged small dense particles [6]. Rutherford initially proposed the orbital model where the particles moved in orbital motion around each other but it was classically unstable as it implies the orbiting electrons will constantly radiate out energy and spiral into the nucleus. This problem was solved when Bohr proposed the quantized atomic model where he suggested the electrons can only occupy certain discrete orbits stably [7]. They can only change orbits by absorbing or radiating energy of the precise energy difference between the orbits. This however, failed to explain some of spectral emission lines observed from Hydrogen. As a result, many corrections to the Bohr model have been made ever since.

To understand the cooling and trapping mechanism well, it is important to first have a brief understanding of atomic structure. This section will explain the Bohr model and its major corrections; relativistic correction, spin-orbit interaction and the Darwinian correction lead to the fine structure model. Further inclusion of the spin of nucleons result in the hyperfine structure. The Zeeman effect is also touched upon as it is needed to explain how the magneto-optical trap works later and is part of the mechanics central to the Gradient Echo memory system this experiment is built for.

2.1 Bohr atom

The Hamiltonian of the one electron Bohr atom is quite simple:

$$\mathcal{H}_{atom} = \frac{p^2}{2\mu} - \frac{Ze^2}{4\pi\epsilon_0 r} \quad . \tag{2.1}$$

The first term is the kinetic energy of combined electron and nucleus with reduced mass μ and the second term is the Coulomb potential due to the nucleus with charge Z. p is the relative momentum of the atom in the centre of mass frame, e is the charge of the electron, r is the radial distance from the center of the nucleus. The Schrodinger equation in spherical coordinates, $\mathcal{H}_{atom}\Psi(r,\theta,\phi) = E\Psi(r,\theta,\phi)$ where E are the energy eigenvalues, can be solved through separation of variables to give solutions of the form $\Psi_{nlm}(r,\theta,\phi) = R_{nl}(r)Y_l^m(\theta,\phi)$; detailed solutions can be found in [8]. $R_{nl}(r)$ are the radial solutions made up of the Laguerre polynomials while $Y_l^m(\theta,\phi)$ are the spherical harmonics. $n \in \mathbb{N}$ is the principle quantum number, l is the orbital angular momentum quantum number ($0 \leq l \leq n-1$) and m is the magnetic quantum number ($-l \leq m \leq l$).

Solving for the energy eigenvalues give

$$E_n = -\frac{Z^2 e^4 \mu}{(4\pi\epsilon_0)^2 2\hbar^2 n^2} \quad . \tag{2.2}$$

Note how E_n is independent of both l and m. This means for each atomic energy level of the Bohr atom, there are n^2 degenerate eigenstates.

2.2 Fine structure

The relativistic correction, spin-orbit interaction and Darwinian correction combined causes the eigenstates in the Bohr model to lose degeneracy which gives rise to the fine structure. The derivations for this section follow the treatment in [9].

2.2.1 Relativistic correction

The first correction is made towards the electron's kinetic energy to account for its relativistic motion. The relativistic kinetic energy of the electron of mass m is

$$KE_{rel} = \sqrt{p^2c^2 + m^2c^4} - mc^2 \quad . \tag{2.3}$$

This expression can be expanded with respect to p to give a first order correction to $\mathcal{H}_{atom}$,

$$\mathcal{H}_{rel} = -\frac{p^4}{8m^3c^2} \quad . \tag{2.4}$$

Treating this correction as a perturbation, the resulting correction to the energy eigenvalues is derived to be

$$\delta E_{rel} = \langle \Psi_{nlm} | \mathcal{H}_{rel} | \Psi_{nlm} \rangle = E_n \frac{\alpha^2}{n^2} \left(\frac{n}{l + 1/2} - \frac{3}{4} \right) \quad , \tag{2.5}$$

where $\alpha = \frac{e^2}{4\pi\epsilon_0 \hbar c}$ is the fine structure constant.

2.2.2 Spin-orbit interaction

Electrons have intrinsic angular momentum called spin which is determined by the spin quantum number, $s = 1/2$. This means that the electron has an intrinsic magnetic moment that may interact with the magnetic field generated by its own orbital motion. This is called the spin-orbit interaction. To correct $\mathcal{H}_{atom}$ for this effect, the interaction energy between the intrinsic magnetic dipole moment, $\vec{\mu}$, and magnetic field, $\vec{B}$ is

$$\mathcal{H}_{SO} = -\vec{\mu} \cdot \vec{B} = \frac{1}{2m^2c^2} \frac{Ze^2}{4\pi\epsilon_0 r^3} \mathcal{L} \cdot \mathcal{S} \quad , \tag{2.6}$$

where $\mathcal{L}$ and $\mathcal{S}$ are the orbital angular momentum and spin angular momentum operators respectively. To solve for the correction to the energy eigenvalues, it is useful to introduce the total angular momentum operator $\mathcal{J} = \mathcal{L} + \mathcal{S}$. The total angular momentum quantum number, $j = l \pm s$, can take all the possible angular momentum values resulting from the combination of the orbital and spin angular momentum so $|l - s| \leq j \leq l + s$. This is useful because the dot product in the Hamiltonian can be expressed as $\mathcal{L} \cdot \mathcal{S} = \frac{1}{2}\left(\mathcal{J}^2 - \mathcal{L}^2 - \mathcal{S}^2\right)$.

The energy correction is then

$$\delta E_{SO} = \left\langle \Psi_{nljm_j} \right| \mathcal{H}_{SO} \left| \Psi_{nljm_j} \right\rangle = -E_n \frac{(Z^2\alpha^2)(j(j+1) - l(l+1) - 3/4)}{2nl(l+1/2)(l+1)} \quad . \tag{2.7}$$

2.2.3 Darwinian correction

The Darwin correction only affects $l = 0$ orbits that have a non-zero wavefunction at the nucleus and smears out the electrostatic potential experienced by the electron due to quantum fluctuations. There is no classical counterpart to this correction. The correction energy is directly quoted from [9] to be

$$\delta E_D = -E_n \frac{Z^2\alpha^2}{n} \quad . \tag{2.8}$$

2.2.4 Combined corrections

Summing all the energy corrections to find the energy of each fine structure level gives

$$E_{nj} = E_n \left(1 + \frac{Z^2\alpha^2}{n^2} \left(\frac{n}{j+1/2} - \frac{3}{4} \right) \right) \quad . \tag{2.9}$$

Clearly, after these corrections, the energy of each eigenstate only depends on the principle and total angular momentum quantum number, n and j. Fine structure levels are typically labeled with the convention $n^{2s+1}l_j$ where l is written in spectroscopic notation so $l = 0$ gives S, $l = 1$ gives P, etc. Examples of this are shown when rubidium-87 fine structure is discussed later.

2.3 Hyperfine structure

The origin of the hyperfine structure is similar to the spin-orbit interaction but this time, it is due to the coupling between the total angular momentum $\mathcal{J}$ with the nuclear angular momentum $\mathcal{I}$. $\mathcal{I}$ is similarly due to the spin of the nucleons. Therefore, the same formulation can be done to derive the hyperfine structure. Defining the total atomic angular momentum as $\mathcal{F} = \mathcal{J} + \mathcal{I}$. The value of the corresponding total atomic angular momentum quantum number, F, can be $|j - I| \leq F \leq j + I$. The interaction energy of this coupling gives the Hamiltonian

$$\mathcal{H}_{hf} = A_{hf} \mathcal{I} \cdot \mathcal{J} + B_{hf} \frac{3(\mathcal{I} \cdot \mathcal{J})^2 + \frac{3}{2}\mathcal{I} \cdot \mathcal{J} - I(I+1)j(j+1)}{2I(2I-1)j(2j-1)} \quad . \tag{2.10}$$

The hyperfine energy levels are then

$$E_{hf} = E_{nj} + \frac{1}{2} A_{hf} K + B_{hf} \frac{3K(K+1) - 4I(I+1)j(j+1)}{8I(2I-1)j(2j-1)} \quad , \tag{2.11a}$$

$$K = F(F+1) - I(I+1) - j(j+1) \quad . \tag{2.11b}$$

A_{hf} is the magnetic dipole constant and B_{hf} is the electric quadrupole constant; both of these can be found on data sheets. The detailed derivation can be found in [10].

2.4 Rubidium-87 atomic structure

The isotope of main interest in the rest of this thesis, Rubidium-87, is an alkali metal which means it only has one electron in its outermost $5s$ shell. Using both the fine and hyperfine structure described above, its energy structure may be examined as shown in Figure 2.1. For this experiment, there are two sets of transitions of interest. The first one is the D_1 transition from the $5^2S_{1/2}$ ground state to the $5^2P_{1/2}$ excited state. By the selection rules ($\Delta F = 0, \pm 1$), there are 4 possible transitions in this set. The D_1 transitions are mostly reserved for quantum memory purposes. The second set of transitions, D_2 is from the $5^2S_{1/2}$ ground state to the $5^2P_{3/2}$ excited state and has 6 possible hyperfine transitions. All the cooling and trapping are done in this set of transitions.

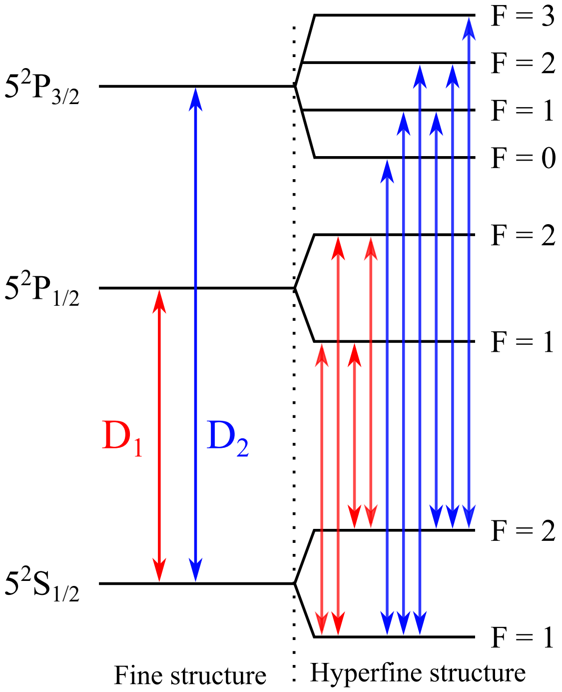

Figure 2.1: Fine and hyperfine structure for rubidium-87 and the transitions allowed by selection rules. Modified from [11].

2.5 Zeeman effect

The Zeeman effect is basically the breaking of energy degeneracy between magnetic sublevels of the same angular momentum quantum number (j for the fine structure and F for hyperfine) when the atom is in a magnetic field. The derivation for the energy shifts are analogous to what was done for the spin-orbit interaction where the total magnetic moment of the atom is taken to be

$$\mu_{atom} = -g_j \mu_B \mathcal{J} \tag{2.12a}$$

$$g_j = 1 + \frac{j(j+1) + s(s+1) - l(l+1)}{2j(j+1)} \quad , \tag{2.12b}$$

where μ_B is the Bohr magneton. Note the effect of nuclear spin has been ignored since it tends to be much smaller than electron spin. The interaction energy between the magnetic moment and an external magnetic field $\vec{B}_{ext}$ gives the Hamiltonian,

$$\mathcal{H}_B = g_j \mu_B \mathcal{J} \cdot \vec{B}_{ext} \tag{2.13}$$

By treating the magnetic field as weak so that this Hamiltonian can be treated as a perturbation [12], the Zeeman energy shift is given as

$$\delta E_B = g_F \mu_B B_{ext} M_F \tag{2.14a}$$

$$g_F = g_j \frac{F(F+1) + j(j+1) - I(I+1)}{2F(F+1)} \quad , \tag{2.14b}$$

where M_F is the hyperfine magnetic quantum number.

Chapter 3

Atom light interactions

This chapter develops and presents useful tools and results that are essential for appreciating how laser cooling and trapping works. The optical Bloch equations that describe the interaction between radiation and a two level atom semi-classically are derived from basic principles. From them, the Bloch vector and sphere are introduced which is a useful tool for understanding the mechanism behind Gradient Echo memory later. The steady state solutions to these equations which are important results used for laser cooling and trapping are also presented. Most of the derivations presented in this chapter are based off [12], [13] and [14].

3.1 Optical Bloch equations

The time dependent Schrodinger equation is

$$i\hbar\frac{\partial\Psi(\mathbf{r},t)}{\partial t} = \mathcal{H}\Psi(\vec{r},t) \quad . \tag{3.1}$$

For the two level atom, $\mathcal{H} = \mathcal{H}_0$ is the same atomic Hamiltonian as in equation 2.1 and $\Psi(\vec{r},t)$ is the time dependent wavefunction. Since this Hamiltonian is time independent, this equation has the known separable solutions of

$$\Psi_n(\vec{r},t) = \psi_n(\vec{r})e^{-iE_nt/\hbar} \quad , \tag{3.2}$$

where $n = 1$ and 2 for a two level atom. Substituting equation 3.2 into equation 3.1 gives the energy eigenvalue equations of

$$\mathcal{H}_0\psi_n(\vec{r}) = E_n\psi_n(\vec{r}) \quad . \tag{3.3}$$

Therefore, any arbitrary state that the atom can take can be represented as a superposition of these two atomic stationary states

$$\Psi(\vec{r},t) = c_1(t)\psi_1(\vec{r})e^{-i\omega_1 t} + c_2(t)\psi_2(\vec{r})e^{-i\omega_2 t} \quad , \tag{3.4}$$

where the time varying coefficients $c_n(t)$ are related to the probability of collapsing the system to either state when measured and $\omega_n = E_n/\hbar$.

So far, the above formulation applies to an unperturbed atom that has no interaction with its environment. It is now useful to introduce a perturbation resulting from interacting the atom with some electromagnetic radiation. A direct way to approach this is to first model the radiation as some monochromatic oscillating electric field of the form

$$\vec{E} = \vec{E}_0 \cos(\omega t) \tag{3.5}$$

where $\vec{E}_0$ is the oscillating amplitude and ω is the oscillation frequency. An atom in an electric field can be modelled as an electric dipole with dipole moment $\mathrm{e}\vec{r}$ where $\vec{r}$ is the displacement between the electron and the atomic center of mass. The interaction Hamiltonian of this perturbation is derived from the electric dipole's potential energy as

$$\mathcal{H}_I(t) = \mathrm{e}\vec{r} \cdot \vec{E}_0 \cos(\omega t) \tag{3.6}$$

Note that this assumes the wavelength of the electromagnetic radiation is much larger than the size of the atom such that the variations of the field are minor across the atom. This assumption is valid given the infrared range of frequencies relevant to this experiment.

The full Hamiltonian is then $\mathcal{H} = \mathcal{H}_0 + \mathcal{H}_I$. Using equation 3.1 with the two level atom solutions gives

$$i\hbar \left(\frac{dc_1}{dt}\Psi_1 + \frac{dc_2}{dt}\Psi_2 \right) = \mathcal{H}\left(c_1\Psi_1 + c_2\Psi_2\right) \tag{3.7}$$

Multiplying equation 3.7 with the complex conjugates of the wavefunctions, Ψ_1^* and Ψ_2^*, further reduces it down to two equations in Dirac notation

$$i\hbar\frac{dc_1}{dt} = c_1 \langle 1|\, \mathcal{H}_I \,|1\rangle + c_2 \langle 1|\, \mathcal{H}_I \,|2\rangle\, e^{-i\omega_0 t} \quad , \tag{3.8a}$$

$$i\hbar\frac{dc_2}{dt} = c_2 \langle 2|\, \mathcal{H}_I \,|2\rangle + c_1 \langle 2|\, \mathcal{H}_I \,|1\rangle\, e^{i\omega_0 t} \quad , \tag{3.8b}$$

where the Dirac notation represents $\langle i|\, \mathcal{H}_I \,|j\rangle = \int \Psi_i^* \mathcal{H}_I \Psi_j d\vec{r}^3$ and $\omega_0 = \omega_2 - \omega_1$. Note that when the positions of the nucleus and electrons are swapped, $\vec{r}$ is changed to $-\vec{r}$, the associated potential energy changes sign as well which means $\langle 1|\, \mathcal{H}_I \,|1\rangle$ and $\langle 2|\, \mathcal{H}_I \,|2\rangle$ are odd spatial functions so must equal zero. This result also implies $\langle 1|\, \mathcal{H}_I \,|2\rangle = \langle 2|\, \mathcal{H}_I \,|1\rangle^*$ given the two states are opposite in parity. Setting the polarization of the electromagnetic radiation to be polarized in the x axis such that

$$X_{12} = \langle 1|\, x \,|2\rangle \quad , \tag{3.9a}$$

$$\Omega = \frac{e|\vec{E}_0|X_{12}}{\hbar} \quad , \tag{3.9b}$$

where Ω is defined as the Rabi frequency. This allows simplification of equations 3.8 to a set of coupled differential equations:

$$i\frac{dc_1}{dt} = c_2 \Omega \cos(\omega t) e^{-i\omega_0 t} \quad , \tag{3.10a}$$

$$i\frac{dc_2}{dt} = c_1 \Omega^* \cos(\omega t) e^{i\omega_0 t} \quad . \tag{3.10b}$$

When analysing the two level atom, it is useful to work out the elements inside its atomic density matrix as given by equation 3.4:

$$|\Psi\rangle\langle\Psi| = \begin{pmatrix} |c_1|^2 & c_1c_2^* \\ c_2c_1^* & |c_2|^2 \end{pmatrix} = \begin{pmatrix} \rho_{11} & \rho_{12} \\ \rho_{21} & \rho_{22} \end{pmatrix} \quad . \tag{3.11}$$

The diagonal elements ρ_{11} and ρ_{22} are real values called the populations that indicate the fraction of the atoms in the ground and excited states respectively while the complex off diagonal elements are called the coherences. It is then simple to derive the equations of motion of the atomic system through the time derivatives of the density matrix elements,

$$\frac{d\rho_{ij}}{dt} = c_i\frac{dc_j^*}{dt} + \frac{dc_i}{dt}c_j^* \quad . \tag{3.12}$$

Substituting from equations 3.10, the equations of motion are:

$$\frac{d\rho_{22}}{dt} = -\frac{d\rho_{11}}{dt} = i\cos(\omega t)\left(\Omega\rho_{21}e^{-i\omega_0 t} - \Omega^*\rho_{12}e^{i\omega_0 t}\right) \quad , \tag{3.13a}$$

$$\frac{d\rho_{12}}{dt} = \frac{d\rho_{21}^*}{dt} = i\cos(\omega t)\Omega e^{-i\omega_0 t}\left(\rho_{11} - \rho_{22}\right) \quad . \tag{3.13b}$$

The fast oscillation terms may then be removed through the rotating wave approximation which assumes they average out to no contribution over the time scales of interest so the effects of the fast oscillating $\omega_0 + \omega$ terms can be ignored. Note that this approximation is only valid when close to resonance, $\omega \approx \omega_0$. Equations 3.13 then simplifies to

$$\frac{d\widetilde{\rho}_{22}}{dt} = -\frac{d\widetilde{\rho}_{11}}{dt} = \frac{i}{2}\left(\Omega\widetilde{\rho}_{21} - \Omega^*\widetilde{\rho}_{12}\right) \quad , \tag{3.14a}$$

$$\frac{d\widetilde{\rho}_{12}}{dt} = \frac{d\widetilde{\rho}_{21}^*}{dt} = \frac{i}{2}\Omega\left(\widetilde{\rho}_{11} - \widetilde{\rho}_{22}\right) + i(\omega_0 - \omega)\widetilde{\rho}_{12} \quad . \tag{3.14b}$$

The remaining oscillation terms were removed using rotating reference frame substitutions, $\widetilde{c}_1 = c_1e^{i(\omega_0-\omega)t/2}$ and $\widetilde{c}_2 = c_2e^{-i(\omega_0-\omega)t/2}$ where $\widetilde{\rho}_{ij} = \widetilde{c}_i\widetilde{c}_j^*$. The above set of 4 equations may be solved simultaneously with the initial conditions of $\rho_{11}(0) = 1$, $\rho_{22}(0) = 0$ and $\rho_{12}(0) = \rho_{21}(0) = 0$ to give the solutions of

$$\widetilde{\rho}_{22}(t) = \frac{|\Omega|^2}{W^2}\sin^2\left(\frac{Wt}{2}\right) \quad , \tag{3.15a}$$

$$\widetilde{\rho}_{12}(t) = \frac{\omega}{W^2}\sin\left(\frac{Wt}{2}\right)\left(iW\cos\left(\frac{Wt}{2}\right) - (\omega_0 - \omega)sin\left(\frac{Wt}{2}\right)\right) \quad , \tag{3.15b}$$

where $W^2 = \Omega^2 + (\omega_0 - \omega)^2$. The solutions indicate that the probability of exciting up to the excited state oscillates between zero and Ω^2/W^2. As the detuning between the transition and optical driving frequency reduces to zero, this probability can go up to 1. These are the Rabi oscillations.

Note from equations 3.10, with no driving optical field, they imply that the populations ρ_{11} and ρ_{22} stay constant which does not account for the decay of the excited state atoms via spontaneous emission. Clearly, the solutions in equations 3.15 only represent the Rabi oscillations but not the full physical picture as one would expect excited atoms to decay back to ground state over time through spontaneous emissions. To account for this, it is then necessary to introduce an exponential decay term such that with no driving field, the number of atoms in the excited state $N_2 = N\rho_{22}$ out of N atoms decays over time with a decay rate of Γ,

$$N_2(t) = N_2(0)e^{-\Gamma t} \quad . \tag{3.16}$$

This effect may then be included into equations 3.14 to give the optical Bloch equations

$$\frac{d\widetilde{\rho}_{22}}{dt} = -\Gamma\widetilde{\rho}_{22} + \frac{i}{2}\left(\Omega\widetilde{\rho}_{21} - \Omega^*\widetilde{\rho}_{12}\right) \tag{3.17a}$$

$$\frac{d\widetilde{\rho}_{11}}{dt} = \Gamma\widetilde{\rho}_{22} - \frac{i}{2}\left(\Omega\widetilde{\rho}_{21} - \Omega^*\widetilde{\rho}_{12}\right) \tag{3.17b}$$

$$\frac{d\widetilde{\rho}_{12}}{dt} = \frac{i}{2}\Omega\left(\widetilde{\rho}_{11} - \widetilde{\rho}_{22}\right) + i(\omega_0 - \omega)\widetilde{\rho}_{12} - \frac{\Gamma}{2}\widetilde{\rho}_{12} \tag{3.17c}$$

$$\frac{d\widetilde{\rho}_{21}}{dt} = -\frac{i}{2}\Omega^*\left(\widetilde{\rho}_{11} - \widetilde{\rho}_{22}\right) - i(\omega_0 - \omega)\widetilde{\rho}_{21} - \frac{\Gamma}{2}\widetilde{\rho}_{21} \tag{3.17d}$$

These are powerful equations that characterize the dynamics of the 2 level atomic system and have many applications.

3.2 Steady state solutions to Optical Bloch equations

In particular to the laser cooling and trapping processes discussed later, the steady state solutions to the Optical Bloch equations are an essential result. To find these, the time derivatives of equations 3.17 are equated to zero. It is also necessary to enforce conservation of number of atoms, $\rho_{11} + \rho_{22} = 1$, and to make use of the relation, $\rho_{12} = \rho_{21}^*$. The population difference is defined as $w = \rho_{11} - \rho_{22} = 1 - 2\rho_{22}$. Even though Ω is in general a complex quantity, when Ψ_1 and Ψ_2 are real wavefunctions of bound states like in real atomic levels, it can be treated as a real number. The Optical Bloch equations then simplify to

$$\frac{dw}{dt} = \frac{d\widetilde{\rho}_{11}}{dt} - \frac{d\widetilde{\rho}_{22}}{dt} = i\Omega\left(\widetilde{\rho}_{12} - \widetilde{\rho}_{12}^*\right) + \Gamma(1 - w) \quad , \tag{3.18a}$$

$$\frac{d\widetilde{\rho}_{12}}{dt} = \frac{i}{2}\Omega w - \left(i\delta + \frac{\Gamma}{2}\right)\widetilde{\rho}_{12} \quad , \tag{3.18b}$$

where $\delta = \omega - \omega_0$. Their solutions are

$$w = \frac{\delta^2 + \Gamma^2/4}{\delta^2 + \Omega^2/2 + \Gamma^2/4} \quad , \tag{3.19a}$$

$$\widetilde{\rho}_{12} = \frac{(\Omega/2)(\delta + i\Gamma/2)}{\delta^2 + \Omega^2/2 + \Gamma^2/4} \quad . \tag{3.19b}$$

The steady state population of the excited state is

$$\widetilde{\rho}_{22} = \frac{1 - w}{2} = \frac{\Omega^2/4}{\delta^2 + \Omega^2/2 + \Gamma^2/4} \quad . \tag{3.20}$$

3.3 Bloch vector and Bloch sphere

To introduce the Bloch vector, it is useful to first take a look at the electric dipole moment of an atom in an optical field. Keeping the assumption that the polarization is in the x

direction, the expectation value of the electric dipole moment, $p_x(t)$ is

$$p_x(t) = -\int \Psi^\dagger(t) \mathrm{e} x \Psi(t) d^3\vec{r} \quad . \tag{3.21}$$

This can be expanded and simplified using equations 3.4 and 3.9a to give

$$p_x(t) = -\mathrm{e}\left(c_2^* c_1 X_{12}^* e^{i\omega_0 t} + c_1^* c_2 X_{12} e^{-i\omega_0 t}\right) \quad . \tag{3.22}$$

Using the same reasoning for Ω in the previous section, X_{12} is also treated as a real number here. Also, the definition of the coherences from before are used to give

$$p_x(t) = -\mathrm{e}X_{12}\left(\widetilde{\rho}_{12} e^{i\omega t} + \widetilde{\rho}_{21} e^{-i\omega t}\right) = -\mathrm{e}X_{12}\left(u\cos(\omega t) + v\sin(\omega t)\right) \quad . \tag{3.23}$$

Therefore, introducing the in phase and out of phase components of the atomic dipole

$$u = \widetilde{\rho}_{12} + \widetilde{\rho}_{21} \quad , \tag{3.24a}$$

$$v = -i(\widetilde{\rho}_{12} - \widetilde{\rho}_{21}) \quad . \tag{3.24b}$$

This finally leads to the definition of the Bloch vector, $\vec{R}$:

$$\vec{R} = u\hat{e}_1 + v\hat{e}_2 + w\hat{e}_3 \quad , \tag{3.25a}$$

$$w = \rho_{11} - \rho_{22} \quad . \tag{3.25b}$$

where w is the population difference.

It can be shown that

$$\frac{d\vec{R}}{dt} = \vec{R} \times (\Omega\hat{e}_1 - \delta\hat{e}_3) = \vec{R} \times \vec{W} \quad . \tag{3.26}$$

Equation 3.26 shows that $\frac{d\vec{R}}{dt}$ is perpendicular to $\vec{R}$; the magnitude of $\vec{R}$ does not change. Therefore, this Bloch vector will always move on the surface of a sphere which is called the Bloch sphere while precessing around the $\vec{W}$ vector. Note the Bloch vector is a unit vector since its length must be 1 for the state $(u, v, w) = (0, 0, 1)$. This is shown in Figure 3.1.

When the Bloch vector points towards the poles, $\vec{R} = \pm\hat{e}_3$, the system is purely in states $|1\rangle$ and $|2\rangle$ correspondingly.

The Bloch sphere is a useful tool for describing the dynamics of any two state quantum system.

Also, equation 3.19b can be used to further derive the solutions to the in phase and out of phase components of the electric dipole moment which would be useful later,

$$u = \frac{\Omega\delta}{\delta^2 + \Omega^2/2 + \Gamma^2/4} \quad , \tag{3.27a}$$

$$v = \frac{\Omega\Gamma/2}{\delta^2 + \Omega^2/2 + \Gamma^2/4} \quad . \tag{3.27b}$$

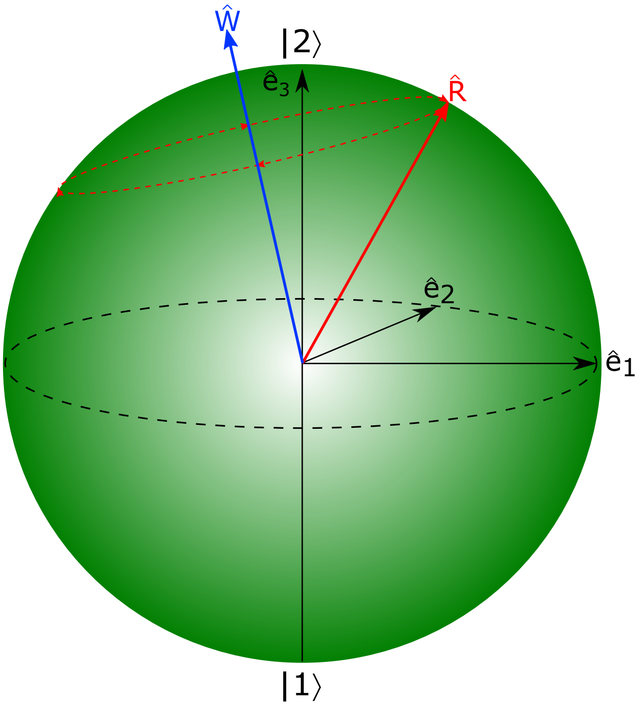

Figure 3.1: The Bloch sphere with the Bloch vector $\vec{R}$ which precesses around the $\vec{W}$ vector in the dotted trajectory over time. The two poles of the Bloch sphere represent the ground, $|1\rangle$, and excited, $|2\rangle$, states. Anywhere else along the surface of the sphere then represents a superposition of these two states.

Chapter 4

Laser cooling and trapping

To be able to slow down atoms in gases and thereby cooling their temperature to subkelvin level has proven to be a very powerful tool and has substantially improved the understanding in many areas of physics for the last few decades. For this particular experiment as a quantum memory, the atoms used are necessarily cooled and confined to vastly improve its performance.

This section provides some basic theory behind laser cooling and trapping of gaseous atoms by first introducing the dipole and scattering forces and from there work towards the magneto-optical trap and the polarization gradient cooling techniques used in this experiment.

4.1 Light forces

To understand the mechanism behind the forces that an atom experiences in an optical field, the induced electric dipole moment is examined again. This section was developed using the same method in [12]. The energy of an induced electric dipole is given as

$$U = \frac{1}{2}\mathrm{e}\vec{r}\cdot\vec{E} = -\frac{1}{2}\epsilon_0\chi_a E^2 \quad , \tag{4.1}$$

where a substitution for the dipole moment, $-\mathrm{e}\vec{r} = \epsilon_0\chi_a\vec{E}$, has been used. $\epsilon_0\chi_a$ is known as the polarizability of the atom. Equation 4.1 can be differentiated with respect to the z direction for the z component of the force:

$$F_z = -\frac{\partial U}{\partial z} = \epsilon_0\chi_a E\frac{\partial E}{\partial z} \quad . \tag{4.2}$$

Taking the electric field of the radiation to be of the form $\vec{E} = E_0\cos(\omega t - kz)\hat{x}$ such that it is polarized in the x direction, equation 4.2 then becomes

$$F_z = -eX_{12}\left(u\cos(\omega t) + v\sin(\omega t)\right)\times\left(\frac{\partial E_0}{\partial z}\cos(\omega t - kx) + kE_0\sin(\omega t - kz)\right) \quad . \tag{4.3}$$

The above expression was expanded using the electric dipole moment found in equation 3.23. The time average of this force over many oscillation periods is found by setting the $\sin(\omega t)\cos(\omega t)$ terms to zero and $\sin^2(\omega t) = \cos^2(\omega t) = 1/2$ to give

$$\bar{F_z} = \frac{-eX_{12}}{2}\left(u\frac{\partial E_0}{\partial z} - vkE_0\right) \quad . \tag{4.4}$$

The two terms in the brackets of equation 4.4 are known as the dipole and scattering force respectively. Their complete expressions are found using the solutions to u and v in equation 3.27 and the definition of the Rabi frequency in equation 3.9b:

$$F_{dip} = -\frac{\hbar\delta}{2}\frac{\Omega}{\delta^2+\Omega^2/2+\Gamma^2/4}\frac{\partial\Omega}{\partial z} \quad , \tag{4.5a}$$

$$F_{sca} = \frac{\hbar k\Gamma}{2}\frac{\Omega^2/2}{\delta^2+\Omega^2/2+\Gamma^2/4} \quad . \tag{4.5b}$$

These equations imply that in the x and y directions, there is no scattering force if the same derivation method is followed. The dependence of δ for both forces are plotted in Figure 4.1.

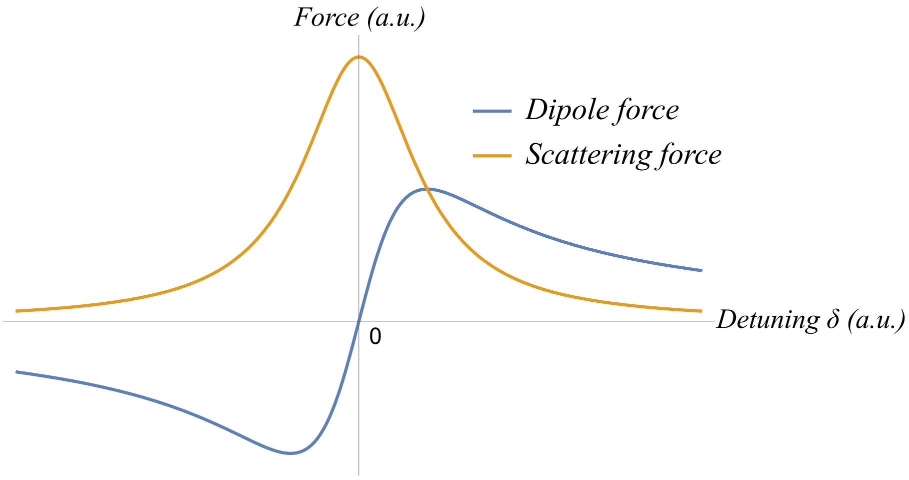

Figure 4.1: Dipole and scattering force as a function of detuning, δ.

4.1.1 Dipole force

With the inclusion of the interaction Hamiltonian, $\mathcal{H}_I$, the energy eigenvalues E_n in equation 3.3 are necessarily shifted. This shift of atomic energy levels in the presence of an optical field is called the AC Stark effect. The AC Stark effect for a two level atom causes the ground and excited energy levels, E_1 and E_2, to shift by

$$\Delta E_1 = -\Delta E_2 = \frac{\hbar\Omega^2}{4\delta} \tag{4.6}$$

Details on the rigorous derivation of the above result requires the use of the dressed states of the atom and are detailed in [14] and [15]. Note that this result is only true when $\Omega \ll |\delta|$ is true. This shift in energy level is illustrated in Figure 4.2.

From this, the atomic energy levels are clearly dependent on the intensity of the optical field through the relation

$$\frac{I}{I_{sat}} = \frac{2\Omega^2}{\Gamma^2} \quad , \tag{4.7}$$

where I and I_{sat} are the optical field intensity and transition saturation intensity respectively [12]. As a result, if the field does not have uniform intensity across space, the atomic energy levels vary in space which generates a dipole potential, U_{dip}. This dipole

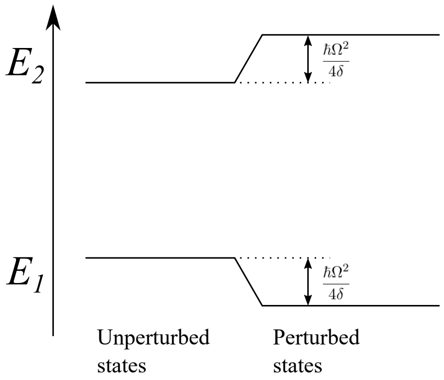

Figure 4.2: The shift in energy levels due to the AC Stark shift when atoms interact with radiation which perturbs the eigenstates.

potential is given by the light shift and equation 4.7 to be

$$U_{dip} = \frac{\hbar\Gamma^2 I}{8\delta I_{sat}} \quad . \tag{4.8}$$

If the optical field is red detuned to the atomic transition, an attractive potential is generated where atoms are attracted to locations of high optical intensity and vice versa for blue detuned fields. This is a very powerful tool for trapping atoms and when are formed into standing waves, an optical lattice may be generated. However, since this force is conservative, it cannot be used for cooling.

4.1.2 Scattering force

This part presents a somewhat more physically intuitive picture of the scattering force. When an atom absorbs a photon, by the conservation of momentum, its momentum has to change. The resultant force, F_{rad}, of this interaction is the rate of change of momentum this atom experiences that results from absorbing photons. The momentum of a photon is E/c where E is the energy of the photon. Therefore, the radiation force is given as

$$F_{rad} = \frac{I\sigma_{abs}}{c} \quad , \tag{4.9}$$

where σ_{abs} is absorption cross-section and I is the intensity of the optical field. The force strength on the atoms is the most significant close to a resonant transition where a photon is most likely to be absorbed as the maximum of σ_{abs} can be much larger than the size of the atom at resonant frequencies.

This force can be used to slow down atoms as demonstrated in Figure 4.3.

A laser beam is directed at the atom against its direction of motion. If the frequency of this laser is tuned close to one of the atom's transitions, it will then exert a force against its motion given in equation 4.9. Each absorption of a counter propagating photon will reduce the momentum of the atom. Since the spontaneous emission from the atom occurs randomly in all directions, the net momentum change from spontaneous emission averages to zero. This is the scattering force that the atom experiences over many absorption and emission events and slows it down.

Therefore ignoring the momentum contribution of the spontaneous emissions that av-

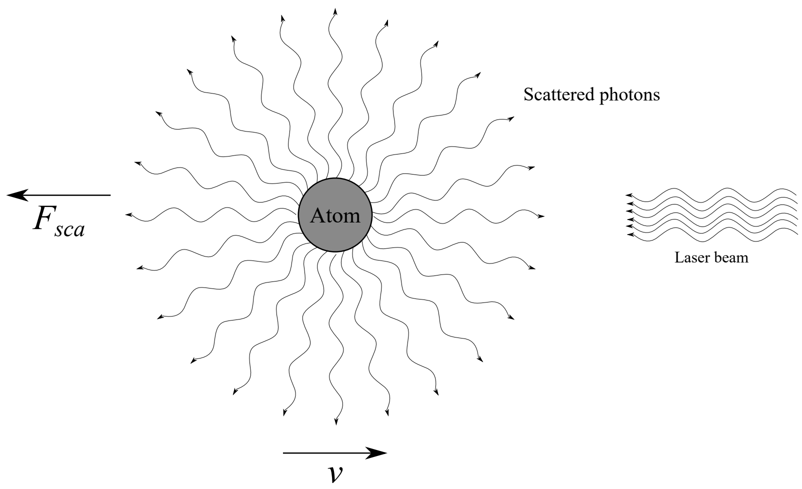

Figure 4.3: The atom has velocity v. It absorbs photons from the laser beam and then re-emits them randomly in all directions which results in a net force against the motion of the atom.

erage to zero, the force the atom experiences with each absorption of a photon is

$$F_{sca} = \hbar k \Gamma \rho_{22} \quad , \tag{4.10}$$

where $\hbar k$ is the momentum imparted onto the atom, Γ is the rate of this process and ρ_{22} is the probability the atom is in the excited state. This is consistent with the expression derived in equation 4.5b. The quantity $\Gamma\rho_{22}$ is also known as the scattering rate of light from the optical field, R_{scatt}.

Relating the optical field intensity with the Rabi frequency through equation 4.7 leads to

$$F_{sca} = \frac{\hbar k \Gamma}{2} \frac{I/I_{sat}}{1 + I/I_{sat} + 4\delta^2/\Gamma^2} \quad . \tag{4.11}$$

As the optical field intensity increases, the scattering force does not increase indefinitely; it approaches a limit of $\hbar k\Gamma/2$. This is a result of the limit in the probability of being in the excited state in a two level system; $\rho_{22} = 1/2$. For this force to work, the atoms must scatter photons out of the optical field and thereby dissipating energy from the system through spontaneous emission. Therefore, it is a very useful force for cooling atoms.

4.2 Optical Molasses

The scattering force is clearly an effective mechanism in slowing down atoms when configured appropriately. To maximize the scattering force against the atomic motion, it is necessary to take into account Doppler shift; if the atom is moving towards the beam, in the atom's frame, the light becomes blue shifted. From Figure 4.1, the scattering force is strongest at resonance; therefore, for maximum stopping force, it is necessary to set the laser frequency to be red detuned such that in the moving atom's frame it is on resonance.

Extending this concept such that the atom may be slowed in one dimension, it may be set up such that there are two counter propagating beams of the same intensity along the dimension of motion which forms a standing wave. If both of these beams are red detuned, it no longer matters which direction the atom moves in as it would be slowed in either directions. This is illustrated in Figure 4.4.

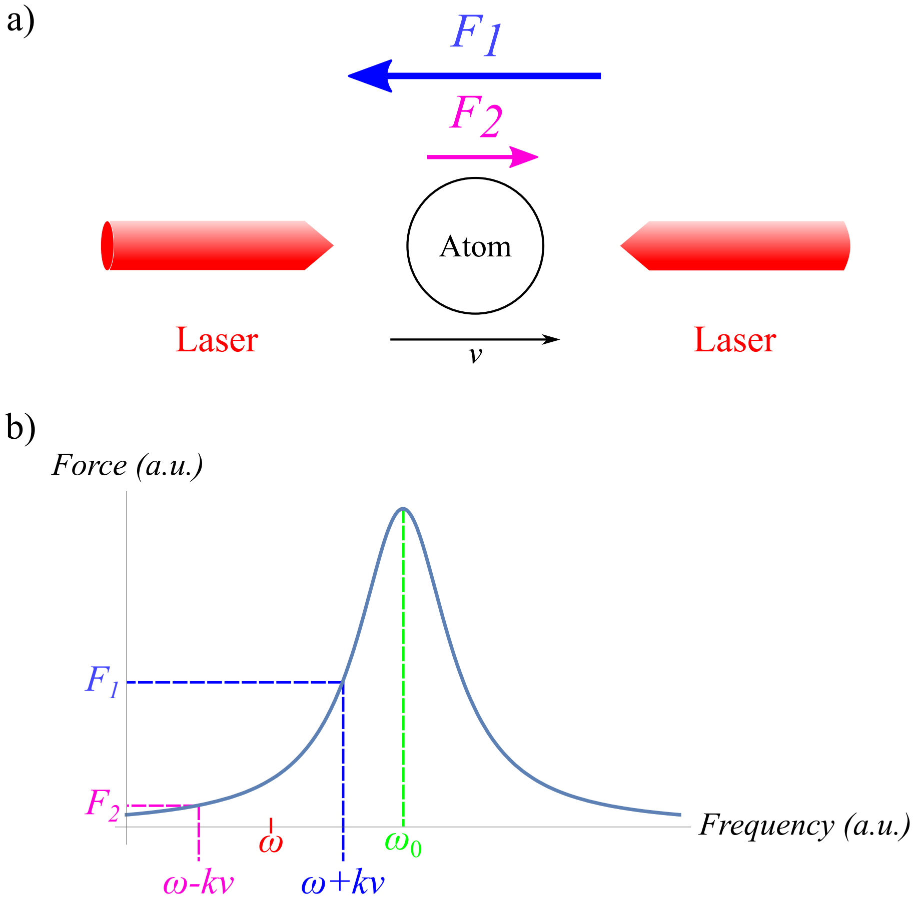

Figure 4.4: a)The atom has velocity v inside two counter propagating beams red detuned to the transition frequency, ω_0. b)In the atom's rest frame, the laser frequency, ω, is Doppler shifted to $\omega + kv$ and $\omega - kv$ for the two beams. The frequency of the laser pointing against the direction of motion is shifted closer towards resonance and thus exerts a larger scattering force, F_1, compared to the other laser, F_2. The resultant force opposes the motion of the atom.

The above phenomena can be expressed by finding the force a moving atom experiences when it is in an optical field that forms a standing wave. To do so, it is necessary to make corrections to the optical Bloch equations by including the effects of the atomic velocity. However, these equations cannot be solved analytically. It is sufficient to just make first order corrections to their solutions by treating the atomic velocity as a perturbation and this rigorous treatment can be found in [16]. Even though it is even a larger approximation, for simplicity, this perturbation is applied directly to the scattering force expression of equation 4.11 as follows.

The force applied by the standing wave formed by the two beams can be expressed by summing up the scattering force due to the both beams as a function of the Doppler shifted frequency detunings from equation 4.11. Firstly, the scattering force on an atom moving towards the beam at velocity v by first order correction from [12] is

$$F_1 = \frac{\hbar k\Gamma}{2}\frac{I/I_{sat}}{1+I/I_{sat}+4(\omega_0-(\omega+kv))^2/\Gamma^2} \simeq \frac{\hbar k\Gamma}{2}\frac{I/I_{sat}}{1+I/I_{sat}+4\delta^2/\Gamma^2}+kv\frac{\partial F}{\partial\omega} \quad (4.12)$$

The optical molasses force is then

$$\begin{aligned} F_{mol} &= F_2 - F_1 \\ &\simeq -2kv\frac{\partial F}{\partial\omega} \\ &\simeq \frac{8\hbar k^2\delta}{\Gamma\left(1+\frac{4\delta^2}{\Gamma^2}\right)^2}\frac{I}{I_{sat}}v = -\beta v \end{aligned} \quad (4.13)$$

where the approximation $I/Isat \ll 1$ was necessarily made because the above process needs the beam intensity to be low enough such that spontaneous emission can return the atoms into the ground state. Note that equation 4.13 is in the form of a frictional force where β is the damping coefficient. For F_{mol} to work against the movement of the atom, it is necessary for δ to be negative; the beams must be red detuned to the atomic transition as expected. This force as a function of velocity is plotted in Figure 4.5.

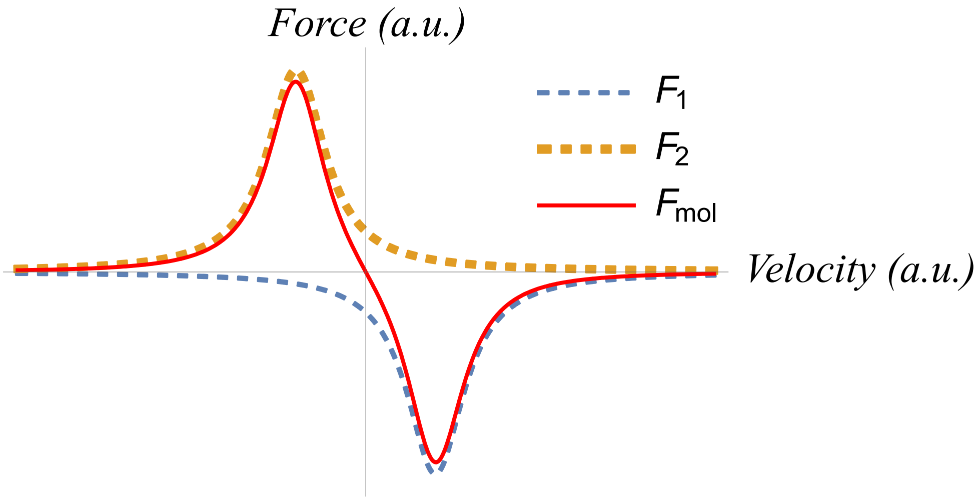

Figure 4.5: A plot of the force a one dimensional optical molasses arrangement has on an atom with respect to velocity. F_{mol} is a superposition of the force applied by each of the counter-propagating beams F_1 and F_2. F_{mol} will always work to decelerate the atoms.

The range of velocity, Δv of atoms that can be effectively cooled with this technique is approximately the natural linewidth of the excited state divided by the wavenumber

$$\Delta v = \frac{\Gamma}{k} \quad (4.14)$$

as this is the range of velocities in which the damping force is approximately linear. [17] In order to cool atoms in three dimensional space, the above discussion simply needs to be extended into using 3 pairs of orthogonal counter-propagating beams so the atoms may be cooled in all three directions. This is shown in Figure 4.6

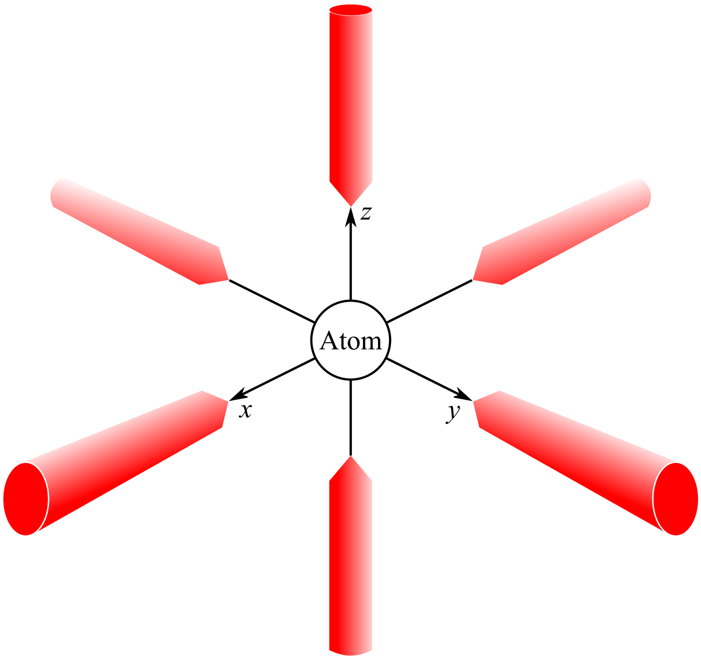

Figure 4.6: A three dimensional optical molasses configuration with 3 orthogonal pairs of counter propagating beams acting against all three components of the atom's velocity.

4.2.1 Doppler cooling limit

The above discussion implies that with enough time, the atoms irradiated by the 6 beams simultaneously will continuously cool until they reach absolute zero. This does not seem to be physical; there clearly is a temperature limit to which these atoms may be cooled down to. So far, the effects of spontaneous emission have been ignored as their contributions average to zero with the random emission direction. However, with each spontaneous emission, the atom actually gets a momentum kick in the opposite direction. Therefore, they are never completely stationary and has some fluctuation in their velocity; their mean squared velocity is non-zero. This is analogous to Brownian motion. As a result, the coldest temperature that this technique can achieve is determined by the equilibrium temperature where the cooling rate from the optical molasses and heating rate from spontaneous emissions are the same. This temperature is

$$T_{doppler} = \frac{\hbar\Gamma}{2k_B} \quad , \tag{4.15}$$

where k_B is Boltzmann's constant [17]. This is called the Doppler cooling limit for a two level atom of linewidth Γ.

4.3 Magneto-optical trap

With the 3 orthogonal beams on, the optical molasses technique will allow the accumulation of neutral atoms inside the intersection region over time as the atoms will have very low velocity inside. However, this is not a trap; the atoms will eventually diffuse out. In order for the system to actively trap the atoms, it is important to introduce a restoring force that actively keeps the atoms inside the trap.

The magneto-optical trap (MOT) is a simple extension of the optical molasses technique which just requires adding in a magnetic field gradient and choosing appropriate polarizations for the trapping laser beams. The magnetic field gradient can be generated using coils in an anti Helmholtz configuration where the current in the coils go in opposite directions and thereby generating a quadrupole magnetic field as illustrated in Figure 4.7. The magnetic field generated this way is useful because the field at the center is zero and, when close to the center, the field strength increases linearly in all directions.

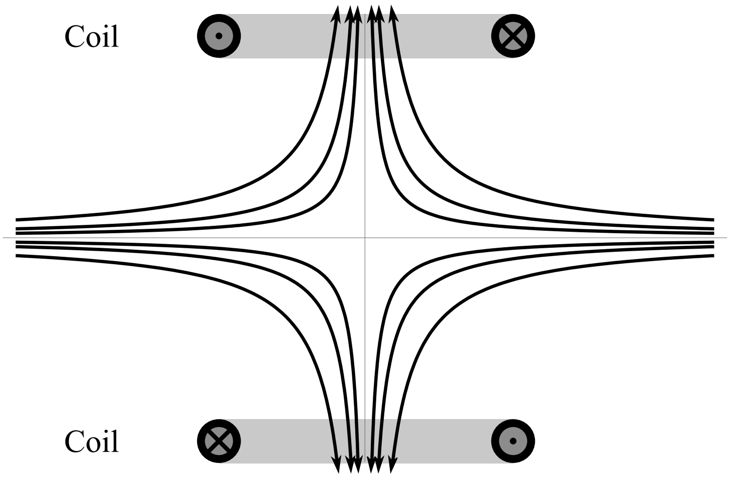

Figure 4.7: Quadrupole magnetic field generated in the anti Helmholtz configuration where the current of the two coils flow in opposite directions.

As a result of this magnetic field gradient, atoms that are not at the center of this configuration experience an increasing Zeeman shift in their energy levels as they move away from the center.

For simplicity, an atom with two energy levels of $J = 0$ to $J = 1$ in one dimension is examined. As this atom is situated further from the center, where the magnetic field is zero, the magnetic field strength increases the energy level splitting between the $M_J = -1, 0, +1$ levels of the $J = 1$ level. This is clarified with Figure 4.8.

If the atom is to the right of the center, the energy of the $M_J = -1$ level moves below ω_0 and closer to resonance with ω. To push the atom back towards the center, the beam propagating leftwards is required to provide a restoring force while the other beam should have a minimal effect. To do this, the beam must satisfy the correct selection rules; it needs to have the correct circular polarization, σ_-, such that it can interact with the $J = 0$, $M_J = 0$ to $J = 1$, $M_J = -1$ transition. Of course, the atom still experiences a force from the counter-propagating σ_+ beam as that interacts with the $J = 0$, $M_J = 0$ to $J = 1$, $M_J = 1$ transition but it is much further detuned so the number of photons absorbed from this beam is lower than that from the σ_- beam. Therefore, there is an imbalance of scattering forces between the two beams when the atom is displaced from the center and this net resultant force acts as a restoring force. The opposite is true when the atom is displaced to the left of the center; the $M_J = 1$ level is now closer to resonance and, by the selection rules, it would scatter the right propagating beam more strongly which pushes it back towards the center. Since both counter-propagating beams are red detuned they not only trap the atom but also cools it via the same Doppler cooling mechanism described in the optical molasses section.

Note that this trapping mechanism is very similar to the optical molasses tech-

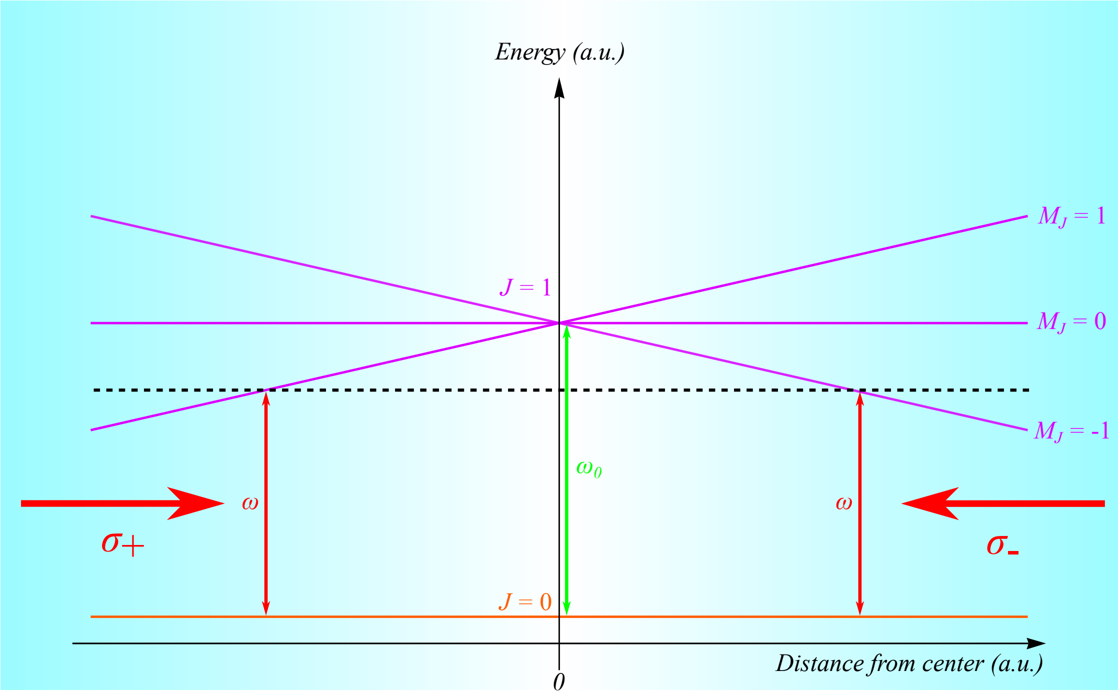

Figure 4.8: Energy levels of the atom with respect to the distance from the center of the MOT. The linear magnetic field gradient causes Zeeman splitting of the sublevels of the $J = 1$ level.

nique. Optical molasses is based on Doppler shifting the laser frequency of the counter-propagating beam closer to resonance with the atom's velocity while the MOT uses a magnetic field gradient and selection rules to ensure an atom not in the center interacts more strongly with the beam that would push it back to the center.

The damping force exerted on an atom by the MOT can be modelled by including the effects of the Zeeman shifts from equations 2.14 into the detuning in equations 4.12 and 4.13. In general, let the magnetic quantum number of the ground and excited state that are on resonance at position z away from the center of the MOT be M_1 and M_2 respectively. The effect of the Zeeman frequency shift in the atomic energy levels on the transition frequency is

$$\delta_B = \frac{(g_2 M_2 - g_1 M_1)\mu_B}{\hbar}\frac{dB}{dz}z \quad , \tag{4.16}$$

where $B(z)$ is the magnetic field as a function of position. The scattering force from the σ_- beam is then

$$\begin{aligned} F_{\sigma_-} &= \frac{\hbar k \Gamma}{2}\frac{I/I_{sat}}{1 + I/I_{sat} + 4((\omega_0 - \delta_B) - (\omega + kv))^2/\Gamma^2} \\ &\simeq \frac{\hbar k \Gamma}{2}\frac{I/I_{sat}}{1 + I/I_{sat} + 4\delta^2/\Gamma^2} + kv\frac{\partial F}{\partial \omega} - \delta_B\frac{\partial F}{\partial \omega_0} \end{aligned} \tag{4.17}$$

Evaluating the force the MOT applies to the atoms,

$$\begin{aligned}
F_{MOT} &= F_{\sigma_+} - F_{\sigma_-} \\
&\simeq -2kv\frac{\partial F}{\partial \omega} + 2\delta_B \frac{\partial F}{\partial \omega_0} \\
&\simeq -\beta v - \kappa z \qquad (4.18a) \\
\kappa &= \frac{\delta_B \beta}{k} \qquad (4.18b)
\end{aligned}$$

The first term in equation 4.18a represents the damping force identical to in optical molasses and the second term is the restoring force applied by the MOT. F_{MOT} describes the atoms to be in damped harmonic motion when inside a MOT. [12]

Similarly, the one dimensional discussion above can be extended to three dimensions with another two pairs of counter-propagating circularly polarized beams as shown in Figure 4.9.

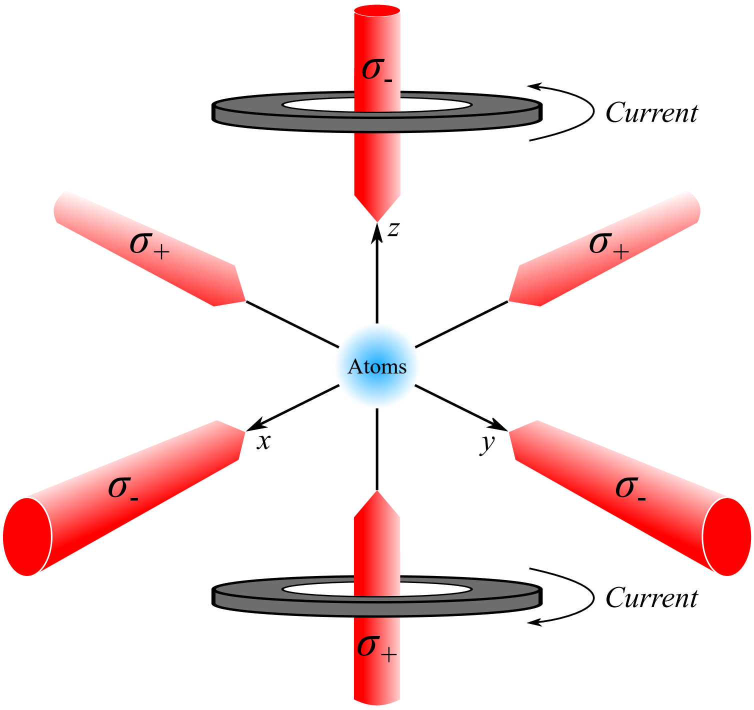

Figure 4.9: Basic schematic of a three dimensional magneto-optical trap. The anti-Helmholtz coils form a magnetic field gradient along with 3 pairs of counter propagating oppositely circular polarized trapping beams.

Any atoms that are irradiated simultaneously by all 6 beams would slow down and as they try to diffuse out of the interaction region, the restoring force brings them back to the center which effectively traps the atoms inside the MOT through damped harmonic motion. As a result, the MOT has a much larger velocity capture range compared to the optical molasses and can be used to directly trap and cool atoms from a cloud of atoms initially at room temperature. Therefore, the number of atoms accumulated in the intersection region is much higher too.

4.4 Sub-Doppler cooling

It is actually possible and has been demonstrated that cooling beyond the Doppler limit is achievable. The previous discussion of the Doppler limit is built upon summing the individual contributions of each of the 6 beams towards cooling the atoms. This treatment of the system neglects to account for the cooling resulting from the atoms being inside a pair of counter-propagating beams forming a standing wave. As explained in [17], this phenomena can be explained with optical pumping where the atomic population is forced to shift between atomic levels as the atoms travel through the standing wave. This technique is known as polarization-gradient cooling (PGC).

Similar to the optical molasses, PGC only requires 3 pairs of counter-propagating orthogonal beams. However, as its name implies, the beams are required to have specific polarization and they also need to be further red detuned to be effective. There are two sets of beam polarization configurations that are possible. The pair of two counter-propagating beams can either be linearly orthogonal or circularly orthogonal from each other. The linearly orthogonal case is also known as Sisyphus cooling. Despite achieving the same cooling efficiency, the two polarization configurations work on different mechanisms. An in depth model of both of these mechanisms can be found in [17].

The general procedure for preparing the atoms in this experiment involves gathering Rubidium atoms from room temperature into a cold dense cloud using the MOT. After which, the magnetic fields are switched off and the already circularly orthogonal polarized beams are further red detuned in the PGC phase to further cool the gas cloud. Therefore, for the purpose of this experiment, the rest of this section will briefly describe the mechanics of only the circularly polarized configuration of PGC.

4.4.1 Circularly polarized PGC

For simplicity, the system is first considered in a one dimensional configuration with a pair of counter-propagating σ_+ and σ_- beams. The electric field for the two beams combined can be expressed as

$$E_{st}(z) = E_0^+ e^{ikz}\epsilon_+ + E_0^- e^{-ikz}\epsilon_- \tag{4.19}$$

where E_0^+ and ϵ_+ are the electric field amplitude and polarization of the σ_+ beam respectively and similarly so for the σ_- beam. The circular polarizations of ϵ_+ and ϵ_- can be expressed in terms of the unit horizontal and vertical polarization vectors ϵ_x and ϵ_y

$$\epsilon_+ = -\frac{1}{\sqrt{2}}(\epsilon_x + i\epsilon_y) \tag{4.20a}$$

$$\epsilon_- = -\frac{1}{\sqrt{2}}(\epsilon_x - i\epsilon_y) \tag{4.20b}$$

Substituting equations 4.20 into 4.19 gives the electric field of the standing wave

$$E_{st}(z) = \frac{E_0^- - E_0^+}{\sqrt{2}}(\epsilon_x \cos(kz) - \epsilon_y \sin(kz)) - i\frac{E_0^- + E_0^+}{\sqrt{2}}(\epsilon_x \sin(kz) + \epsilon_y \cos(kz)) \tag{4.21}$$

From this expression, it can be seen that this standing wave can in fact be expressed as a sum of two fields with orthogonal polarizations in the linear polarization basis. The total electric field has an ellipticity of $(E_0^- - E_0^+)/(E_0^- + E_0^+)$. The axis of this ellipse rotates around the z axis depending on the position and wavelength through $\phi = -kz$. If the two counter-propagating beams have the same amplitude, the ellipticity will be zero and the electric field will always be purely linearly polarized. This linear polarization will rotate along the length of the standing wave axis forming a helix as shown in Figure 4.10.

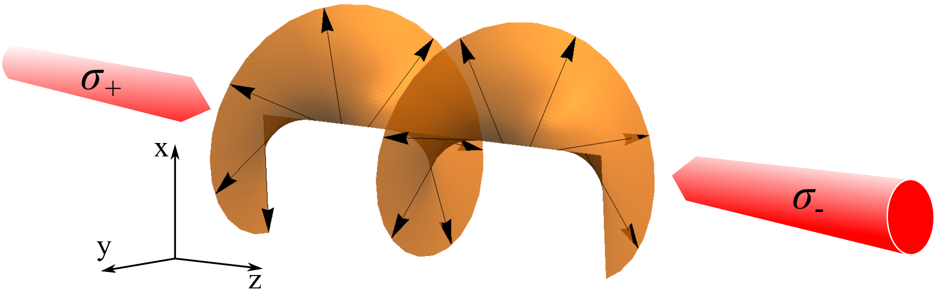

Figure 4.10: Polarization vector in space along the standing wave formed by two counter-propagating σ_+ and σ_- beams of the same amplitude.

First assume the atom is stationary in this optical field. The polarization at the atom's location can be taken as the quantization axis for the atom. For this experiment, assume the atom is a rubidium-87 atom and the two levels are the D2 transition $F = 1 \rightarrow F' = 2$ levels. For simplicity, the other hyperfine levels are ignored. The atomic structure and the Clebsh-Gordon coefficients of this level is drawn in Figure 4.11.

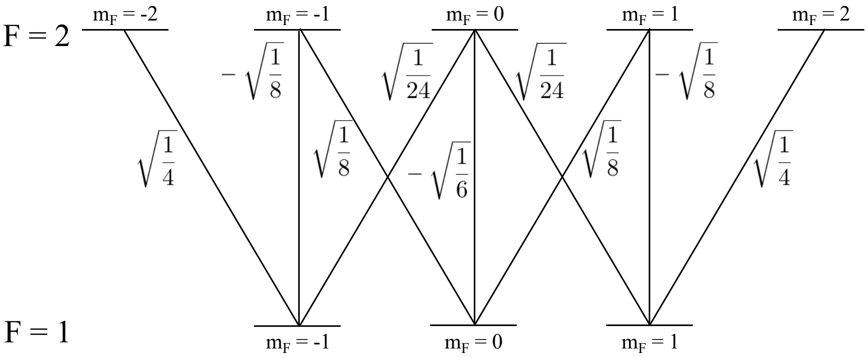

Figure 4.11: Rubidium-87 D2 $F = 1 \rightarrow F' = 2$ structure with the Clebsh-Gordon coefficients. These are from [11]. Note that the transition probabilities add up to $\frac{1}{4}$ here as the coefficients here also take into account the transitions to other hyperfine levels.

Given that with linearly polarized electric fields only π transitions ($\Delta m_F = 0$) can occur, atoms starting at the $F = 1$, $m_F = \pm 1$ levels are optically pumped into the $F = 1$, $m_F = 0$ state at a rate of $4 \times (-\sqrt{1/8})^2(\sqrt{1/8})^2 = 1/4$. The opposing optical pumping from the $m_F = 0$ state to the $m_F = \pm 1$ states have the rate of $4 \times (-\sqrt{1/6})^2(-\sqrt{1/24})^2 = 1/9$. Clearly, the population will start to accumulate in the $m_F = 0$ sublevel due to optical pumping. The steady state population of these three sublevels are $9/17$ for $m_F = 0$ and $4/17$ for $m_F = \pm 1$. These steady state population results are not position dependent; the same results will be derived no matter where along the z axis they were done. However, since the polarization direction changes with z, the quantization axis also changes with it. Therefore, the actual eigenstates are different. As an atom moves along the z axis, it can introduce couplings between the different sublevels.

It is shown in [17] that by examining the atom in its rest frame which also rotates along with the polarization direction so the atom experiences a constant polarization, one would find that there is an additional (imaginary) magnetic field in the z direction by applying Larmor's theorem. This field introduces a change in the Hamiltonian of the system and its effects have been analyzed as a perturbation to the system. The important final result of this is that the actual energy levels are not changed by this movement. However, the wave functions have been changed which results in a change in the steady state populations of the $m_F = \pm 1$ sublevels. This means that when the atoms move, they will experience optical pumping so they may follow the changing quantization axis.

For an atom moving towards the σ_- beam, the $m_F = -1$ state will be more populated than the $m_F = 1$ state. The difference in population is given as

$$\langle m_F = 1 \rangle - \langle m_F = -1 \rangle = \frac{40}{17}\frac{kv}{\delta} \quad , \tag{4.22}$$

where v is the velocity of the atom and δ is the detuning. From the Clebsh-Gordon coefficients, it can be seen that atoms in the $m_F = -1$ ground state interact with σ_- light much more efficiently than with σ_+. Also, the atoms will be trapped into the $F = 1$, $m_F = -1$ and $F = 2$, $m_F = -2$ transition as by selection rules, the atoms can only spontaneously decay back down to the $m_F = -1$ ground state from the $m_F = -2$ excited state. The opposite is true for the $m_F = 1$ ground state; it interacts with σ_+ light much more strongly. If there are now more atoms in the $m_F = -1$ ground state due to atomic motion, there will then be an imbalance of forces as the atom now scatters more light from the σ_- beam which will transfer momentum against its direction of motion. Therefore, a frictional force is generated.

The temperature of the PGC cooled sample is given as [14]

$$T_{PGC} = \frac{0.097}{k_B}\frac{\hbar\delta C^2}{1 + (2\delta/\Gamma)^2}\frac{I}{I_{sat}} \quad , \tag{4.23}$$

where C is the Clebsh-Gordon coefficient for the relevant cooling transition. The temperature of the sample may be minimized by reducing the laser intensity or increasing the detuning. Just like the case with Doppler cooling, this technique cannot reduce the temperature of the sample indefinitely; it is now limited by the momentum gained by the atom with spontaneous emissions. The minimum temperature [14], called the recoil limit, is achieved when PGC effects are balanced out by heating caused by spontaneous emission given as

$$T_r = \frac{(\hbar k)^2}{2k_B M} \tag{4.24}$$

Typically, this technique allows gas clouds to be cooled down to the order of microkelvins. There are methods available to cool the atoms even further below the recoil limit such as Raman cooling or evaporative cooling.

Chapter 5

Literature review on cold atom quantum memories

Quantum memory experiments have been performed on cryogenic solid state ensembles and cold and warm gas ensembles using a variety of storage protocols [5]. A recent review of various experiments in [18] shows that solid state systems have currently achieved the longest storage time [19] up to 1 minute. Furthermore, the performance of solid state systems has been improving and measurements have recently demonstrated coherence times up to six hours [20]. This implies that a six hour quantum memory for light is feasible, although this has yet to be demonstrated. Meanwhile, cold atom systems currently hold the highest efficiencies [18,21] of up to 96%. This chapter provides a brief literature review on various proposed cold atom quantum memory schemes.

5.1 Electromagnetically induced transparency

When the frequency of an optical field approaches that of the transition frequency of an atom, a resonance effect occurs as the interaction strength between them grows. The atom's response to a resonant field consists of a dissipative (absorption) and dispersive components. This response of a simple two level atom is shown in Figure 5.1.

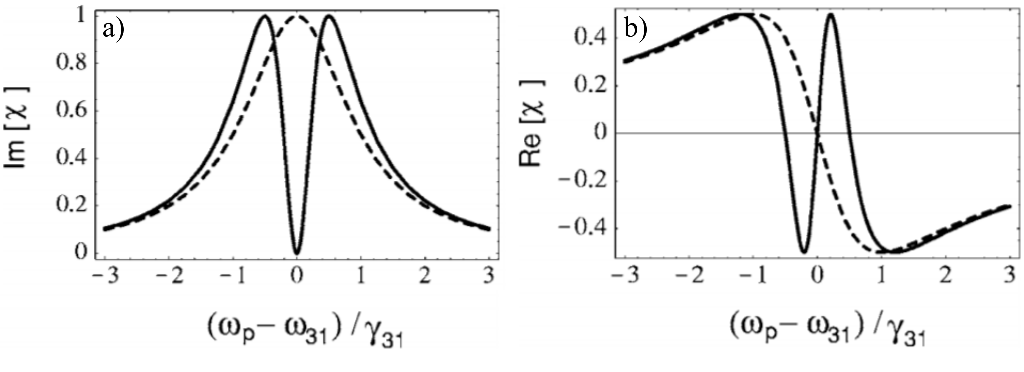

Figure 5.1: a) The absorption and b) dispersive (refractive index) response of the atom with respect to detuning from the transition frequency. Dashed line is the response of a simple two level atom and solid line is the response of an EIT system. Figure taken from [22].

When another optical field, called the control, that is resonant with a third state(Figure 5.2), is introduced, the optical response of the system is much different.

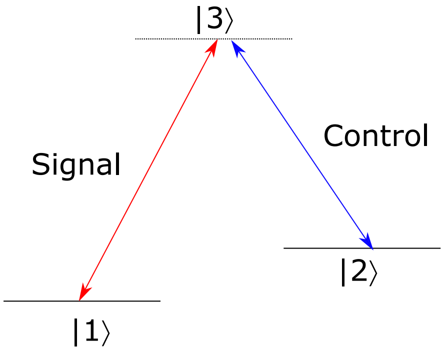

Figure 5.2: A Λ EIT level scheme with the signal and control fields resonant with the excited state $|3\rangle$ and two different ground states.

The result is that these two transitions undergo quantum interference and the atom is now effectively in a superposition of the two ground states. The resulting optical response of this EIT system is also illustrated in Figure 5.1. There is now a window of transparency at resonance caused by destructive interference at resonance. The change in refractive index about the resonance becomes sharper too. By combining these two effects, the idea of using EIT for quantum information storage was first proposed in [23]. The key idea is that the dispersion caused by the sharp change of refractive index at resonance coupled with the transparency window would cause the group velocity of any pulse to slow significantly down to speeds much lower than the speed of light. Assuming the storage medium containing all these Λ scheme atoms are initially in the ground state $|1\rangle$. A pulse of light with spectral width smaller than the width of the transparency window enters the medium and gets spatially compressed as the parts that enter the medium first slows down while rest of pulse outside continued to travel at the speed of light. When the pulse is in the medium, the intensity of the control field may be reduced to reduce the transparency window's spectral width. This effectively drops the group velocity further until the pulse is trapped. By increasing the control field intensity again, the pulse may then continue to propagate through the medium and is recalled. A more in-depth overview of this effect may be found in [22].

EIT has been the focus of much research effort as a potential quantum memory protocol since it was proposed. It was first experimentally demonstrated using cold sodium atoms to store coherent light in 2001 [24]. Sodium atoms were confined in a magneto-optical trap (MOT) at a temperature of 1 mK and then polarization gradient cooling was used to further cool the atoms to 50 μK. Evaporative cooling was then used to finally push the temperature down to 0.9 μK. [25]

Since then, the performance of EIT based quantum memories have greatly improved. Recently, a scheme was reported to have a observed a efficiency of 96% which is a record high for any existing quantum memory systems [21]. The efficiency of this system with respect to storage time is shown in Figure 5.3.

To achieve such a high efficiency, much effort was placed into optimizing the trapping process for cesium atoms in order to maximize the density of the cloud as detailed in [26]. The cesium cloud was prepared by trapping cesium atoms in a MOT and then was compressed. Through careful tuning of the trapping beam frequency and intensity and pushing the atoms into the desired state through optical pumping, a very dense cloud of atoms was obtained which strongly contributed to the high efficiency observed.

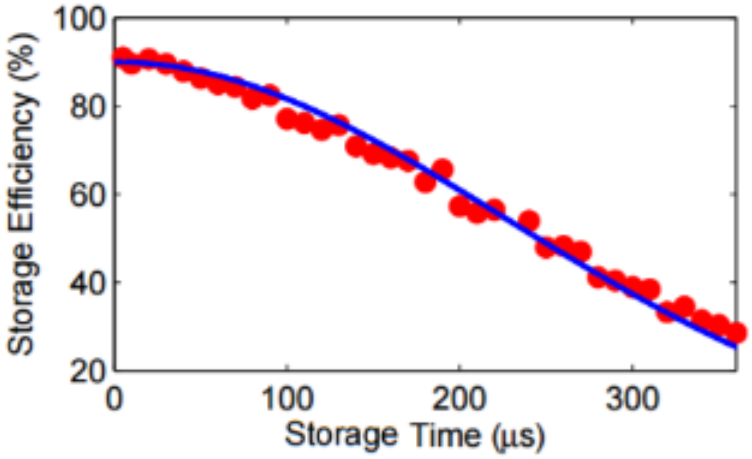

Figure 5.3: Efficiency of EIT storage with respect to storage time. The red dots are the measured efficiency for different storage times and the blue curve a decaying exponential fit of the form $90e^{-t^2/\tau^2}$ where $\tau = 325\ \mu$s. Taken from [21].

At the other end of the spectrum, long storage times up to 240 ms was reported in [27] using an EIT scheme on rubidium atoms. The atoms were prepared in an ultracold Mott insulator state. Though not specified in the paper, it could be inferred that the temperature of these atoms were on the order of nK if not lower as a Mott insulator state could be obtained from a phase transition of a Bose-Einstein condensate to a more structurally organized lattice state [28]. However, unlike in [21], a much lower efficiency of 0.3% was observed.

Although EIT schemes have been demonstrated to have high performance, it is not without limitations. Clearly, the pulses that can be stored inside EIT memories have limitations in their spectral and spatial width. If the frequency components of the pulse did not fit in the transparency window, parts of the pulse would just pass through the medium. The length of the memory needs to be long enough to store the pulse as well.

5.2 Raman memory

The Raman memory uses a similar Λ atomic level scheme as in EIT with the main difference being that both the signal and control fields are operated detuned from resonance as shown in Figure 5.4.

As a result of the off resonance transitions used, the optical response of a Raman scheme differs greatly from EIT. By being off resonance, the atom-light interaction strength is much weaker. Introducing the control field in this case effectively generates a Raman transition pathway between the $|1\rangle$ and $|2\rangle$ ground states through the virtual excited state. This means the storage state is now the $|2\rangle$ stable ground state which leads to longer storage times compared to storing information in excited states. To retrieve the stored light, the control field just needs to be reapplied. A more in-depth description of this process can be found in [29].

To store optical pulses with non-zero spectral width, the control field must also similarly be pulsed to allow the system to absorb the entirety of the input pulse. Retrieving the stored pulse would require another pulse of the control field. [30] This is illustrated in Figure 5.5.

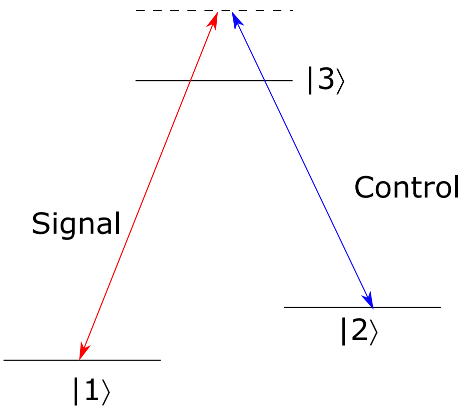

Figure 5.4: The Raman memory atomic energy level scheme where both the signal and coupling beams are detuned from their transitions.

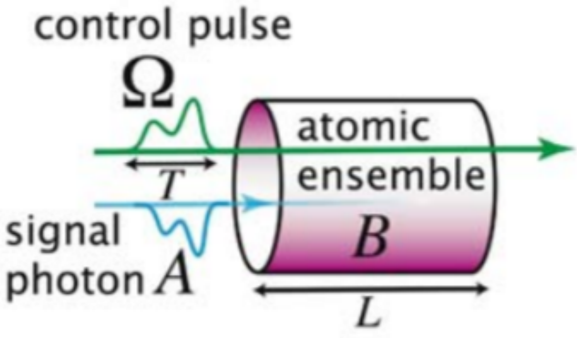

Figure 5.5: Raman memory storage process where both the signal and control fields are needed to be pulsed to store all the information in the signal pulse. Taken from [29].

The most major recent report of a cold atom Raman memory scheme was the storage of entangled photonic states in a Raman scheme in [31]. A simple MOT setup was used to trap cold rubidium atoms for this experiment. The efficiency of this system was 26.8% with a storage time of 1.4 μs. Their efficiency was largely limited by reabsorption.

One of the key advantages to a Raman memory is its large bandwidth (on the order of GHz) [32] which also meant it was compatible with very short pulses of light useful for fast quantum communications. However, it is limited to single mode operation; if a second pulse of light is to be stored, the control field needed to write a second pulse would cause the first to be recalled.

5.3 DLCZ

The DLCZ scheme was named after Duan, Lukin, Cirac and Zoller who proposed its design in 2001 in [33]. It facilitates long distance and long lifetime entanglement between quantum memories for long distance quantum communications. Similarly, it starts with an ensemble of Λ scheme atoms in the ground state. An off-resonance weak write pulse is sent into the ensemble and couples the $|1\rangle$ to $|3\rangle$ transition and results in a forward scattered Stokes photon from the $|3\rangle$ to $|2\rangle$ transition. By making the detuning large enough, it is possible to control the ensemble to be statistically likely to only emit a single photon into the spatial mode of interest at a time. A similarly detuned read pulse in the

$|2\rangle$ to $|3\rangle$ transition may be sent to the ensemble to retrieve an anti-Stokes photon in the backwards direction. This is illustrated in Figure 5.6a.

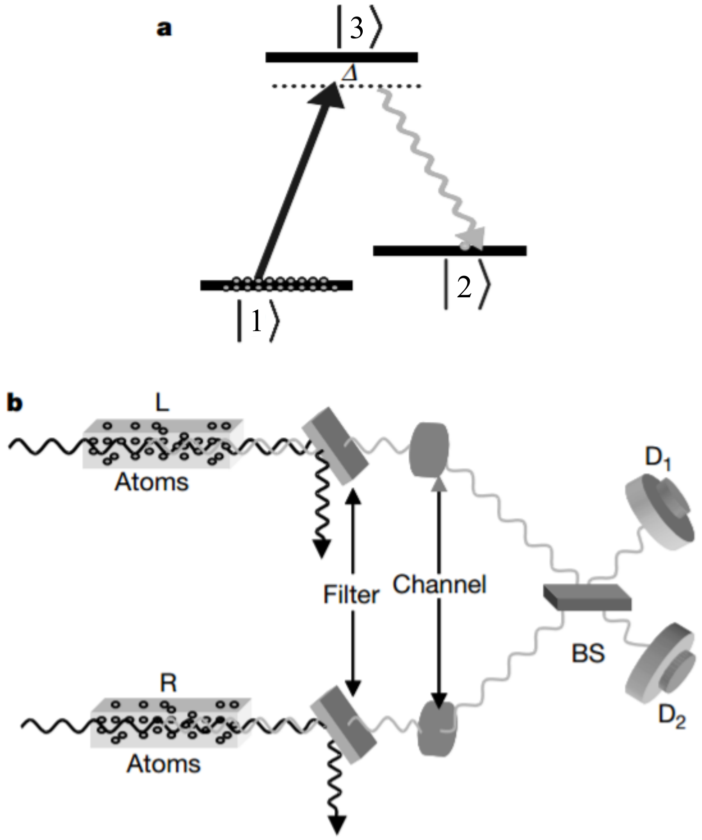

Figure 5.6: a) The Λ atom in the DLCZ scheme when an off-resonance write pulse excites the atom into the $|3\rangle$ state from the $|1\rangle$ ground state and emits a Stokes photon in the forward direction as it decays down to the $|2\rangle$ state. b) The DLCZ entanglement scheme where essentially the Stokes output of two ensembles are interfered at a 50:50 beamsplitter (BS) and outputs detected at two single photon detectors D_1 and D_2. Modified from [33].

To entangle two ensembles, the Stokes output of two ensembles interfere on a 50:50 beamsplitter which has its output monitored by two single photon detectors D_1 and D_2 as shown in Figure 5.6b. Successful entanglement occurs when either of the detectors detect a photon; the detection event only indicates that one of the ensembles has emitted a Stokes photon but not which one. This entanglement state is stored in the $|2\rangle$ ground state allowing for potentially long storage times and may be retrieved by sending in a read pulse as described before. [32]

The storage part of the DLCZ scheme in cold atomic ensembles was first experimentally demonstrated in [34] using simple MOT of cold cesium atoms as the medium. Since then, a high efficiency scheme of 84% efficiency with storage times of about a few hundred ns has been reported in [35] by employing cooled cesium atoms in a MOT inside an optical cavity. Even more recently, [36] reported long storage times of 3.2 ms at 73% efficiency using rubidium MOT inside a ring cavity. This scheme inherently can only operate in single mode as it relies on only having one Stokes photon being released for it to work.

5.4 Gradient Echo memory

The Gradient Echo memory (GEM) system has one of the highest efficiency in existing systems [37]. A good way to picture how GEM works is to think of the system as being made up of an ensemble of two level atoms. By placing these atoms into a linear magnetic field gradient, these atoms will experience inhomogeneous broadening of their energy levels; the Zeeman shift magnitude for the atoms will be location dependent as shown in Figure 5.7.

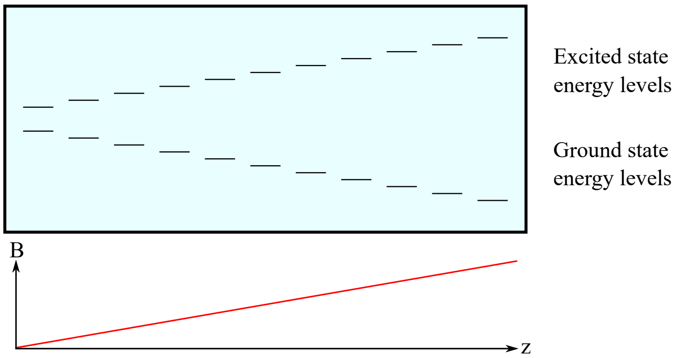

Figure 5.7: Inhomogenous broadening of atomic energy levels along the z direction due spatially dependent Zeeman shifts to the atom from a magnetic field gradient.

The continuous range of atomic transition frequencies produced by this gradient generates a broad range of absorption frequencies compatible with this atomic ensemble so when a pulse of light is sent to be absorbed, its various frequency components get absorbed at different spatial locations along the length of the ensemble. This effectively encodes the pulse into the ensemble through a spatial Fourier transform. A key advantage this configuration brings is that as the pulse is retrieved from the ensemble, the various frequency components leave by passing by atoms that are not resonant so that the efficiency of the system is not reduced by reabsorption.

When light is absorbed by the atoms, the ensemble is sent into a superposition state. Representing the system using a Bloch sphere, assuming all the atoms are in the ground state initially, the Bloch vector would point towards the bottom pole of the sphere. This is shown in Figure 5.8a. As the atoms absorb a pulse, they are sent into a superposition state and the Bloch vector moves upwards along the surface of sphere (Figure 5.8b). Depending on the Zeeman shifting these atoms experienced, their spin state starts to precess on the surface of the sphere. Over time, they start to dephase as shown in Figures 5.8c and 5.8d. This represents the atomic coherence of the atoms; the coherence dephases over time as the speed their state evolves in is dependent on their spatial location. Effectively, the absorbed pulse has been converted into a collective state of the ensemble. To reverse this process, one needs to reverse the magnetic field gradient at time τ. This reverses the state evolution and causes the coherence to rephase. When they are in phase again, the original optical pulse is regenerated.

In practice, three level atoms are used rather than two level. The reason for doing so is as follows. When choosing an excited state in a two level atom, there is a trade off between efficiency and storage time. For example, if one chose an excited state with a long lifetime to enhance the storage time of the system, that state would usually have weak interaction strength and thus poor absorption rate. This means the efficiency of the system has been compromised.

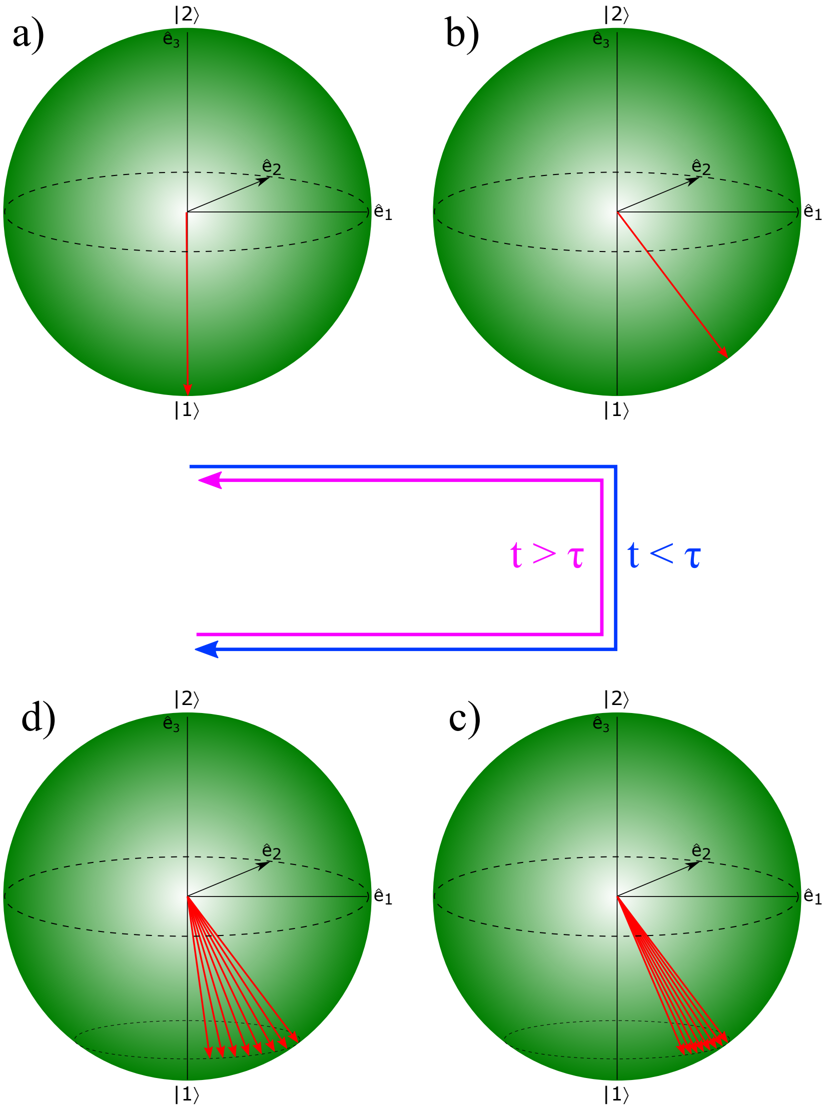

Figure 5.8: The process of storing an optical pulse using GEM as represented by a Bloch sphere. Assuming all the atoms start off in the ground state (a), absorbing an optical pulse sends the ensemble into a superposition state (b). The atomic coherence of the atoms dephase as a result of inhomogeneous broadening (c). At time τ, the magnetic field gradient is flipped and the coherences rephase (d). This reverses the process and eventually regenerates the original optical pulse.

When using three level atoms, rather than storing the energy of the photon, it is the information about the fact that a photon has been absorbed that is stored. This is demonstrated in Figure 5.9.

The three level atom has three states, two of which are ground states. The signal field, which is to be stored, along with a control field are used to create a Raman transition. So electrons in $|1\rangle$ that are excited by the signal field end up in the second ground state $|2\rangle$ thereby effectively storing the information about absorbing a photon without storing the photon's energy. By shifting the storage state into a stable ground state, the issue with storage lifetime is solved. To retrieve the information, the electron in state $|2\rangle$ then absorbs energy from the control field and as it decays back down to state $|1\rangle$, the original photon is regenerated. Note that the Raman transition is tuned off resonance to avoid

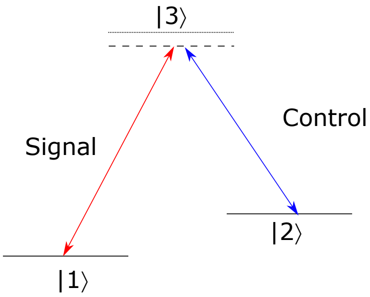

Figure 5.9: Three level atom for GEM.

promoting atoms into state $|3\rangle$ which might lead to spontaneous emissions. Even though three level atoms are used, the theory on the inhomogeneous broadening still applies.

In a recent publication, GEM was reported to have achieved a efficiency of 87% with storage times up to 1 ms [18]. The detailed process for preparing the rubidium atomic ensemble is detailed throughout this thesis. Since the atoms could not be trapped by the MOT during the storage phase, the storage time of this system is ultimately limited by the gas atoms dropping due to gravity. Not only is this memory compatible with storing multiple pulses of light but through manipulation of the system parameters, the pulses could be recalled in arbitrary order, time stretched or compressed and even split into smaller pulses. This is detailed in [38].

5.5 Summary

Although a brief review of some of the more prominent cold atom quantum memory schemes has been presented, there are still numerous other systems that have been explored. For example, the atomic frequency comb, other photon echo techniques, etc. An implicit property of these memories was that generally efficiency of these systems was maximized with shorter storage times. Generally, using cold atoms as a storage medium has proven to improve both efficiency of their systems through increased density of their atomic clouds and also improved storage times through better stability of the system. All of these schemes have their own advantages as a quantum memory.

Chapter 6

Experimental setup

6.1 MOT transitions

In order to create a MOT, it is essential that the beams are initially prepared to have the correct frequency, intensity and polarization. The frequencies needed for this experiment are labeled in Figure 6.1.

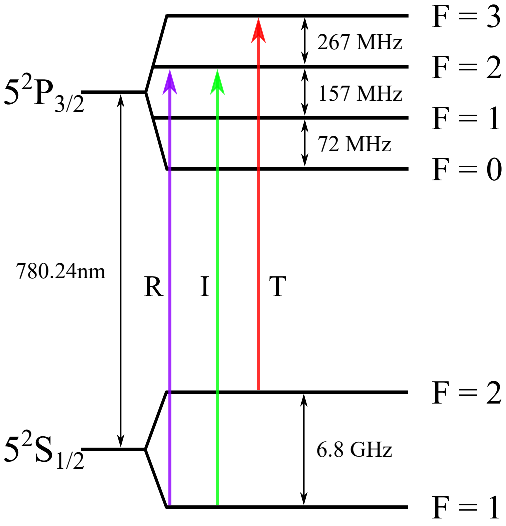

Figure 6.1: The transition frequencies needed in the experiment on the energy level diagram of rubidium-87 D2 (not to scale). T is the trapping, R is the repump and I is the imaging. The imaging beam is used later to image the rubidium gas cloud. The frequencies were obtained from [11].

The trapping of Rb atoms are done using the $F = 2 \rightarrow F' = 3$ closed cycling transition where atoms excited into the $F' = 3$ state can only decay back down to the $F = 2$ ground state by selection rules. However, to achieve cooling, the beams are necessarily red detuned from this transition which would bring it closer to the $F = 2 \rightarrow F' = 2$ transition. As a result of the non-zero overlap between the laser and the $F = 2 \rightarrow F' = 2$ absorption line, atoms may sometimes be excited into the $F' = 2$ state where the atoms may potentially decay back down to either the $F = 2$ or $F = 1$ ground state. If the atom decays back down to the $F = 2$ state then the trapping beams will push it back into the cycling transition. However, if the atom decays down to the $F = 1$ state, which does not interact with the laser, it will stay in that ground state and not contribute to trapping and cooling. Even when the detuning is not large, atoms will eventually accumulate in the $F = 1$ dark state over time through optical pumping. This will result in atoms diffusing out of the trap over time.

To resolve the above issue, generally another beam called the repump is introduced working on the $F = 1 \rightarrow F' = 2$ transition as labeled in Figure 6.1. Any atoms that decay down to the $F = 1$ level will be sent back up to the $F' = 2$ state where they may decay back into the $F = 2$ state and return into the cycling transition. If the repump beam interacts strongly enough with the atoms, the atoms would not be able to accumulate in the $F = 1$ ground state and thus stay trapped.

The entire optical setup required to do this experiment is quite complex so it has been divided into parts that are described in the following few sections.

6.2 Beam preparation

Not only do the beams need to have the correct frequency and intensity, it was quite important that there was fine control over both of these parameters.

6.2.1 Trapping beam preparation

The equipment configuration for preparing the trapping beam is shown in Figure 6.2.

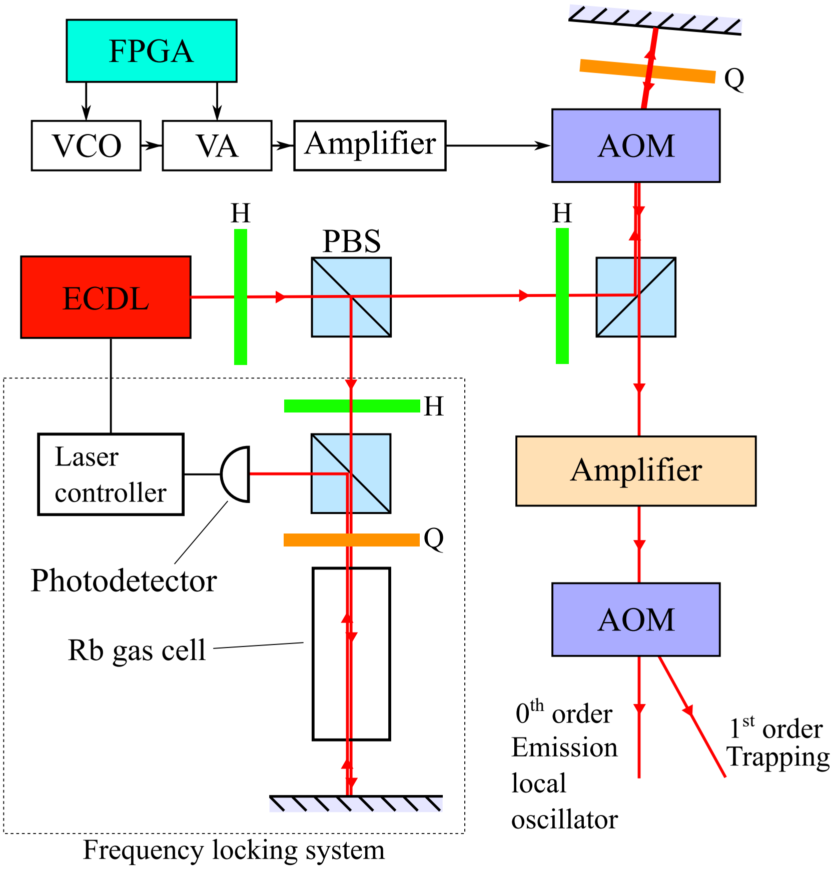

Figure 6.2: Configuration used to prepare the beam from an external cavity diode laser (ECDL) into the trapping and emission local oscillator beams. The abbreviations are: PBS - Polarizing beam-splitter, H - Half wave-plate, Q - Quarter wave-plate, AOM - Acoustic-optic modulator, VCO - voltage controlled oscillator, VA - variable attenuator, FPGA - field-programmable gate array. The driver for the second AOM was just a function generator generating a sinusoidal signal.

The source of the trapping beam was an external cavity diode laser (ECDL) that operated close to the D2 transition at a wavelength of 780 nm and was controlled using a laser controller capable of controlling the laser frequency through the current supplied to the diode and a piezoelectric actuator on the external cavity. Using a polarizing beam-splitter (PBS), part of the laser output was sent to a frequency locking system used to stabilize the laser frequency through feedback. This is properly discussed later. The other part of the beam was sent to another PBS which sent the beam through a 110 MHz acoustic-optic modulator in a double pass configuration as shown. The acoustic-optic modulator was controlled using a Labview digital controller that operates much of the experiment through a field-programmable gate array (FPGA). The FPGA generated analogue signals sent to a voltage controlled oscillator (VCO) in series with a variable attenuator (VA). The VCO generated a sinusoidal signal with frequency determined by its input voltage and the signal was then attenuated by a factor determined by the input voltage to the VA. This electronic signal was then amplified and sent to the AOM.

The AOM diffracted the input light into many diffraction orders using sound waves in a crystal. Different diffraction orders from the AOM were deflected at different angles; the higher the order of diffraction, the larger the frequency shift of that order. It was aligned so that more of the output power was sent to the first order mode which shifted the beam frequency by the frequency of the VCO output. The AOM was optimized to work close to 110 MHz so if a 110MHz was sent to it, the AOM could be aligned to dump most of its power to the first order mode which shifted the beam frequency up by 110 MHz. Since a double pass configuration was used, the frequency shift was observed twice; the beam was shifted up by 220 MHz in this setup. The amplitude of the electronic signal determined how much optical power was sent to the first order diffracted output of the AOM. The remaining power stayed within the fundamental output mode where no frequency shift occurred. The advantage of this double pass setup was that when the frequency shift was changed, even though the deflection angle of the first order output changed too, the optical alignment after the AOM remained the same after passing through twice. It is commonly used on AOMs to minimize deflections in the optical setup. This meant that the frequency of the beam could be changed freely without jeopardizing the alignment afterwards which might have resulted a drop in optical power that reached the trap.

The frequency shifted beam was then sent to an optical amplifier system. It worked by seeding another ECDL using this beam such that this second ECDL followed the frequency of this shifted beam. The output of this new ECDL was then sent through a tapered amplifier where the optical amplification could be controlled by its current.

Finally, the laser was sent through a final AOM used to shift the frequency beam back down 80 MHz. Though not shown in the diagram, this beam was coupled into a fibre that brought the trapping beam to another optics table where the rubidium gas chamber was.

6.2.2 Repump beam preparation

The preparation of the repump beam was quite similar to that of the trapping beam. The same frequency stabilization system was used and the beam from the ECDL was directly amplified using a tapered amplifier. The beam was then split for repump and imaging purposes. Only single pass AOM systems were used for this beam due to the frequency operation range of the AOMs and the frequency stabilization point. Even though this did affect the optical alignment after the AOM whenever the repump and imaging frequencies were changed, it was realized that the telescope system after the two beams used to couple the beams into optical fibres was robust enough to account for slight misalignments like this so the power coupled into the fibres stayed fairly constant. The setup is illustrated in Figure 6.3.

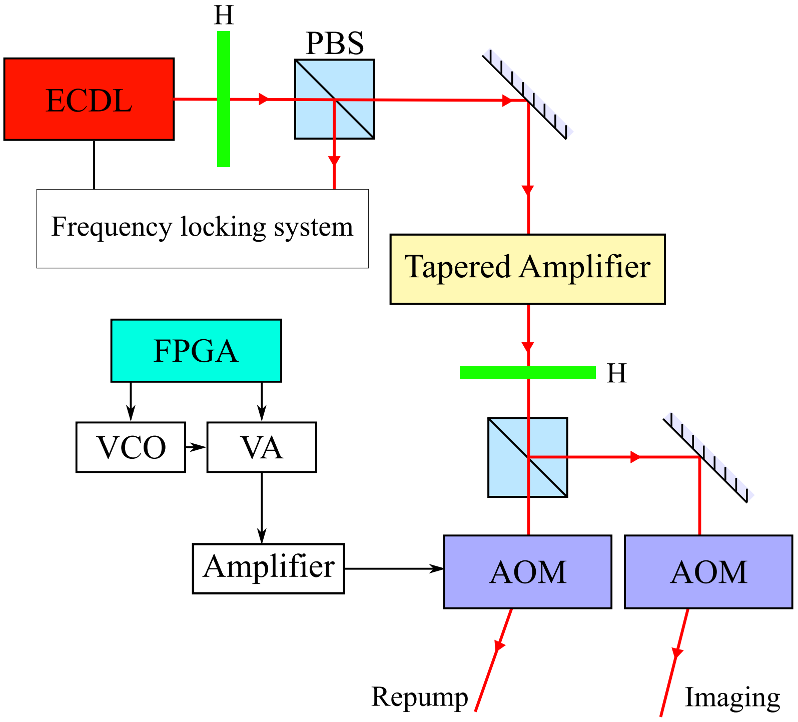

Figure 6.3: Setup used to prepare the beam from an ECDL into the repump and imaging beams.

6.2.3 Frequency locking system

For a stable MOT, the frequency of the cooling beams must be stable as well. This was basically achieved using a Pound-Drever-Hall (PDH) frequency stabilization system [39] to stabilize the laser frequency to a chosen Rb-87 hyperfine transition.

First, the hyperfine transitions must be observed and this was done using saturated absorption spectroscopy with the setup as labeled in Figure 6.2. A fairly powerful beam was sent through the PBS through the Rb gas cell and if the laser frequency was roughly in the range of the Rb-87 D2 transition, many atoms would be excited to the $5^2P_{3/2}$ hyperfine states. The beam reflected back through the gas cell would then measure reduced absorption due to the reduced amount of atoms in the ground state. However, this only works when the atoms are resonant to both the pump and probe beams; if the atom was moving in the propagation directions of the pump and probe beams, the beams would be Doppler shifted in opposite directions and thus there is no reduced absorption as it is not resonant with both beams simultaneously. Therefore, only atoms that have zero velocity with respect to the direction of beam propagation or are resonant with two different transitions simultaneously would experience reduced absorption which would appear on the absorption spectrum as a small dip. This results in a Doppler free spectrum which allows one to resolve some of the hyperfine absorption lines, which are on the order of MHz, despite the transition being Doppler broadened by about 600 MHz at room temperature [12]. The saturated absorption spectrum of the D2 line is shown in Figure 6.4.

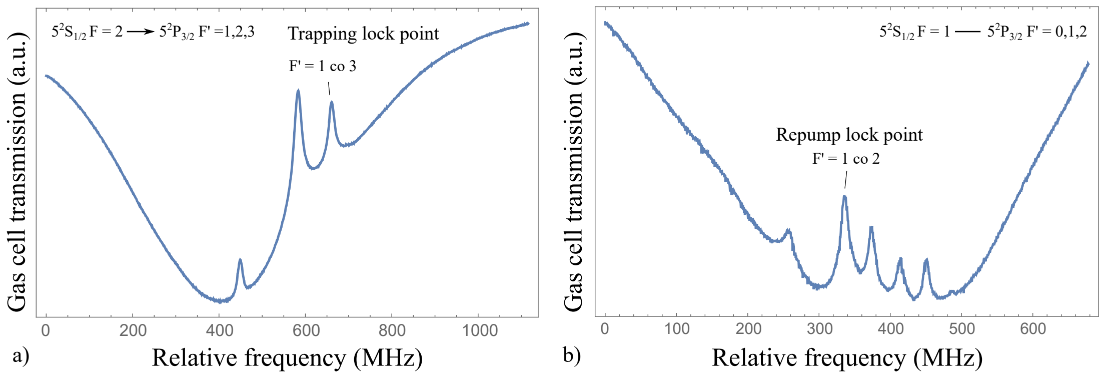

Figure 6.4: Measured Rb-87 D2 line using saturated absorption spectroscopy.

The absorption dips that have been labeled in Figure 6.4 were the transitions that the laser frequency was stabilized on. Both of these are cross over peaks between different hyperfine levels that occur when the atoms are resonant with two transitions. These locking points were chosen because their absorption dips had a fairly large signal and while still being convenient based on the operation frequency range of the AOMs.

The error signals were generated by first modulating the system and then demodulating the transmission signal from the photodetector using the initial modulation signal. This was low pass filtered to generate a PDH error signal. This signal was then used by the laser controller to control both the diode current and piezoelectric actuators to stabilize the laser frequency. All of these electronic processes was completed inside the laser controller box.

6.3 Magneto-optical trap

After expanding them, the beams were ready to be used to construct a MOT. Both the trapping and repump beams take the same optical path to form 3 pairs of circular polarized counter propagating pairs of beams that intersect at a Rubidium gas cell as illustrated in Figure 6.5.

Both the trapping and repump beams from the previous section were split into three beams of equal power and configured to irradiate the rubidium gas cell from three orthogonal directions as shown. Their respective orthogonally polarized pair were simply produced by reflecting them back through the gas cell with mirrors. It was not essential for the repump beam to follow this beam path as well but since the repump could be red detuned to the repump transition, it could also offer a small amount of extra cooling in this setup.

For quantum memory purposes, it was ideal for the efficiency to gather the maximum number of atoms in the propagation path of the storage beam. As a result, rather than the spherical MOT that could be produced using the pair of circular coils in Figure 4.9, two sets of elongated MOT coils were used to trap the Rb-87 atoms in a cigar shape. These coils allow for strong trapping forces in the x and y directions. A third set of coils called the cap coils allowed for control over the length of the MOT in the z direction.

The Labview controlled FPGA is responsible for running much of the experiment as it can take parameter values set by a user on a computer and push them to relevant parts of the experiment. As mentioned previously, it has control over the AOMs that control the intensity and frequency of the trapping and repump beams. Through a run builder

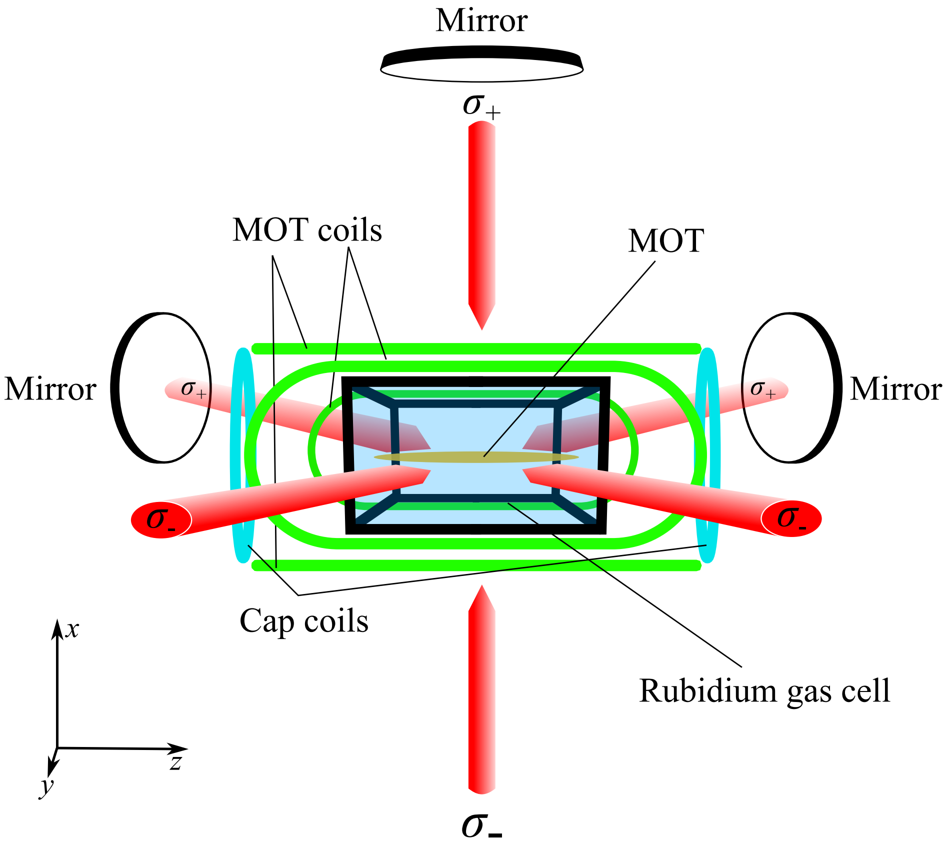

Figure 6.5: Diagram of experimental setup for the MOT. The 6 beams shown are 3 pairs of orthogonal circular polarized counter propagating beams. These beams contain both the trapping and repump beams and were created by retro-reflecting 3 circular polarized beams back through the gas cell. Unlike in Figure 4.9, three pairs of anti Helmholtz coils were used to shape the trapped gas cloud into a cigar shape. The MOT coils were used to confine the Rb atoms in the x and y directions to form a 2D MOT. The Cap coils were used to restrict the length of the MOT in the axial z direction.

programmed using python, parameter values can be pushed to the equipment in real time repeatedly allowing for time varying features like ramping up MOT coil currents to increase the magnetic field gradient to compress the gas cloud. This run builder was programmed to run in various modes. Continuous mode allows for a pre-built array of parameters to be looped at time intervals determined by the length of the sequence. Manual mode allows parameters to be changed in steady state. Finally, the mode used the most in this experiment would be the parameter sweep where it works similar to the continuous mode but it allows for different values in the parameter array to be swept between determined values at set number of steps. This mode allows for efficient observation of how the MOT changes with respect to a change in different parameters. Generally, for a simple MOT, steady state parameters in manual mode is sufficient for simple cooling and trapping of the atoms.

The rubidium gas cell contained a natural abundance of both the Rb-87 and Rb-85 isotopes and were released into the gas cell using a rubidium dispenser that was controlled with the current sent to it. By increasing the current, the density of the rubidium gas inside the gas cell could be increased. To reduce background collisions, the gas cell was connected to a ion pump that reduced the pressure in the cell down to the order of 10^{-9}

Torr.

The entire setup was mounted on a pressure stabilized floating optics table to minimize noise coupled into the experiment through the environment. Three large pairs of Helmholtz coils enclose the experiment to cancel out all external magnetic fields from sources like the earth's own magnetic field, static electric fields, etc. A photo of the gas chamber is shown in Figure 6.6

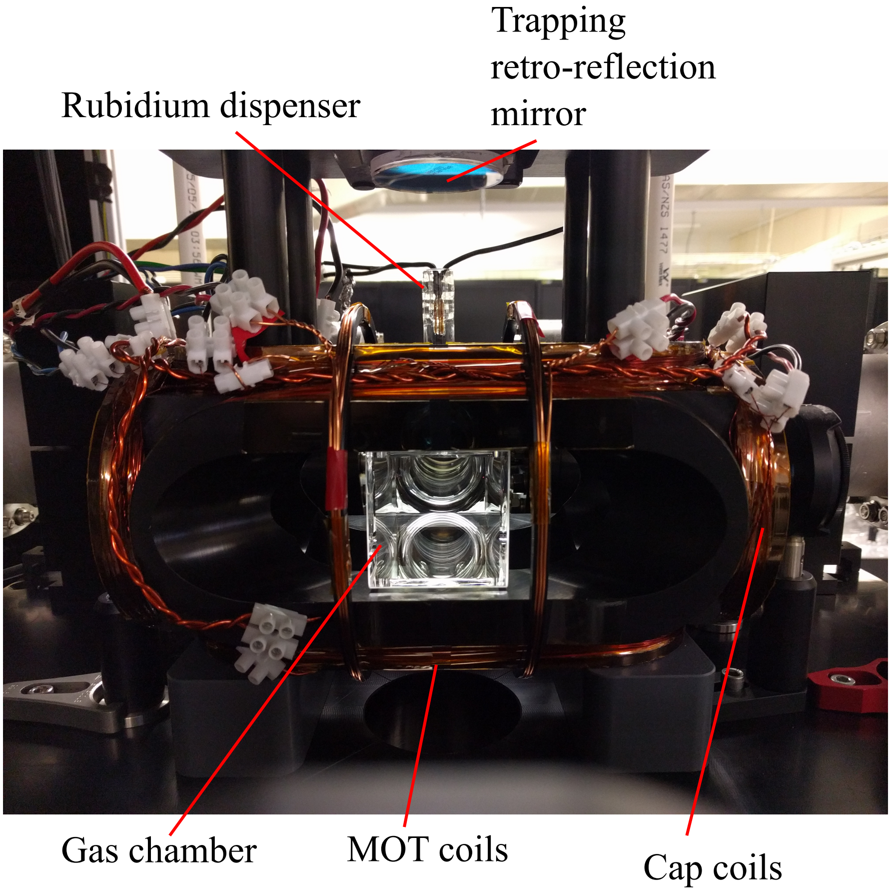

Figure 6.6: Photo of the Rb gas chamber.

6.4 MOT characterization methods

To measure the performance of the MOT, various methods were used to characterize some of its features.

6.4.1 Imaging the MOT

The most direct measurement of the trapped gas cloud is to image it. One might choose to go either with fluorescence or absorption imaging depending on the conditions. Fluorescence imaging is only usable when the trapping beams are on; the atoms need to have a source of light to scatter from for it to fluoresce. On the other hand, absorption imaging can be done at all times given that an imaging beam was prepared and used to irradiate the entire MOT.

Therefore, fluorescence imaging is the most useful at the loading/trapping stage where all the beams and magnetic fields are on to allow for accumulation of atoms in the intersection region. Absorption imaging is not as ideal for the loading stage since the fluorescence will serve to reduce the absorption signal. So when the trapping beams are off and the atom cloud is allowed to freely drop (due to gravity) and expand, called the free expansion stage, absorption imaging becomes the better method. The setup used to do absorption imaging is shown in Figure 6.7.

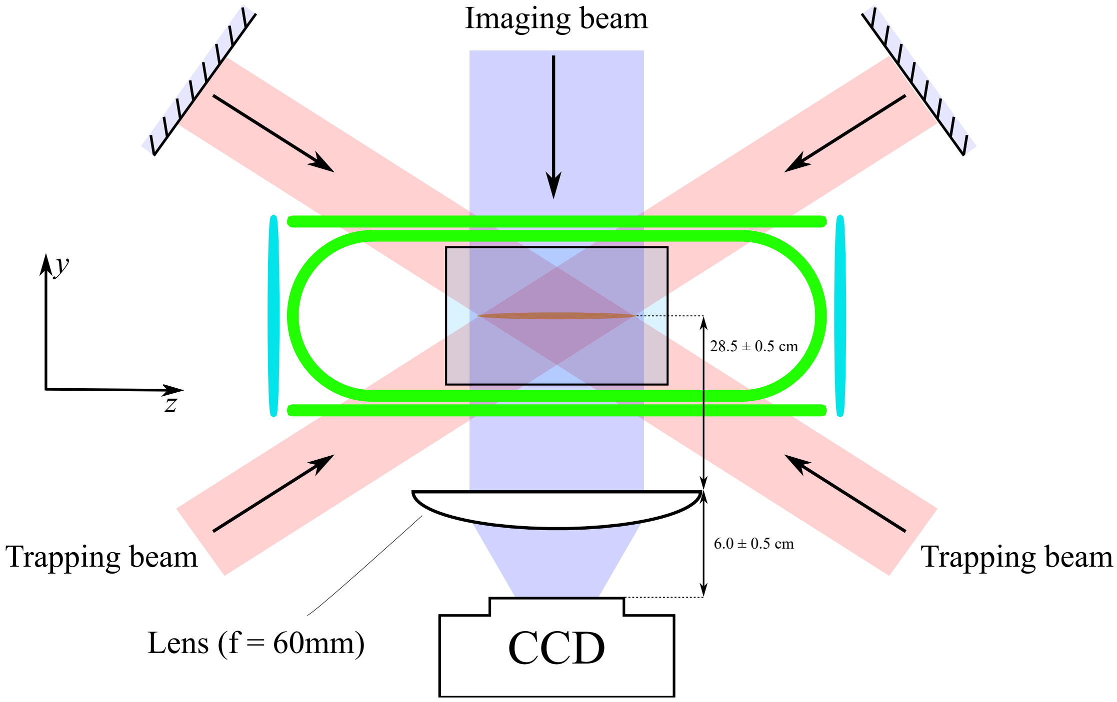

Figure 6.7: A view from the top of Figure 6.5 including the imaging system. The imaging beam was obtained by splitting part of the repump beam as shown in Figure 6.3 and was used to irradiate the MOT from the side for absorption imaging. Its light was collected using a $f = 60$mm lens onto a CCD camera.

To image the MOT, the trapping beams were turned off to allow for free expansion. The image was collected through a large $f = 60$ mm lens onto a CCD camera (Point Grey Grasshopper 1.4) connected to a computer. The imaging beam was derived from the repump beam and then expanded and collimated to evenly irradiate the whole MOT. Its frequency and intensity was controlled using an AOM. The function generator controlling the AOM was configured to operate by sending pulses of sinusoidal signals such that the imaging beam also only operated in pulses. This was important because if the imaging beam, which was resonant with the repump transition, was too intense and irradiated the atoms for too long, it would start pumping atoms out of the $F = 1$ ground state. Since the trapping beams were off during the free expansion stage, atoms would not get pumped back to the $F = 1$ ground state. As a result, the imaging beam was sent in 0.025 ms pulses to minimize optical pumping out of the imaging transition which would have decreased the absorption signal.

Since the imaging beam was not on all the time, it was then necessary to make sure both the camera and imaging bursts were triggered together. The triggering signal was obtained from the FPGA where a trigger pulse was programmed into the run.

The dimensions of the imaging system are shown in Figure 6.7. The magnification of this system was estimated to be $M \approx -0.267$ and the size of a pixel on the CCD is

$6.45 \times 6.45\ \mu\text{m}^2$. Using the images with these parameters, the size of the MOT could be estimated.

6.4.2 Temperature measurements

If the gas cloud was allowed to freely expand, it is quite intuitive that this expansion rate is determined by the temperature of the gas cloud; if it were warmer, the atoms having larger kinetic energy would diffuse out of the trapping region faster. Therefore, by taking absorption images of the gas cloud at different intervals after the trapping beams go off, one can measure the expansion speed of the cloud and thus estimate the temperature. An example of how this might look like in the run builder is shown in Figure 6.8.

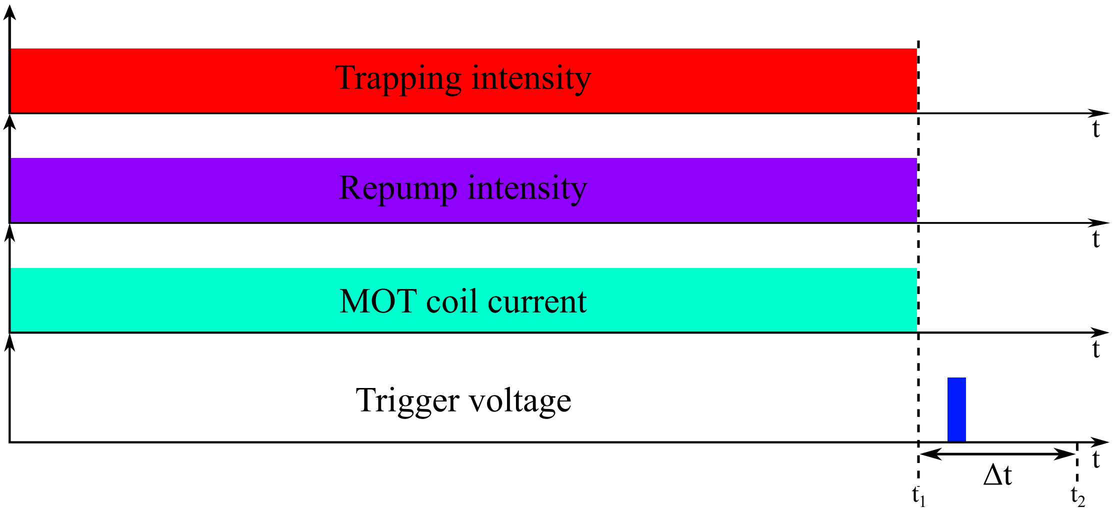

Figure 6.8: Example of how the change in parameters for a free expansion would look like in the run builder. All the beams and magnetic fields are turned off at t_1. Δt is the time during which the cloud is free expanding and the trigger pulse is free to move anywhere in that time period to allow for imaging at different expansion duration. At t_2, the run is looped and restarted again.

The Maxwell-Boltzmann velocity distribution of a gas with temperature T is

$$f(v) = 4\pi v^2 \left(\frac{M}{2\pi k_B T}\right)^{3/2} e^{-\frac{Mv^2}{2k_BT}} \quad , \tag{6.1}$$

where M is the mass of the Rb-87 atoms [40]. The atoms are assumed to have this velocity distribution before the expansion stage. Then using the initial position distribution of the gas cloud and then doing a convolution between this velocity distribution and the measured initial position distribution, a model for of the atomic position distribution as a function of expansion time may be obtained. This model may then be used to fit the expanded position distribution of atoms from the absorption images to obtain an estimate for the temperature T.

6.4.3 Atomic density measurements

Generally, the number of atoms trapped in a MOT could be measured using optical depth measurements as detailed in [41]. This involved taking absorption measurements to determine the number of atoms in the beam path. By Beer's law [12], the change in intensity,

I, of a beam as it travels through a medium is given by

$$\frac{dI}{dz} = -N\sigma_{abs}I \quad , \tag{6.2}$$

where σ_{abs} is the absorption cross section and N is the atomic density. The optical depth, OD, is defined as

$$OD = ln\left(\frac{I_t}{I_0}\right) \quad , \tag{6.3}$$

where I_t and I_0 are the transmitted and initial beam intensities respectively. The above equations show that measurements of the optical depth can be easily used to determine the atomic density where $OD = \sigma_{abs}N = \frac{3\lambda^2}{2\pi}N$. However, the above derivations are only true if the imaging beam is on resonance. If it is off resonance, the reduced strength in absorption needs to be accounted for using the absorption spectrum profile which gives

$$N = \frac{OD}{\sigma_{abs}}\frac{\delta^2 + \Gamma^2/4}{\Gamma^2/4} \quad . \tag{6.4}$$

Using this, the number of atoms could be measured.

6.5 Summary

This section detailed the various optical fields and equipment required to generate a MOT and how they were prepared. It also described how absorption imaging was done on the atomic cloud and the various analysis methods that could be used to extract temperature and density measurements from these absorption images. The next section presents and discusses the results of these measurements.

Chapter 7

Optimization of MOT temperature and density

This section presents the results from doing parameter sweeps on the MOT largely focusing on the following parameters: trapping field frequency and repump field intensity. The imaging system was first optimized for expansion imaging. A time dependent model for the spatial distribution of atoms was obtained through convolution and then used to calibrate the imaging system. The parameter sweep results are then presented and discussed.

7.1 Optimizing absorption image signal

There were three parts to the imaging system, the imaging beam, lens and camera. The optimization required for each part was as follows. As shown in Figure 6.7, the measured dimensions of the imaging system were fairly inaccurate mostly due to the difficulty in aligning the measurement to the location of the gas cloud. Note that the dimensions of the imaging system was optimized through making minor adjustments to the position of the lens until the image of the MOT came into focus. Therefore, the magnification value estimated previously could not be used for accurate measurements.

As noted previously, the imaging beam could not be continuously irradiating as that would pump atoms out of the imaging transition and reduce the absorption signal. Since the imaging beam operated in bursts, it was important to optimize the rate at which the beam pulsed at so it was not too intense while not being too weak for a good absorption signal. Also, it was found useful to actually turn off the repump beam 3 ms before the trapping and coils turned off to allow for the trapping beam to pump more atoms into the imaging/repump transition for a clearer absorption image.

The CCD camera shutter time (time period over which the image was averaged over) was set to the order of 100 μs to make sure a minimal amount of the expansion was blurred out while ensuring enough light was detected. The post processing gain at the computer was set to 1 to avoid introducing too much noise or distorting any information from the image. The imaging beam was set to put out 2000 bursts per second operating at a frequency red detuning of less than 10 MHz from the imaging transition (Figure 6.1). Since the MOT could be quite dense, it was necessary to push the imaging beam off resonance so some variation in the atomic density could be seen in order to determine the spatial profile of the atomic density. It was found that generally a 3.5 MHz detuning produced images with fairly good atomic density resolution without sacrificing much signal strength. Absorption images of the MOT immediately after the trapping beams go off, using imaging beams of different detunings, are shown in Figure 7.1.

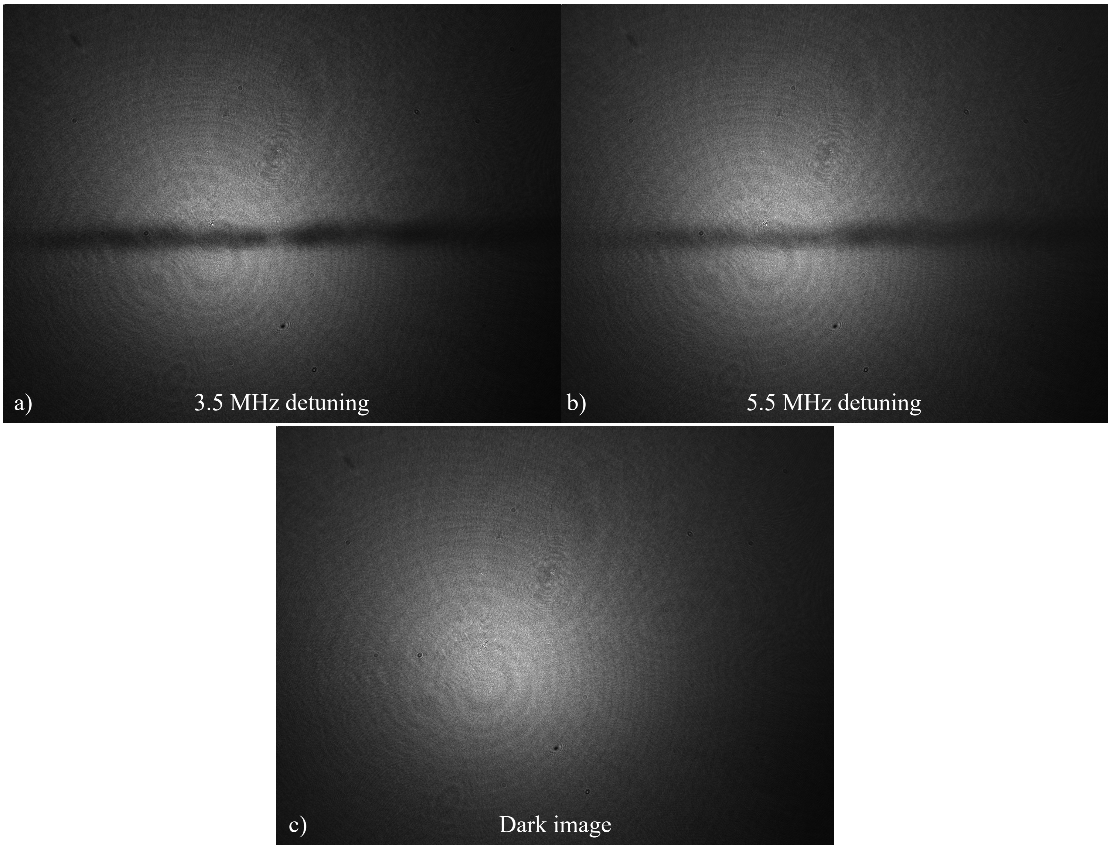

Figure 7.1: a) Absorption images of the MOT with the imaging beam red detuned at 3.5MHz and b) 5.5MHz from the imaging transition. c) A dark image showing the spatial profile of the imaging beam when no atoms were trapped.

Comparing Figures 7.1a and b, clearly the absorption signal was stronger with the 3.5 MHz detuning while retaining some level of resolution on the atomic density of the MOT. Moving to 5.5 MHz detuning improved the atomic density resolution as more light penetrated through the gas cloud while sacrificing some absorption signal strength. Clearly, imaging at different detuning offered different advantages depending on the parameter of interest.

From Figure 7.1c, it could be seen that aside from the imaging beam not being perfectly collimated which resulted in more intense illumination at the center, there were a fair number of aberrations in the intensity profile as well. It was likely that they were introduced from dust or particulates on the optics scattering the beam. Efforts were made to minimize them already through cleaning the optics but they could not be completely eliminated. This was also true for the trapping beams as inspecting the gas cloud profile in Figure 7.1a, clearly, the cloud was not completely uniform. This was especially clear with the gap near the center. It was proven to be likely due to the trapping optics and not the magnetic fields as changing the current in the coils did not change the position of this gap. Also, it was found to be very difficult to actually see the two ends of the gas cloud with this imaging system because both ends reached very close to the walls of the gas cell which were difficult to image.

7.2 Modeling the expansion

With these images, determining the spatial profile of the MOT became a simple operation of subtracting the absorption image of the MOT (Figure 7.1a) from the dark image (Figure 7.1c) which resulted in Figure 7.2a.

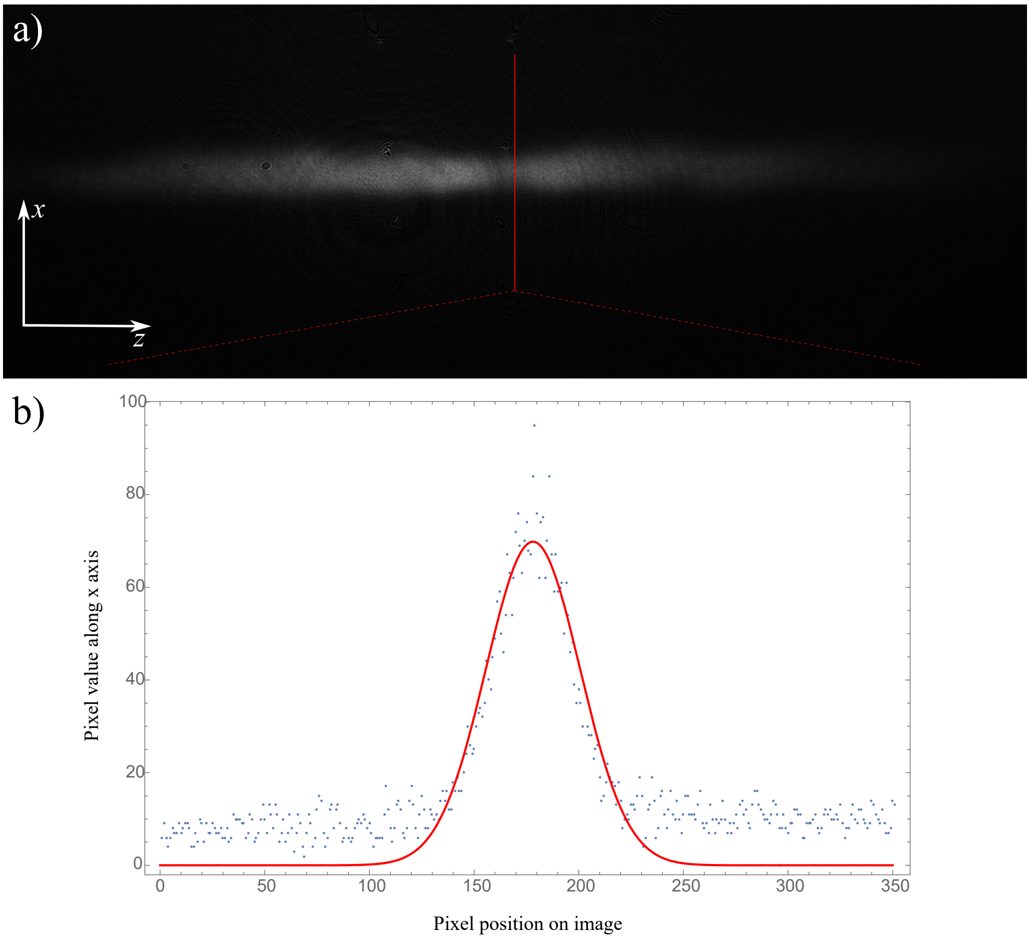

Figure 7.2: a) Image of the trapped atomic cloud obtained from subtracting the absorption image (Figure 7.1a) from the dark image (Figure 7.1c). b)A plot of the cross section pixel intensity as indicated in a) along with a fitted Gaussian model (red line).

The subtracted image showed that since very little light made it through the MOT in Figure 7.1a, the subtraction operation had left the aberrations in the imaging beam in Figure 7.2a. This was a problem for any further image processing so this was addressed by shifting the imaging beam such that the MOT was irradiated by portions of it that had fewer aberrations.

From the cross section intensity shown in Figure 7.2b, it could be seen that despite removing the majority of the background intensity using the subtraction operation, still a fairly minor level of background noise remained. This was likely to have been due to a difference in the absorption image background and the dark image due to fluctuations in the imaging beam or the room fluorescent light over time.

A model was then fitted to this cross section profile. It was found that a Gaussian model offered an excellent fit and this was generally true for most trapping parameters when a gas cloud was successfully trapped. The model in Figure 7.2b did not include an offset as it sometimes led to poor fitting accuracy. Generally, adding in the offset did not change the measured temperature later anyway as both the initial and expanded images were changed by similar amounts. A time dependent model was found by convolving the Maxwell-Boltzmann distribution with a Gaussian position distribution. Since the expansion in neither the y nor the z directions were observable with the absorption images, they were ignored in the model. The velocity distribution of the x velocity component was assumed to have the Maxwell-Boltzmann distribution. The convolution then resulted in a convenient Gaussian model

$$N(x,t) = \frac{1}{\sqrt{2\pi(\sigma_0^2 + \sigma_v^2 t^2)}} \exp\left[-\frac{\left(x - \frac{gt^2}{2}\right)^2}{2(\sigma_0^2 + \sigma_v^2 t^2)} \right] \quad , \tag{7.1}$$

where $N(x,t)$ is the spatial atomic density distribution of the gas cloud as a function of position and time.

Note the $gt^2/2$ factor was added at the end to account for the downwards acceleration of the cloud due to gravity. σ_0 is the initial width of the Gaussian describing the spatial distribution of the atoms just before free expansion. Over time, t, the atomic velocity contributed to expanding the cloud through the factor

$$\sigma_v^2 = \frac{k_B T}{M} \quad , \tag{7.2}$$

where T was the average temperature of the cloud and M was the mass of the rubidium atoms. This model showed that as the cloud expanded, its spatial distribution should remain Gaussian with a width of $\sigma_e = \sqrt{\sigma_0^2 + \sigma_v^2 t^2}$. Therefore, measuring the width of the cloud in the x direction before and time t after expansion allowed for the determination of σ_v and thus the temperature of the cloud, T.

Note that the background level in Figure 7.2b was generally not a problem with images like Figure 7.2a since the signal was fairly appreciable over the noise floor as the trapping parameters were ideal for the cloud density. However, this was not true when lower density clouds were being imaged or when the dark image was taken a substantial amount of time before or after the measurement. An example where the dark image and absorption image was taken at significantly different times is shown in Figure 7.3.

The resolution to this issue is illustrated in Figure 7.4.

First, the intensity profile of the dark image was modeled using a Gaussian in Figure 7.4a. Using the center of the dark image model, x_1, the background intensity of the absorption image was modeled as well using a Gaussian with a center confined to x_1 in Figure 7.4b using only the first 200 pixels. Finally, the absorption image cross section data was subtracted from the background model to get the plot in Figure 7.4c after which the final MOT profile model was obtained from.

Note that the plot of the processed data in Figure 7.4c was noticeably noisier than the simple subtraction shown in Figure 7.3 as the variations in the background intensity of the MOT absorption image could not be removed using a fitted model. The alternative and possibly more ideal way to remove the background completely was by modeling the first 200 points in Figure 7.3 and then subtract it out. However, there were several issues with this approach. Firstly, the model in this case was not necessarily a Gaussian since the fluctuations in the imaging intensity was not known. An arbitrary model could be fitted and would have given a similar result anyway if its width was restricted to be significantly

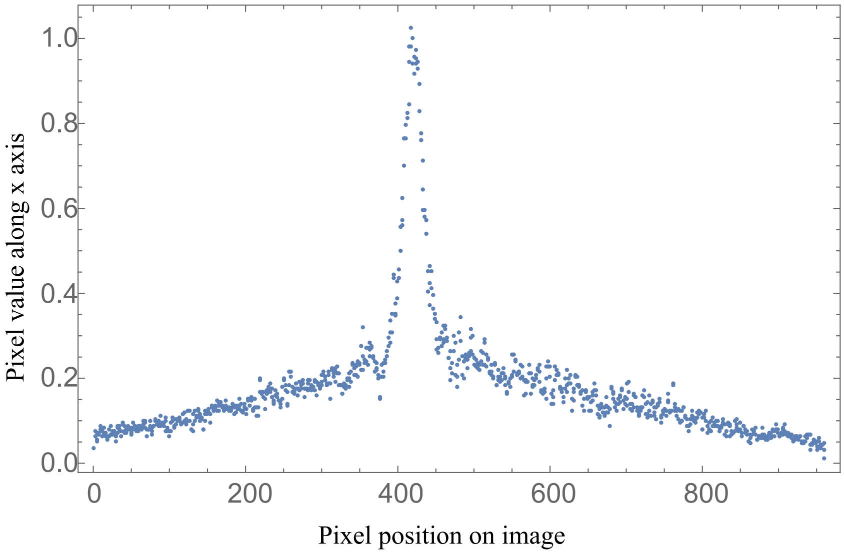

Figure 7.3: Example dark image subtracted cross section profile of an absorption image where the subtraction operation failed to remove some of the background intensity.

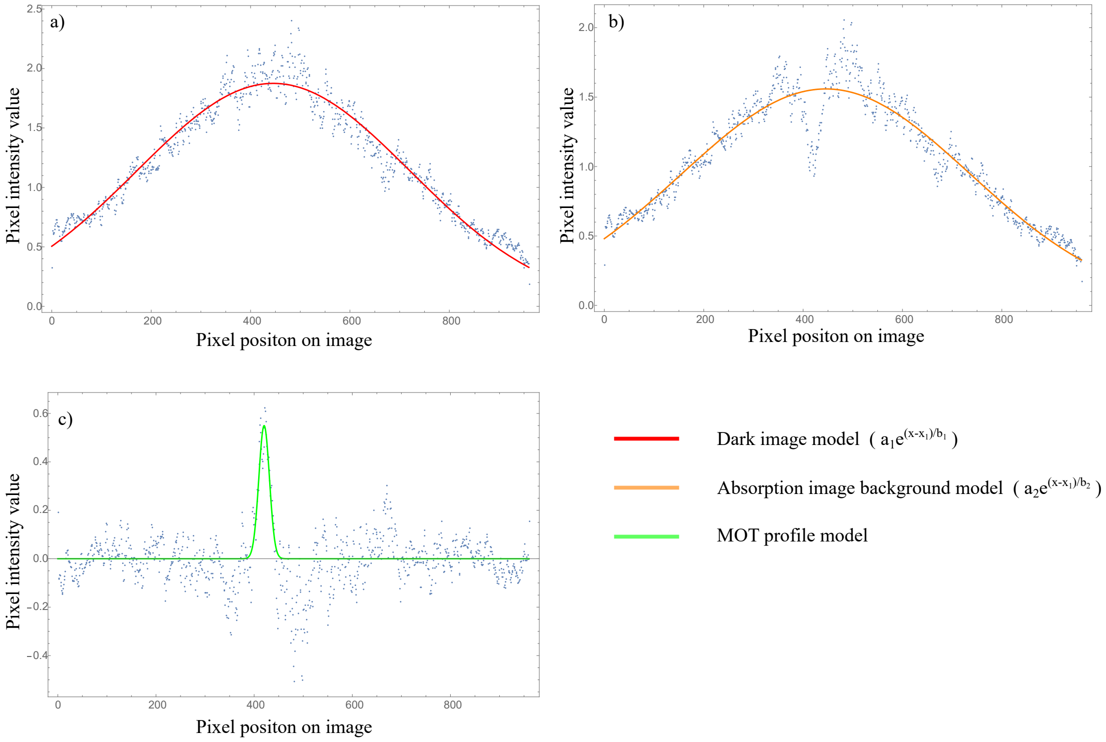

Figure 7.4: a) Cross section intensity profile of the dark image with a Gaussian model fitted (red). b) Cross section intensity profile of the absorption image with a Gaussian model fitted to just the background using the first 200 pixels and forced to center at the same point as with the dark image model (orange). c) The result of subtracting the absorption image profile from its background model and fitted with the final MOT profile (green).

wider than the width of the cloud. Finally, both the computation speed and accuracy of the model fitting were greatly improved when fitting the absorption image background model in Figure 7.4b using the parameters of the dark image model as the starting point.

Such values were not available if the background in Figure 7.3 was directly fitted which led to poor fitting accuracy and long computation times when thousands of images had to be analyzed at once.

7.3 Calibration of imaging system

In the previous chapter, the magnification of the imaging system was estimated using its dimensions but it was observed that very minor adjustments (within the measurement error of the dimensions) to the position of the lens and camera changed the magnification factor greatly. As a result, the $gt^2/2$ factor in the expansion model in equation 7.1 was used for calibration by measuring how much the center of the cloud dropped as a function of time.

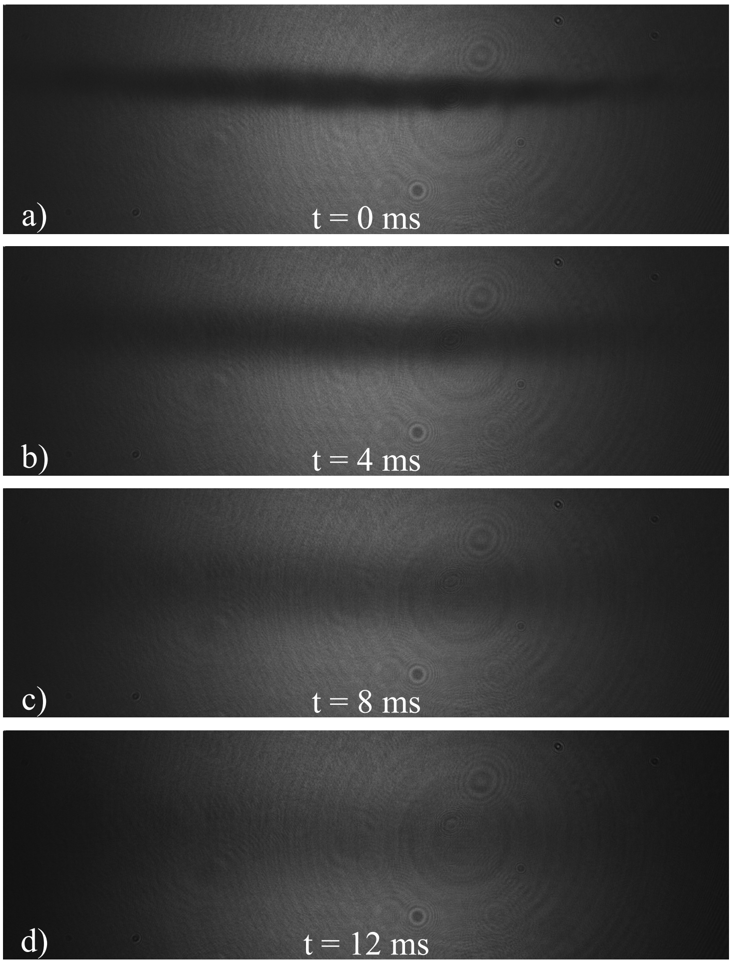

Figure 7.5: Absorption imaging of atomic cloud at different time intervals, t, after the beams were shut off and the cloud allowed to freely expand.

Figure 7.5 showed that even as the cloud was expanding, it was also dropping downwards as expected. The cross section intensity profiles were then modeled as before. Note that in general, these cross sections were produced by integrating over 10 columns of pixels. This was observed to have sufficiently suppressed much of the noise. The center of these Gaussians were extracted from the fitted models and used to calibrate the magnification. The center of the cloud on the images were measured and plotted against time in

Figure 7.6.

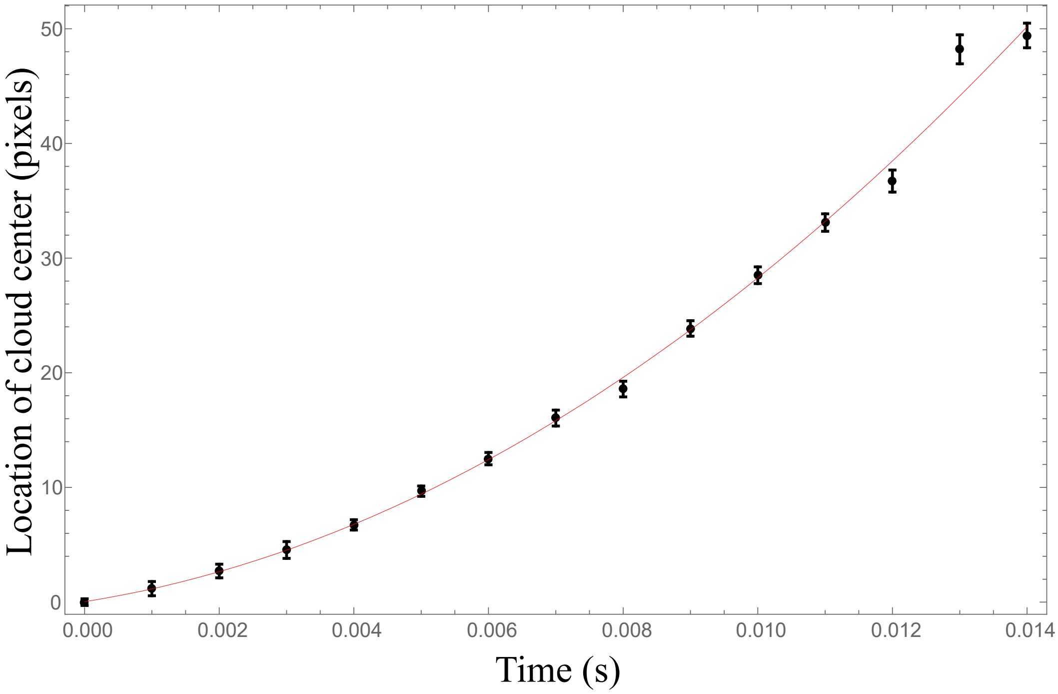

Figure 7.6: Plot of location of center of atomic cloud in the x axis with respect to time. The images were analyzed and Gaussian models were fitted to a cross section of the images in the x direction. The cross sections were obtained by integrating the image over 10 columns of pixels to minimize noise. The Gaussian centers of each image was obtained and for each point in time above, the centers were averaged over 4 images. The errors were propagated from the Gaussian fitting parameter uncertainties. A quadratic model was fitted (red line) to the data.

The fitted quadratic model had the general form of $x = At^2 + Bt + C$ of which the B factor accounted for the initial velocity of the atoms before trapping beams were turned off and C was a constant offset. A accounted for the acceleration due to gravity so the calibration factor, k_{cal}, for the images was found from

$$k_{cal}At^2 = \frac{gt^2}{2} \quad . \tag{7.3}$$

For the particular set of images from Figure 7.5, the conversion from pixels on the images to length at the MOT was $k_{cal} = 2.4 \pm 0.3 \times 10^{-5}$m/pixel. Note that this factor had to be recalculated every time changes were made to the imaging system. Also, note from this that the timing error from the FPGA that timed when to shut off the beam and output the trigger pulse was negligible since it had a refresh rate of 10MHz; the majority of the error in these measurements came from the uncertainty in determining the central location of the gas cloud.

7.4 Temperature measurements

With the information presented so far in this chapter, all the pieces necessary to make temperature measurements were ready: the initial and expanded image, the time at which the expanded image was taken and the calibration factor. One would then just fit Gaussian models to appropriately integrated cross sections of the images and extract the widths of initial, σ_0 and expanded, σ_e, Gaussians and find the temperature through

$$T = \frac{M(k_{cal}\sigma_v)^2}{k_B} = \frac{Mk_{cal}^2}{k_B}\frac{\sigma_e^2 - \sigma_0^2}{t^2} \quad . \tag{7.4}$$

Given the model in equation 7.1, it could be seen that it technically did not matter at what time interval, t, the temperature was measured as all the measurements should yield the same initial temperature but this needed to be confirmed. In order to find a suitable time interval for future measurements, an atomic cloud was trapped and then allowed to freely expand. It was noted that after $t = 14$ ms, the expanded cloud became too diffuse to identify anymore even with ideal trapping parameters. With this, images were taken at increasing intervals of 1 ms after trapping was turned off up to 14 ms. Note that ideally, these images would have been taken from the same expansion run. However, the CCD cameras were unable to acquire at such a rapid rate. Therefore, each image had to be taken in separate runs with the same trapping parameters but just triggering the camera at different times into the expansion phase.

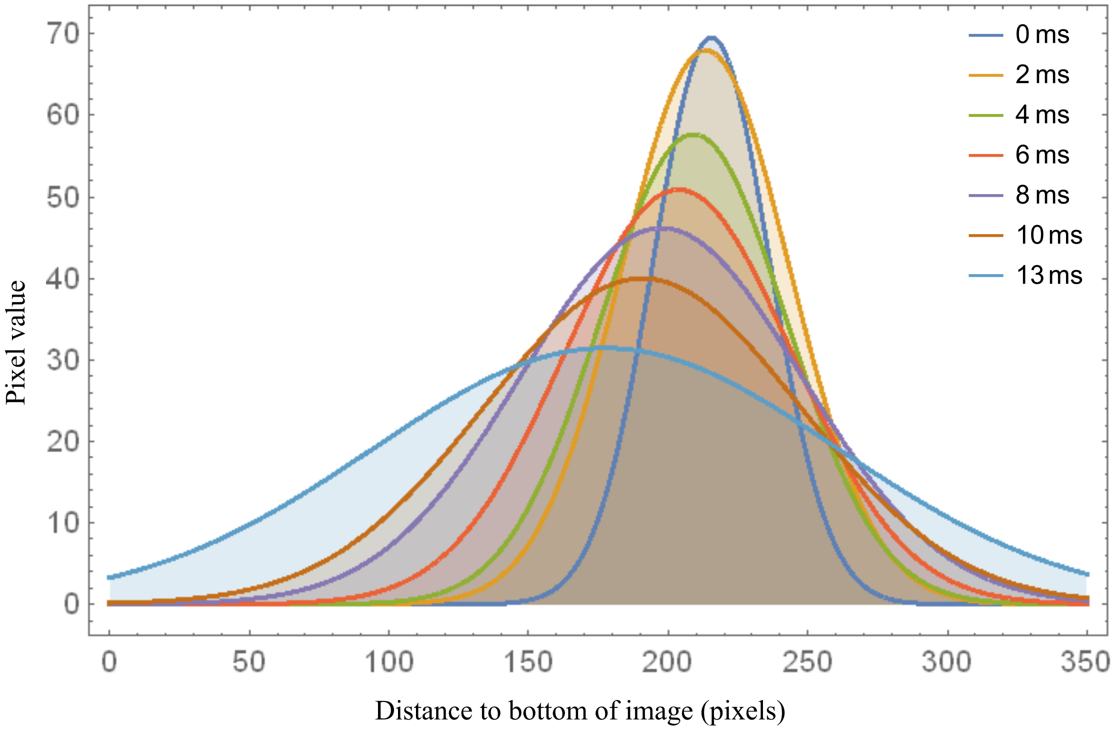

Figure 7.7: Fitted Gaussian models of the absorption image cross sections taken at different intervals after the MOT was turned off.

Figure 7.7 is a plot of the Gaussian models fitted to image cross sections obtained at different intervals. It clearly illustrated what was shown in Figure 7.5 where the atomic density diffused from the center over time while the whole cloud dropped due to gravity. Extracting the width of these curves and using equation 7.4, the temperature obtained from each of these models are shown in Figure 7.8.

The temperature measurements obtained from the first 3 ms of expansion seemed to provide poor agreement with the rest of the measurements. This was not too surprising

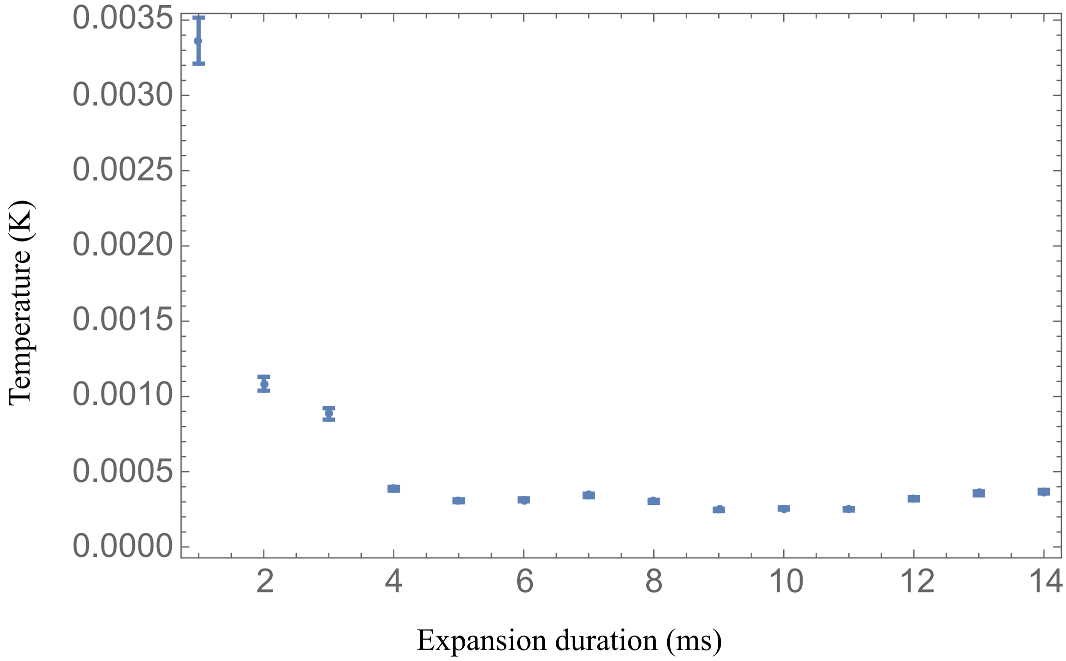

Figure 7.8: Temperature of the MOT before expansion as measured using images taken after different expansion durations.

since from Figure 7.7, it can be seen that the atomic distribution had yet to change very much both in terms of position and width. As a result, the effect of error was more significant for these measurements. The error bars were likely underestimated in Figure 7.8 since it did not account of the slight variations in the MOT with every repeated run. The plotted errors were purely from fitting parameter uncertainties. Therefore, averaging all the data points (except the first three) in Figure 7.8, the temperature of the MOT was found to be 0.31 ± 0.05 mK when the trapping was detuned by 19 MHz.

The above measurement was repeated for other trapping parameters and it was found that generally, the optimal time for temperature measurements was at 5 ms of expansion duration. This time was after the window of poor measurement accuracy of 0 - 3 ms. When the atoms were trapped with less ideal parameters, it was found that after 5 ms, the cloud would have diffused too much to be visible over the background light. Therefore, for consistency, temperature measurements for the rest of this chapter were made at 5 ms of expansion time.

To get an idea of how well the experiment already ran as a starting point before the optimization process, the temperature of typical trapping sequences used to operate GEM were analyzed. The run sequence is detailed in Figure 7.9.

First, by setting $t_{pgc} = 0$, the effect of the compression was observed and the temperature due to compression was measured to be 1.3 ± 0.5 mK. This was not too surprising given the act of compression was expected to raise the temperature of the atoms. The effect of this was minimized in the experiments using the PGC phase. For $t_{pgc} = 1$ ms, $T = 0.15 \pm 0.06$ mK and for $t_{pgc} = 2$ ms, $T = 0.13 \pm 0.04$ mK. Clearly, the effect of the PGC phase was significant for cooling down the cloud. The parameters used to generate these MOTs were largely arrived upon over the years through educated estimations from other systems and trial and error. The results had proven to have done quite well but there was room for further optimization.

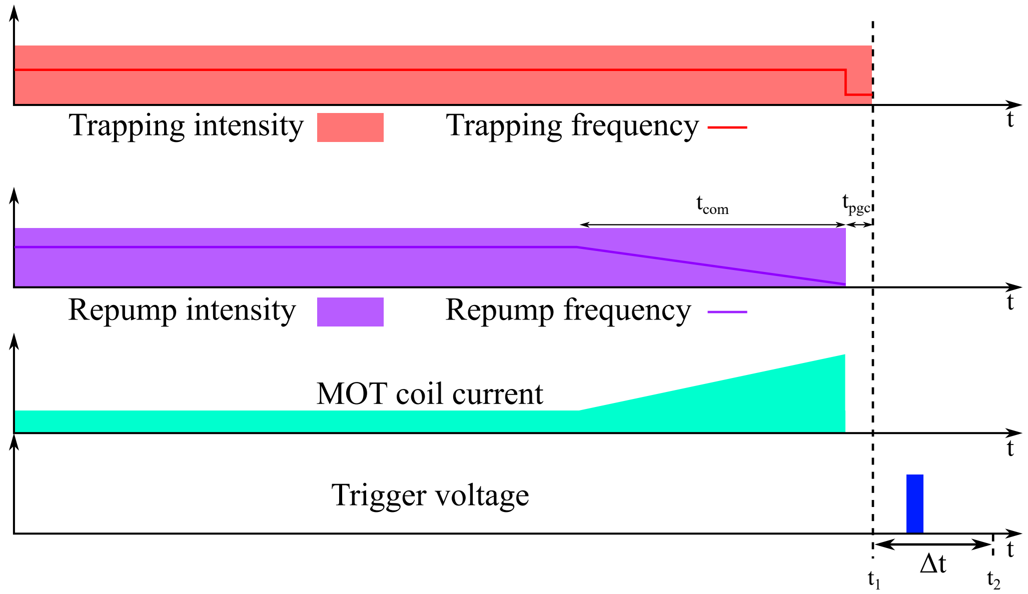

Figure 7.9: The typical run sequence used to form the MOT during a memory experiment. After forming the MOT in steady state for typically $0.3 - 0.4$s, the gathered atoms were compressed by increasing the current in the MOT coils to increase the number of atoms in the path of the memory pulse over a time period of t_{com}. The repump frequency red detuning was also increased linearly during compression as that reduces the outward radiation pressure due to scattering inside the cloud which made for a better compression [42]. The coils and repump beam were then switched off while the trapping continued for a time of t_{pgc} to do PGC cooling on the atoms. t_{pgc} is typically $1 - 2$ ms long and the trapping detuning is increased during this time for more efficient cooling. After which the trapping goes off as well since they cannot be on during the memory experiment. In the case of measuring temperature, they were turned off to allow for expansion imaging.

7.5 Atomic density measurements

There were two main possible methods to measure the absolute number of atoms inside the trap. One could either set the imaging beam to be exactly on resonance and then measure the transmitted light through the MOT and use that to calculate the optical depth. This was not possible for this gas cloud since it was too dense as shown in Figure 7.1. Another method was to set the imaging beam well detuned from the transition (about 20 MHz) and then scale the optical depth back to the on resonance optical depth using the detuning and linewidth of the transition using equation 6.4. Unfortunately, this method was not viable either since the absorption signal became very weak at detunings that far and no appreciable measurement above the noise level could be obtained. A measurement of smaller detuning was not usable either as the high density cloud would have caused lensing of the imaging beam as it scattered light at an angle and made it difficult for accurate measurements. Therefore, it was decided to obtain a measure of the number of atoms just by integrating over the fitted Gaussians. It was not possible to derive the absolute number of atoms in the trap using this measurement but it did give a measure of the relative number of atoms which could be used to compare between different parameters.

7.6 Parameter sweeps

For quantum memory purposes, two of the most important properties of the MOT are its temperature and density. The temperature limits the storage time of the memory as that determines how quickly the atoms move while the density affects the amount of atoms available to absorb the storage light. Therefore, both of these were the main properties to optimize. The parameters that were used for this optimization were the trapping frequency and the repump intensity. The frequency of the repump in general was run at 1 MHz blue-detuned but since the width of the transition was 6 MHz, this was effectively on resonance. It was observed that changing the repump frequency or the trapping intensity did little to affect the performance of the MOT. Though it would have made sense for the repump to be ran at red detuned frequency to give it additional cooling using its configuration but it was likely that this effect was not observed strongly since the repump did not interact with a cycling transition that made for effective cooling/trapping.

For the following parameter sweeps, the run sequence used were similar to the one illustrated in Figure 6.8 used to form a simple MOT.

7.6.1 Sweeping trapping frequency

The trapping frequency was increased from -41 MHz to -11 MHz detuned in steps of 0.75 MHz. The experiment was repeated 20 times at each step; 10 times each for the initial and expanded atomic cloud images. The intensity of the trapping and repump beams were 77.6 ± 0.5 mW/cm^2 and 15.5 ± 0.5 mW/cm^2 respectively. The MOT temperature with respect to trapping frequency detuning with these parameters is shown in Figure 7.10.

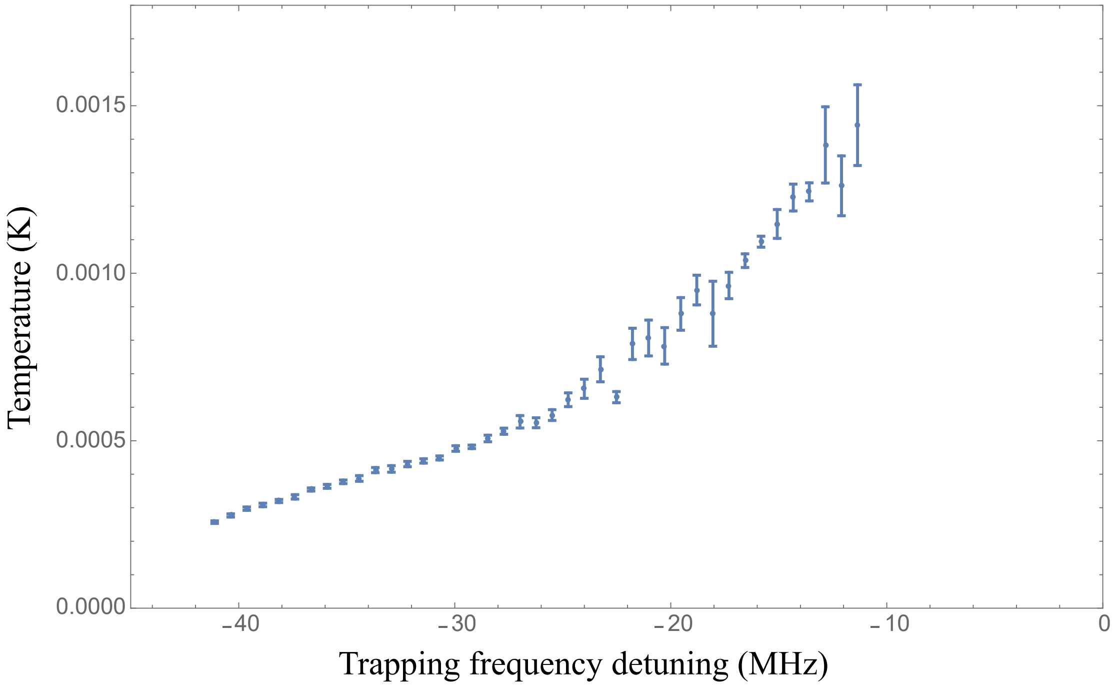

Figure 7.10: Temperature of the MOT with respect to trapping frequency detuning.

By integrating over the fitted Gaussian models, a measure of the number of atoms were also obtained and plotted in Figure 7.11.

Figure 7.10 showed that temperature was significantly lower with larger frequency

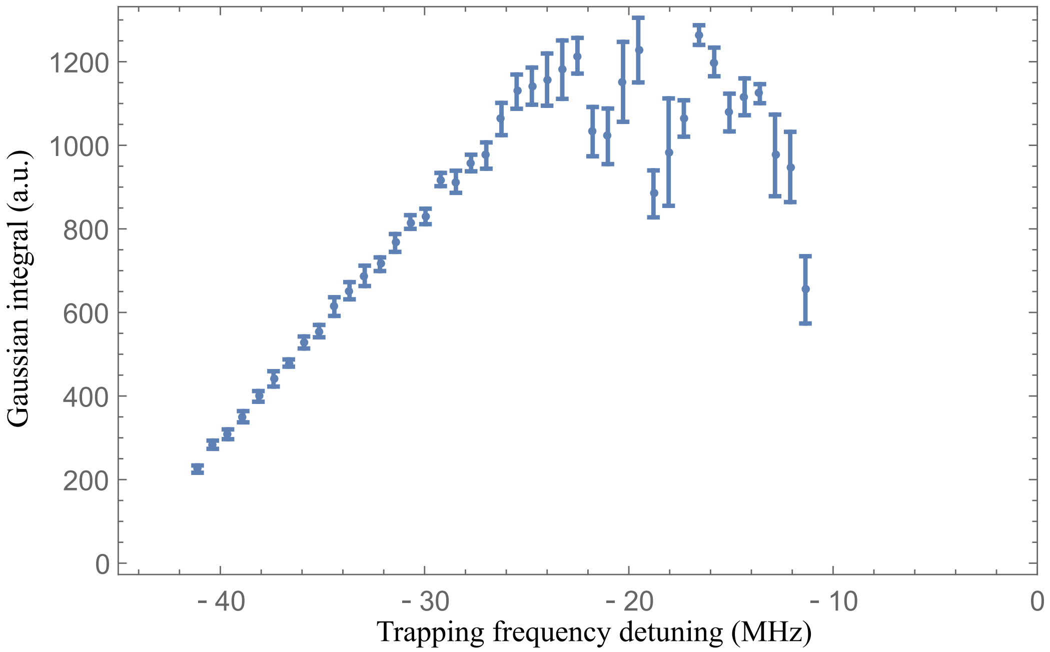

Figure 7.11: Relative number of atoms trapped against trapping frequency detuning.

detunings. At a detuning of 41 MHz, the temperature was down to 253 ± 4 μK. Note that absolute comparisons between measurements made on different days could not be made. This was due to a number of reasons. The intensity of the beams varied everyday largely due to the tapered amplifiers. The number of atoms released by the rubidium dispenser fluctuated greatly from day to day. Given the large number of parameters that could vary from day to day, absolute comparisons could only be made with data taken on the same day.

Therefore, one could see that compared to the usual operating detuning at 19 MHz, clearly there was room for improvement in the temperature by increasing the detuning. This behavior implied that despite the magnetic fields and being above the Doppler temperature (146 μK [11]), the effect of PGC was still significant. This was because this agreed with the increasing effectiveness of PGC with increased detuning as shown in equation 4.23. Neither optical molasses nor the MOT operation temperature would have had such a strong temperature dependence on the detuning.

One of the major reasons why the operation detuning was chosen to be smaller for memory experiments was due to the large number of atoms that it trapped. As can be seen from Figure 7.11, the maximum number of atoms trapped occurred at around 20 MHz detuning. The lack of atoms at larger detunings were simply due to the weaker interaction between the trapping field and the atoms which caused fewer atoms to be trapped.

In both plots, a common feature was the increasing uncertainty in the measurements at detunings smaller than 20 MHz. They were a result of large fluctuations between each repetition of the experiment. It was observed that at small detunings like this, the shape of the gas cloud started to oscillate with clusters of atoms moving back and forth along the z direction. This is shown in Figure 7.12.

As a result, the images obtained from the repeated runs varied greatly. The reason for this instability was thought to be from radiation trapping where the large atomic density caused scattered photons to be reabsorbed by atoms and not being dissipated out of the MOT. This created an outwards radiation pressure inside the cloud and pushed atoms

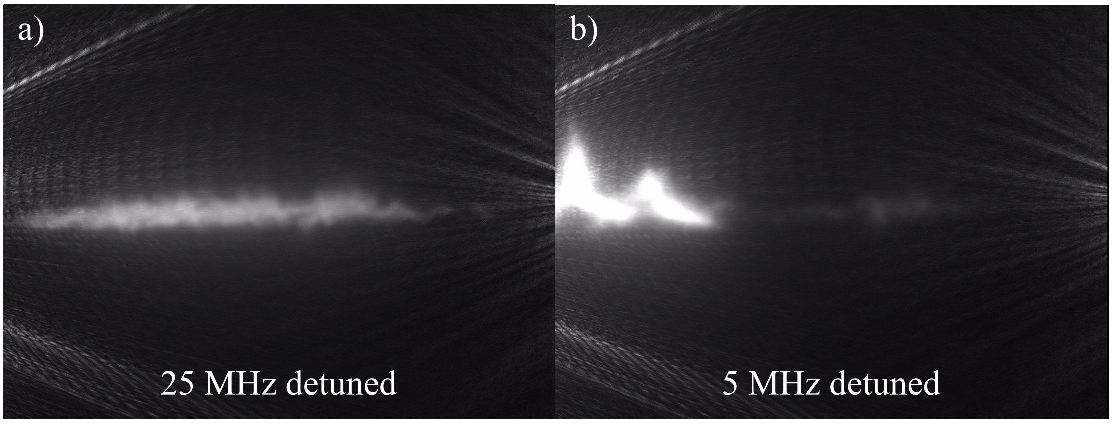

Figure 7.12: Florescence imaging of the MOT during the loading phase comparing the cloud with trapping detuned at a) 25 MHz and b) 5 MHz. Fluorescence images had to be used here since radiation trapping caused instabilities in b) that can only be observed with the trapping fields on. The cloud gets pushed upwards and towards the side since the retro-reflected trapping beams are weaker after scattering off the gas chamber walls.

towards points of lower potential generated through misalignment of the beams. [43]

From sweeping the trapping frequency, it could be seen that the temperature of the cloud was minimized with increasing detuning but at the sacrifice of the number of atoms trapped. Detunings smaller than 20 MHz were not ideal since radiation trapping severely compromised the stability of the gas cloud.

7.6.2 Sweeping repump intensity

To ensure more of the parameter space was observed, a two dimensional parameter sweep was done using the trapping frequency and repump intensity. The trapping intensity remained the same while the trapping detuning was scanned from 17 to 42.5 MHz and the repump intensity was changed from 13.5 to 17.0 mW/cm^2. The results were plotted in Figure 7.13 and 7.14.

Clearly, changing the repump intensity within this range had a negligible effect on the temperature or the density of the MOT. Even though the repump intensity was already reduced below the level typically used before to form the MOT, this indicated that it was still powerful enough to saturate the $F = 1 \rightarrow F' = 2$ transition. Although changing its intensity had negligible effects, it was logical that reducing its power was probably better for the MOT's performance as it meant less unnecessary energy was being fired at the cold atoms.

To further investigate, the repump intensity was dropped until an appreciable effect on the MOT was observed as shown in Figures 7.15 and 7.16.

Figure 7.15 showed that at 0.9 mW/cm^2, a strong threshold effect was observed with the temperature as a result of there being too few atoms trapped in the MOT. Unfortunately, a finer resolution of the repump intensity was difficult to achieve close to this threshold as the variable attenuators were very nonlinear in this regime. A more gradual decrease was observed with the atom number with dropping repump intensity.

Changing the repump intensity was expected to change the atomic density by controlling the number of atoms that were in the trapping transition. Figure 7.16 supported this. As long as the atoms were not in the radiation trapping regime, the temperature of the

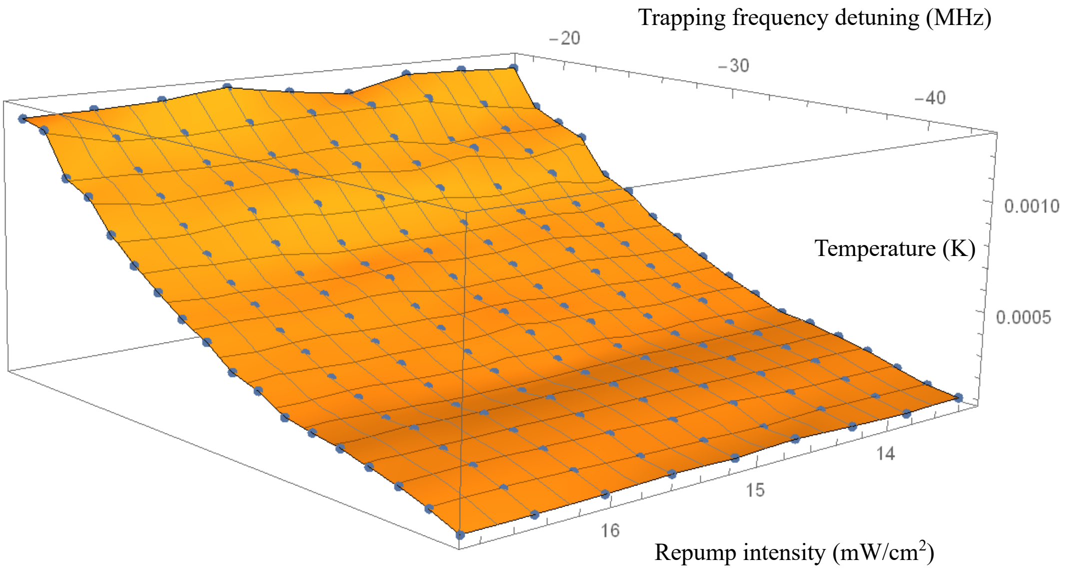

Figure 7.13: Temperature of MOT with respect to repump intensity and trapping detuning.

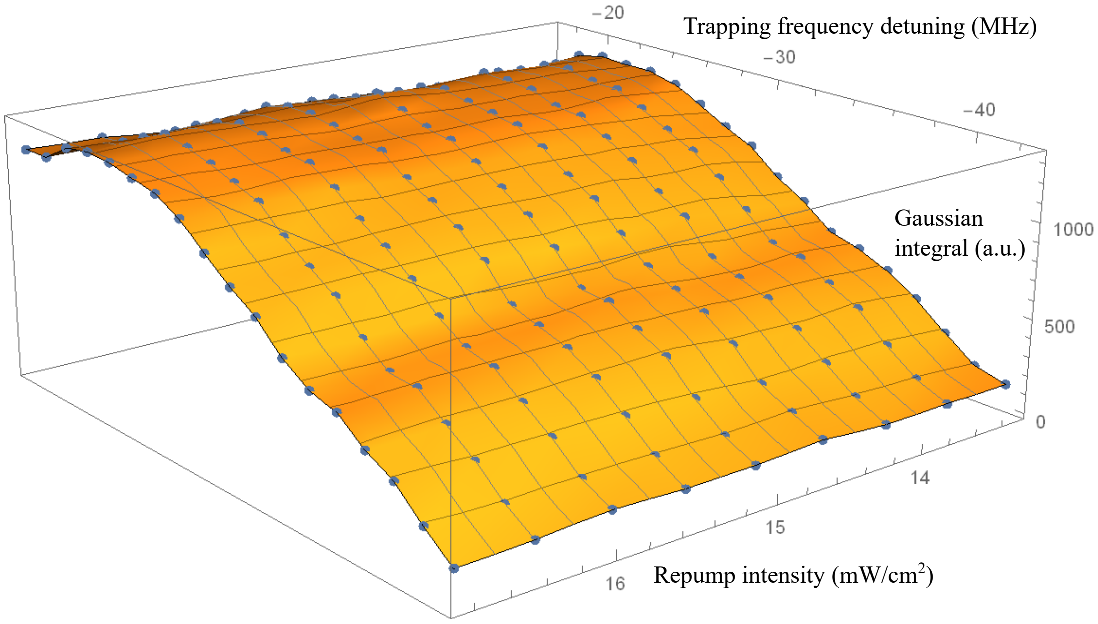

Figure 7.14: Gaussian integral of absorption image cross sections with respect to repump intensity and trapping detuning.

cloud should not have had a strong dependence on the repump intensity as demonstrated in Figure 7.15. Note that this set of measurements were not done on the same day as the set of measurements in Figure 7.13 and 7.14. Hence, direct comparisons between the two could not be made. However, trends from both sets of data suggested that the atom density leveled off with increasing repump intensity after about 5 mW/cm^2. They both also agreed with the idea that the temperature had negligible dependence on the repump intensity.

The above observations illustrated that the intensity of the repump beam was not essential to optimizing either the MOT temperature or density. As long as it was above

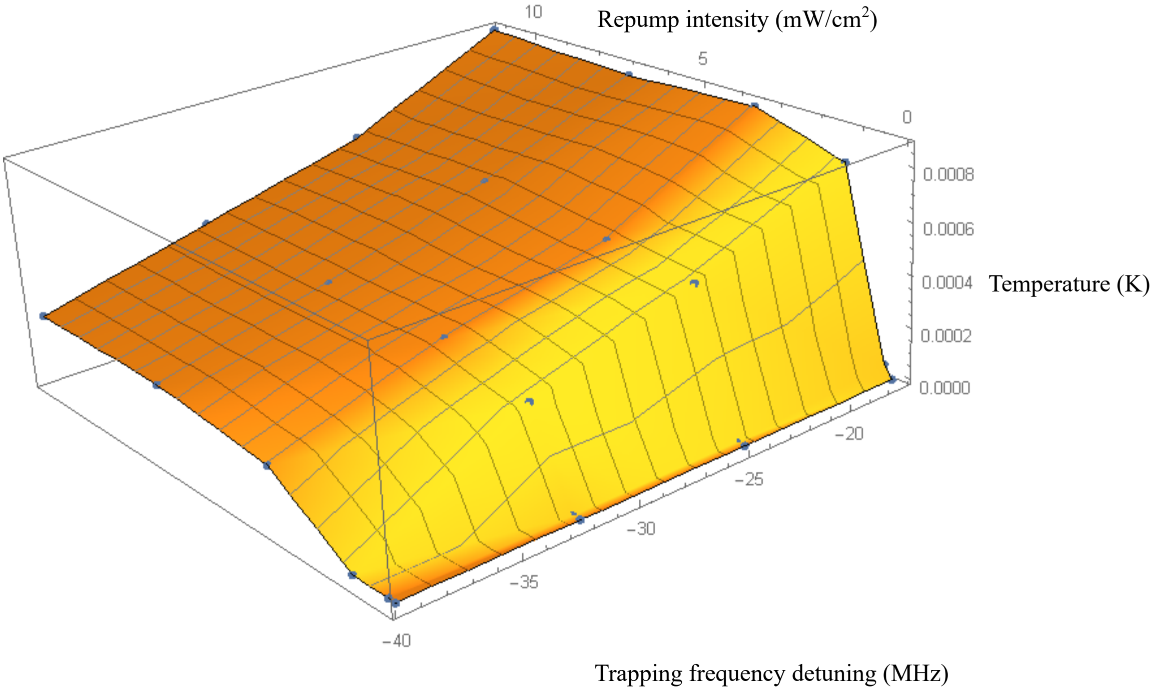

Figure 7.15: Temperature of MOT with respect to repump intensity and trapping detuning. Note the temperature did not drop to zero at low repump intensities, the zero values were a result of no atoms being trapped.

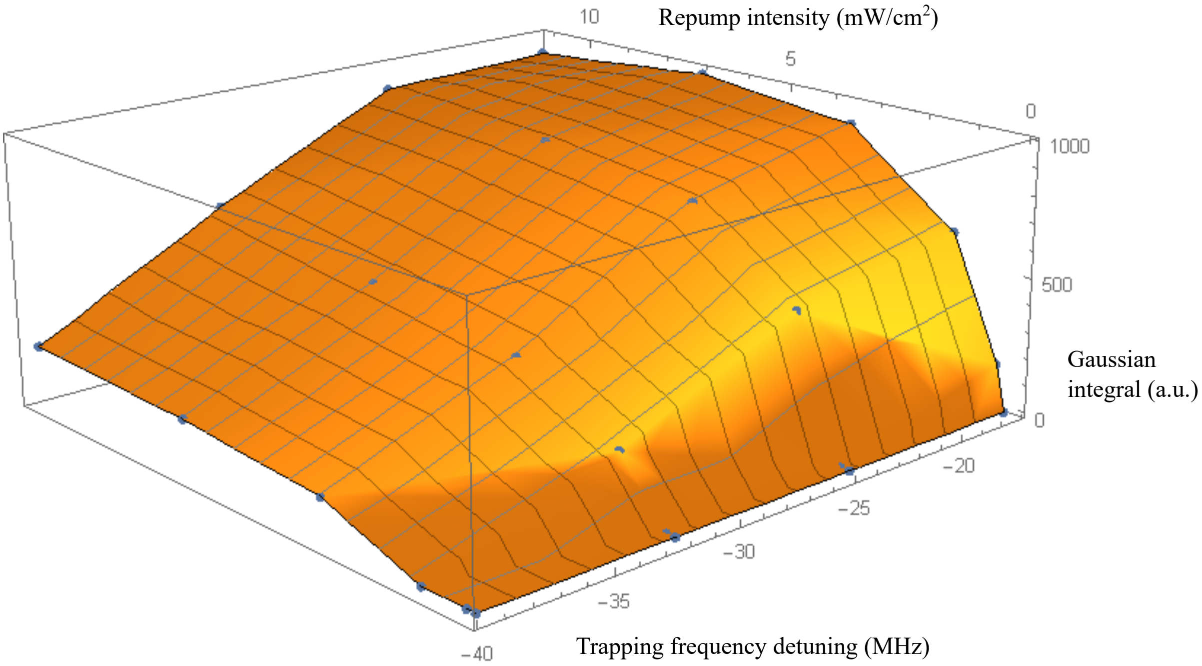

Figure 7.16: Gaussian integral of MOT cross section with respect to repump intensity and trapping detuning.

5 mW/cm^2, the maximum number of atoms trapped as controlled by it would plateau as the transition was already saturated.

7.7 Trapping sequence optimization

From what was observed in the previous section, the main controlling factor of the temperature of the cloud was the trapping frequency. Therefore, to further push the temperature down while maintaining a dense cloud, one could start the trapping phase using a small detuning of about −20 MHz to maximize cloud density and when enough atoms have been trapped, the detuning could be pushed even further than it was before down all the way to −45 MHz as opposed to the previous −40 MHz for an even more aggressive PGC phase. Through some further trial and error the sequence shown in Figure 7.17 was achieved.

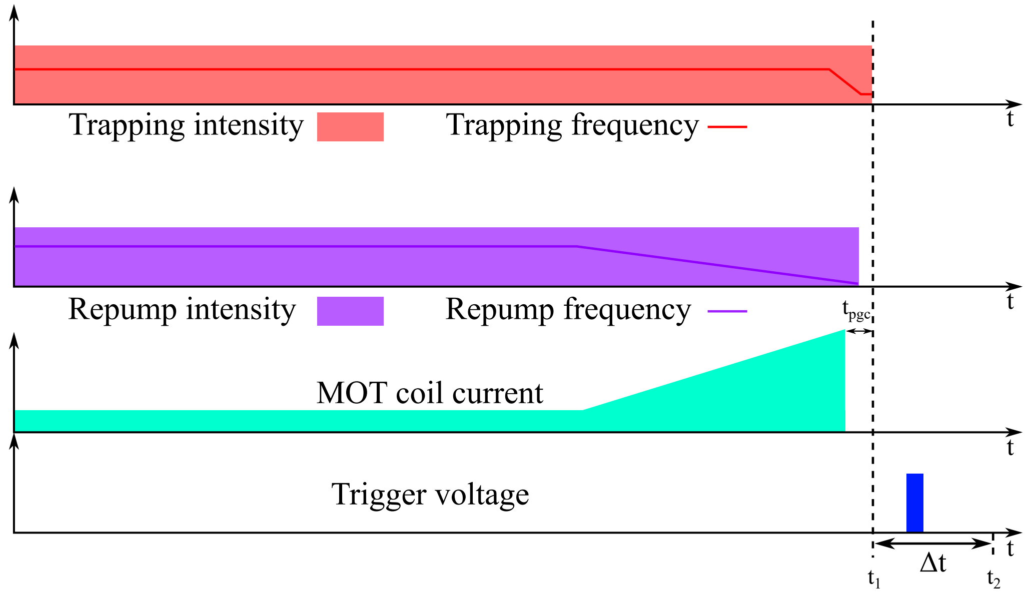

Figure 7.17: Improved cooling and trapping sequence based on what was observed with the parameter sweeps and some trial and error.

It was observed to have better results when the trapping frequency was changed gradually starting from during the compression phase. Also, extending the repump into part of the PGC phase also made sense given it kept atoms in the cooling transition. With this sequence, the measured temperature of the cloud was 0.20 ± 0.05 mK. Though this temperature seemed fairly similar to the initial temperatures of the original sequences given their uncertainty, it was difficult to make direct comparisons between these measurements as many aspects of the system both in the digital design and the optical configurations have changed over time between they were taken. However, one thing that was quite clear was that the compression phase in Figure 7.17 was more aggressive as the rate of increase in the current supplied to the MOT coils was larger. This should have created denser clouds. Therefore, to be able to achieve similar temperatures despite this, implied that this new and optimized sequence improved both the temperature and density of the MOT.

7.8 Summary

This section described how absorption images were optimized using the imaging beam and a model for the cloud expansion was derived. The procedure for analyzing the images for a fitted Gaussian profile was presented and it was optimized for analyzing large sets of images. Parameter sweeps of both trapping frequency and repump intensity were done to explore their impact on the temperature and density of the cloud. It was found that larger trapping frequency detunings favored lower temperatures at the expense of density. At trapping frequency detunings less than 20 MHz, radiation trapping became significant and caused great instabilities in the cloud. Meanwhile, it was discovered that the repump intensity previously used for typical memory experiments was completely saturating the transition; only 5 $\mathrm{mW/cm^2}$ was required to ensure no atoms were accumulating in the wrong ground state. Using all these findings, a new and improved trapping and cooling sequence was developed and it demonstrated better performance in both cooling and trapping. In addition, included in the appendix, similar parameter sweeps were made on Rb-85 atoms.

Chapter 8

Optical lattice and superradiance

One important but unexpected observation in addition to everything discussed in the previous chapter was the coherent emission that was observed along the axial direction of the MOT when the atoms were being trapped. Unlike simple fluorescence, the light coherently emitted from the trapped cloud had both a well defined direction and phase. This effect has been observed in [44] and was referred to as superradiance where the interaction between the atoms and their spontaneous radiation results in coherent emission. An in depth general theoretical description of this effect can be found in [45]. This section briefly investigates its impact on the performance of the trap.

8.1 Characterizing the emission

The setup for characterizing the emission is shown in Figure 8.1.

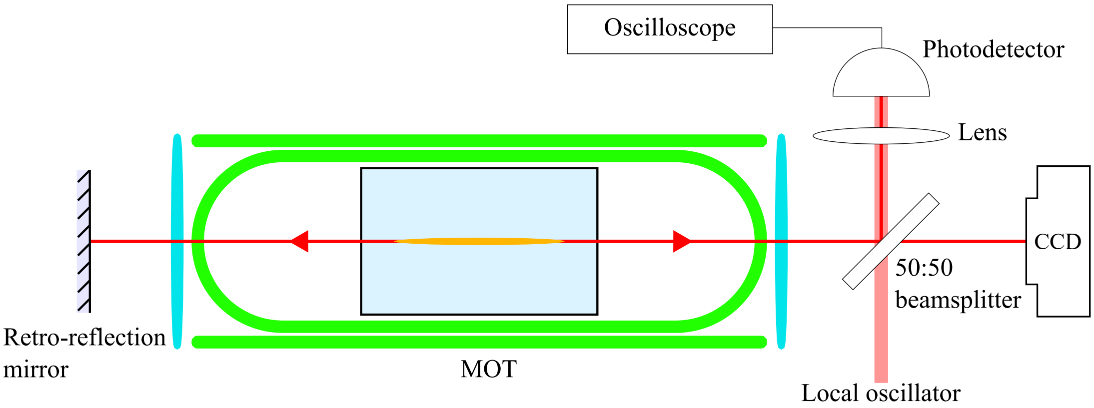

Figure 8.1: Setup for characterizing the MOT emission. The emission from one side could be retro-reflected through the MOT. A 50:50 beamsplitter was used so the emission could be observed both on a CCD camera and on a photodetector.

A variety of observations have been made using this setup noted as follows.

8.2 Observations

To measure the frequency of this emission, it was interfered with a local oscillator beam derived from the trapping beam as shown in Figure 6.2. The resulting beat note was at the frequency difference between the emission and local oscillator which can be measured using the photodetector. The electronic signal from the detector was sent to an electronic signal analyzer where a mixing operation was performed to obtain the frequency components in the signal. The local oscillator frequency was tuned 10 MHz below the trapping frequency and the beat note frequency spectrum showed a peak at 10 MHz with a linewidth of about 200 kHz. As the frequency detuning of the local was changed, the frequency of the beat note remained the same as the the frequency detuning of the local oscillator. This means that this emission was at exactly the same frequency as the trapping beams and not the trapping transition.

Next, the emission was imaged on a camera as shown in Figure 8.2a.

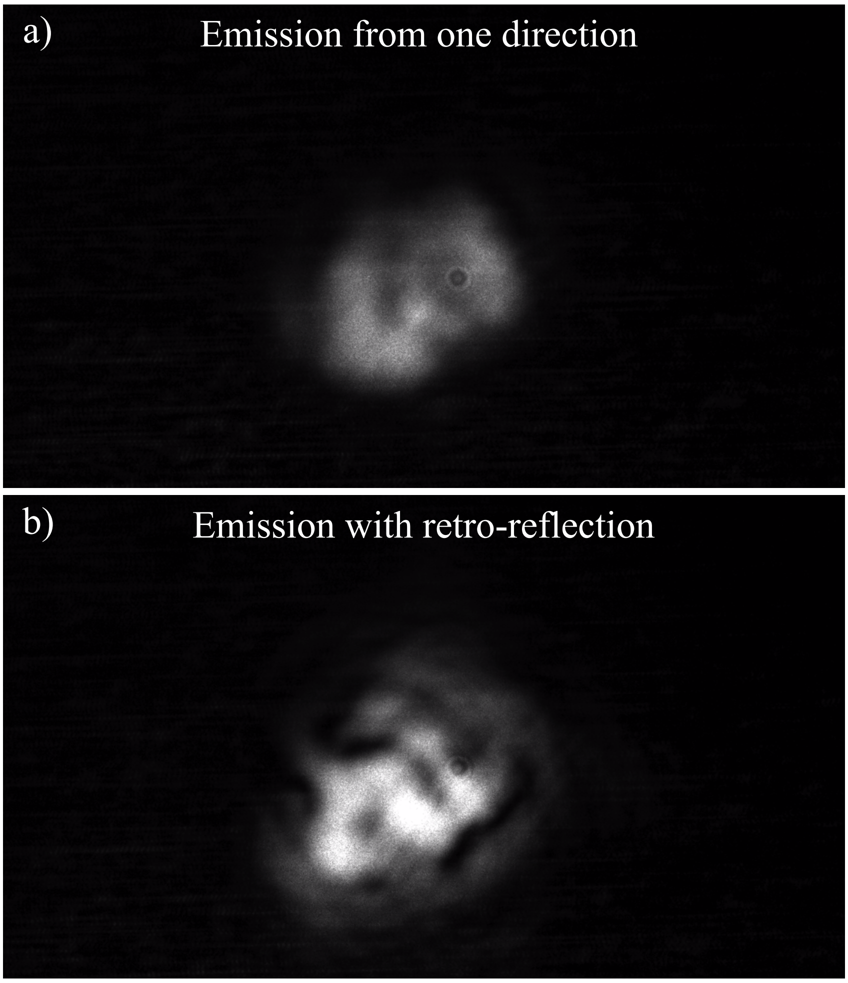

Figure 8.2: Image of MOT emission a) directly from one side of the MOT and b) with the retro-reflection mirror reflecting the emission from the other side back through the atoms.

The observed profile showed complex spatial structure. A number of reasons were hypothesized for causing this complexity; it could have been caused by atomic density distribution within the MOT or the nature of the emission was just very multimodal. The emission from the other side was retro-reflected back through the MOT to give Figure 8.2b. It seemed like the emission experienced some level of gain from this but direct measurements on a photodetector are needed to confirm whether this was true and if so how much gain it was exactly.

Also, regular periodic oscillations in the emission power was observed. A time based trace of the total emission power as focused onto a photodetector and measured by an oscilloscope is shown in Figure 8.3.

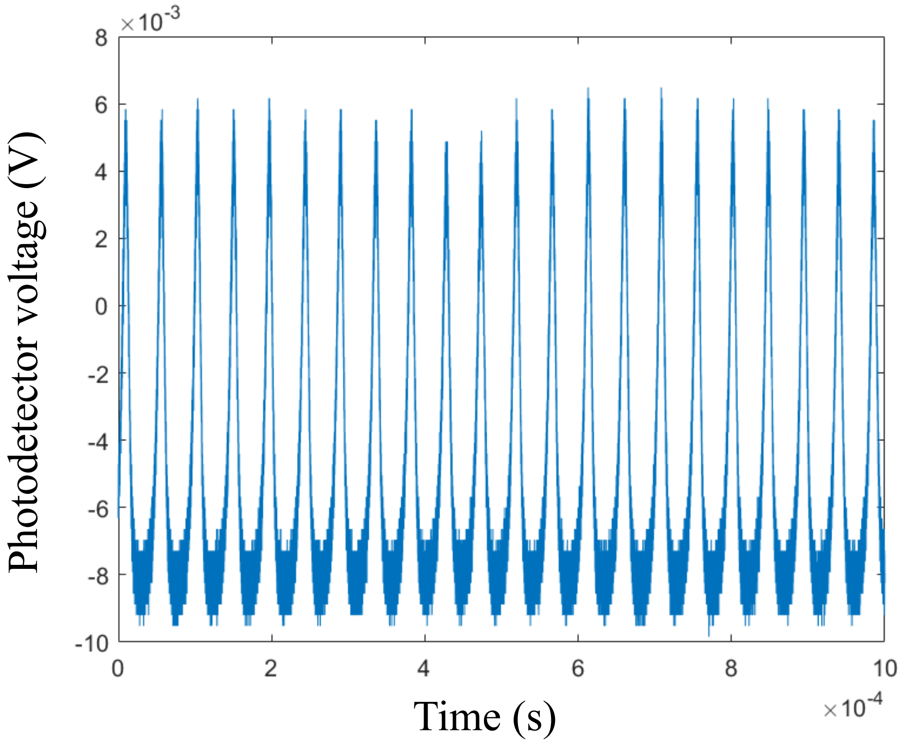

Figure 8.3: Oscillations in the emission power as measured on an oscilloscope through a photodetector. These oscillations were observed when the atoms were trapped in a steady state MOT with a trapping frequency detuning close to 40 MHz.

The emission was observed to be the most intense at large trapping frequency detunings around 30 - 40 MHz. Generally, the oscillation modes were much more pronounced and more often observed with the retro-reflection. Excitation of the emission into these oscillation modes happened at random but generating acoustic vibrations on the optics table could often send it into the oscillation mode with varying degrees of success. The frequency of these oscillations did not stay particularly constant as they varied between 25 - 35 kHz. To investigate the frequency components of these oscillations and how changing the trapping parameters affected them, a sweep of the trapping frequency was done, similar to the one in Figure 7.10. The emission detected by the oscilloscope was recorded and a Fourier transform was performed on them. The results are shown in Figure 8.4.

The emission intensity peaks at a trapping frequency detuning of -47 MHz with oscillation frequencies mostly concentrated between 30 - 40 kHz. Generally, the emission seemed to contain a wide range of frequency components peaking at 20 - 40 kHz. Also, the plot shows various noise sources that had little to do with the emission at 20, 70 and 100 kHz. These were likely electronic noise from various components but further investigation was needed to determine their exact source. Note that compared to previous trapping frequency sweeps, it was possible to go to larger frequency detunings, up to 55 MHz, as to get emission, the density of the cloud can be much lower as no expansion imaging was necessary.

Initially, instead of the 50:50 beamsplitter in Figure 8.1, a PBS was previously used as it was assumed that the emission with its complex structure might have had random polarization. However, while observing one of the large oscillations, the intensity of the image on the CCD was observed to change more significantly than expected. Since swap-

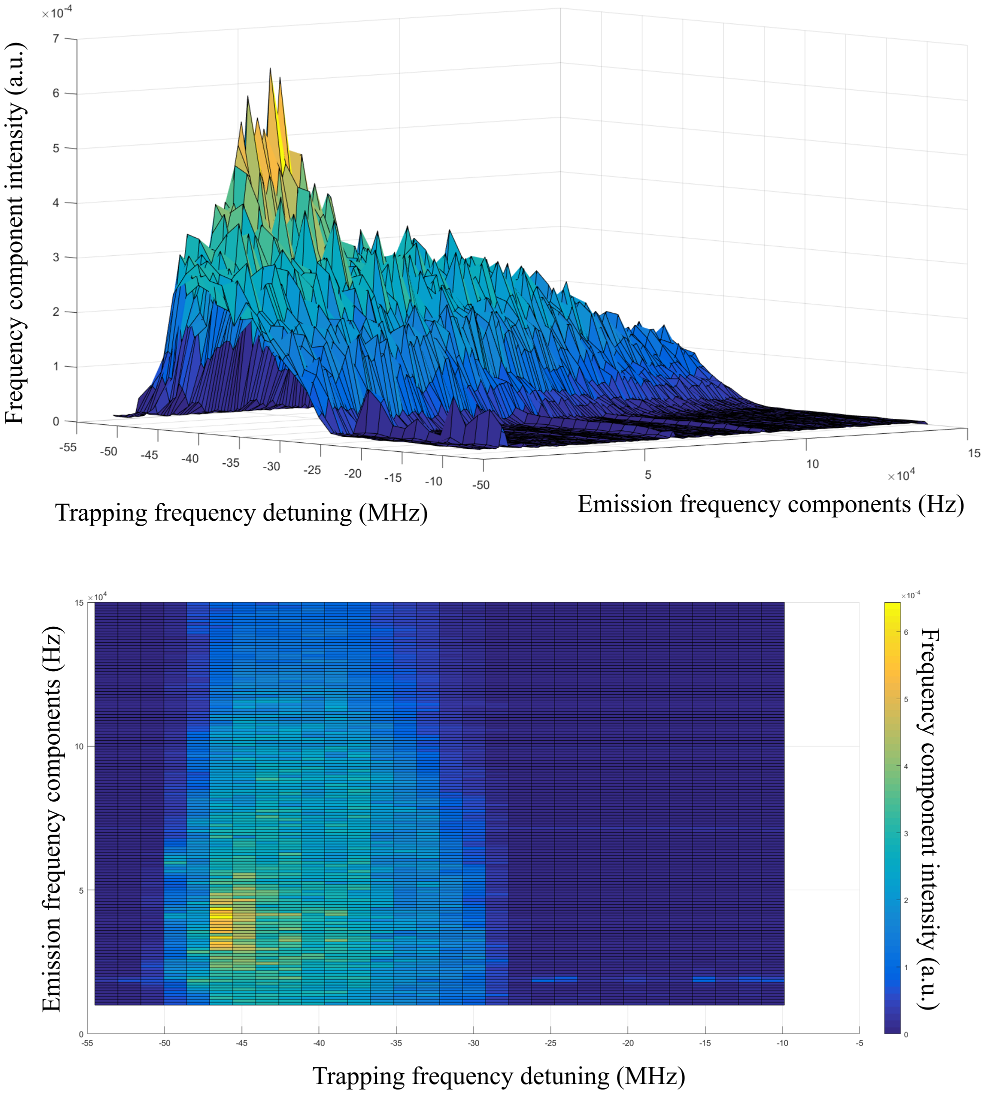

Figure 8.4: Intensity of frequency components of the MOT emission at different trapping frequencies.

ping in a 50:50 beamsplitter mitigated this effect, clearly, the emission had a preferred polarization. It was then noticed there was a strong correlation between the spatial modes observed on the camera and the oscillation mode; during oscillations, the mode intensity profile will consistently change between two different spatial modes.

8.3 Discussion

To be able to coherently scatter light as observed implied there was some level of regular structure within the cloud of atoms like an optical lattice. The radiation forces model of the MOT presented in Chapter 4 is insufficient to fully describing the system; as the previous chapter has showed, polarization gradient cooling formed with the periodic potentials had a significant contribution to the system even in the steady-state MOT configuration. With this, it might be logical to expect the relative phase between all the trapping beams to need to be well defined/controlled to generate a stable optical lattice using the dipole potentials.

This implies the system in this report would be unable to generate an optical lattice. However, results reported in [46] indicated that actually if the MOT was cold enough, the system settled into an optical lattice anyway and was affected very little by changes in the relative phase. This agreed with how the emission intensity was the greatest at larger detunings; Figure 7.10 showed that larger detunings meant lower temperatures. The lower temperatures might have allowed the atoms inside the cloud to settle into an optical lattice and thus coherently scatter light from the trapping beams. Also, qualitatively comparing Figure 8.4 and 7.11, it was likely that the emission dropped off at high detuning simply because too few atoms remained trapped which led to an unsurprising drop in the light scattered. At the other end, Figure 7.10 suggested that the emission intensity dropped off at around trapping frequency detuning of 25 MHz possibly due the cloud being too warm to form a strongly organized optical lattice anymore.

Unfortunately, there were no clear clues as to the exact mechanism causing the large oscillations observed in Figure 8.3. One possible hypothesis is that they were a result of a competition between heating and cooling mechanisms. The peaks in the oscillation corresponded to an structurally organized cloud which results in a peak in the scattered light. However, this scattered light might have then caused heating inside the cloud which disorganized the lattice and breaks the coherent scattering. As the atoms get cooled again, the process repeats. However, this model remains to be confirmed. Through the observations of the emission and its oscillations made so far in tandem with the absorption imaging measurements, there had not been a obvious correlation between the temperature and the emission. However, given the emission propagates axially, it was entirely possible that the radial expansion of the cloud as imaged was completely unaffected by this emission. Rather, it was possible that its effects on axial expansion was more significant.

The emission observed was very similar to what was reported in [44] where a similarly shaped MOT of Rb-87 atoms also emitted light in the axial direction. They described the effect as a form of superradiance. Superradiance is a phenomena seen in Bose-Einstein condensates where light is coherently scattered from an atomic density grating. To generate this atomic grating, the location of the atoms need to be well defined on the scales of the wavelength of the scattered light, effectively requiring an optical lattice. The authors of [44] suggested that this emission interacted with the atoms to strengthen and stabilize the optical lattice structure which resulted in further enhancements to the emission. One key difference between their system and this one was the larger number of trapped atoms trapped in this one which might have led to the oscillations that they did not report.

Chapter 9

Conclusion and future work

This experiment was done in order to both investigate and optimize the operation of the cold atom trapping system for quantum memory purposes. A general theoretical overview for cooling and trapping of atomic ensembles was presented by outlining relevant theory on atomic structure and atom light interactions. This created a framework for discussion of the mechanism behind various atomic cooling and trapping schemes. A detailed overview of the experimental configuration was then presented. Descriptions and explanations on preparations of the various beams and magnetic fields required to create a magneto-optical trap were provided. Absorption imaging was the main method of extracting information on the atomic cloud's temperature and density. Both of these properties have direct consequences on the performance of the quantum memory; the temperature determines the rate of diffusion of the cloud which affects the memory lifetime while the density determines how many atoms are available to interact with the memory light which determines the memory efficiency.

A method to extract information on both of these properties from the absorption images was presented; the cross section density profiles of the cloud were modeled with Gaussian distributions and variations in this Gaussian as the cloud expanded were observed. To minimize the number of relevant parameters, the atoms were cooled and trapped in a simple magneto-optical trap and parameter sweeps on the trapping and repump beams were made. The effect of changing the trapping intensity and repump frequency in the interested range was found to be negligible. It was expected that by pushing the repump frequency into being red detuned from the repump transition, additional cooling might have been observed. However, suspecting the reason being the repump transition not being a closed cycling transition, its contribution to extra cooling seemed negligible. The trapping frequency had a strong influence on the temperature of the cloud. Tuning the trapping frequency further red detuned from the transition brought the temperature of the atoms lower. At a detuning of -41 MHz, the temperature reached down to 257 ± 4 μK. On the other hand, this came at an expense of atomic density as unsurprisingly, being further detuned meant a weaker interaction between the trapping beams and the atoms so fewer atoms were being trapped. Such a strong detuning dependence on the cloud temperature suggested that even in the steady-state MOT configuration, polarization gradient cooling still played a very significant role. At the other end when the trapping detuning was reduced below -20 MHz, significant instabilities to the MOT was observed as a result of radiation trapping. Sweeping the repump intensity in the usual operation range (13 -17 mW/cm^2) showed very little effect on the both the temperature and density of the MOT. This suggested too much repump power had been used in the past which was probably not ideal for the temperature. Further reducing the intensity down below 10 mW/cm^2 proved the repump transition was being saturated at around 5 mW/cm^2 and going down further gradually reduced the cloud density while not affecting the temperatures too significantly.

Finally, coherent emission in the axial direction of the atomic cloud was observed. This emission was generated by coherent scattering of the trapping beams from an atomic density grating in the form of an optical lattice. The emission was the most intense at far detunings of -40 to -50 MHz. It dropped for even further detunings just because there were too few atoms trapped and for smaller detunings, it was suspected due to temperatures being too high for a regular optical lattice to be formed. Large oscillations in this emission was also observed and they were suspected to be attributed to a competition between heating and cooling processes but more investigation was required to confirm this hypothesis.

There are many future directions of investigation left to be explored from ths point. First and foremost, as a direct extension to the work done on parameter sweeps to both better understand and to optimize the system, work is being done to implement machine learning into the system. By giving a computer full control over the parameters of the system while monitoring the property of interest (like temperature and density), the system may be allowed to investigate the parameters on its own to look for more optimized parameters to improve the performance of the system. Since a computer controls this, the parameter sweeps reported here can be enlarged substantially so that it no longer needs to confine the system under investigation as a steady state MOT. It could arrive at unexpected cooling and trapping sequences that might shed more light into the dynamics and mechanism of this system. In addition to the trapping system, machine learning could also be used to improve the performance of the quantum memory as well by giving it control over memory beams and magnetic fields as well.

As mentioned previously, the effects of the axial emission is currently not very well understood. It would be useful to measure how quickly the cloud expands in the axial direction under the effects of this emission. Absorption imaging was not particularly helpful with this measurement but an alternative measurement method was to directly store a pulse in the ensemble and measure the retrieved pulse since changes in the position of the atoms in the axial direction causes a frequency shift and blur the spectrum of the retrieved light. If it turned out that the emission did reduce atomic diffusion in the axial direction, it could be useful for improving the performance of the memory.

Finally, there are a few directions this experiment can go in the future as a quantum memory. Firstly, the experiment so far has only been used to store coherent states of light. It would be important to demonstrate experimentally that it is also compatible with other quantum states of light like single photons. This might entail the construction of a single photon source compatible with this memory. Also, this system has the potential of facilitating photon-photon interactions as they are being stored. This opens up many possibilities such as the construction of quantum optical gates.

Bibliography

[1] T. D. Ladd, F. Jelezko, R. Laflamme, Y. Nakamura, C. Monroe, and J. L. O'Brien, "Quantum computers," *Nature*, vol. 464, pp. 45–53, Mar 2010.

[2] N. Gisin and R. Thew, "Quantum communication," *Nature Photonics*, vol. 1, pp. 165–171, Mar 2007.

[3] A. K. Ekert, "Quantum cryptography based on bell's theorem," *Phys. Rev. Lett.*, vol. 67, pp. 661–663, Aug 1991.

[4] N. Sangouard, C. Simon, H. de Riedmatten, and N. Gisin, "Quantum repeaters based on atomic ensembles and linear optics," *Rev. Mod. Phys.*, vol. 83, pp. 33–80, Mar 2011.

[5] A. I. Lvovsky, B. C. Sanders, and W. Tittel, "Optical quantum memory," *Nature Photonics*, vol. 3, pp. 706–714, Dec 2009.

[6] E. Rutherford, "Lxxix. the scattering of alpha and beta particles by matter and the structure of the atom," *Philosophical Magazine Series 6*, vol. 21, no. 125, pp. 669–688, 1911.

[7] N. Bohr, "I. on the constitution of atoms and molecules," *Philosophical Magazine Series 6*, vol. 26, no. 151, pp. 1–25, 1913.

[8] P. Lambropoulos and D. Petrosyan, *Fundamentals of Quantum Optics and Quantum Information.* Springer Berlin Heidelberg, 2007.

[9] B. Bransden and C. Joachain, *Physics of Atoms and Molecules.* Pearson Education, Prentice Hall, 2003.

[10] A. Corney, *Atomic and laser spectroscopy.* Oxford science publications, Clarendon Press, 1977.

[11] D. A. Steck, "Rubidium 87 d line data," May 2008.

[12] C. Foot, *Atomic physics.* Oxford master series in physics, Oxford University Press, 2005.

[13] R. Loudon, *The Quantum Theory of Light.* OUP Oxford, 2000.

[14] H. Metcalf and P. van der Straten, *Laser Cooling and Trapping.* Graduate Texts in Contemporary Physics, Springer New York, 2001.

[15] C. Cohen-Tannoudji, J. Dupont-Roc, and G. Grynberg, *Atom-photon interactions: basic processes and applications.* Wiley-Interscience publication, J. Wiley, 1992.

[16] J. P. Gordon and A. Ashkin, "Motion of atoms in a radiation trap," *Phys. Rev. A*, vol. 21, pp. 1606–1617, May 1980.

[17] J. Dalibard and C. Cohen-Tannoudji, “Laser cooling below the doppler limit by polarization gradients: simple theoretical models,” *J. Opt. Soc. Am. B*, vol. 6, pp. 2023–2045, Nov 1989.

[18] Y.-W. Cho, G. T. Campbell, J. L. Everett, J. Bernu, D. B. Higginbottom, M. T. Cao, J. Geng, N. P. Robins, P. K. Lam, and B. C. Buchler, “Highly efficient optical quantum memory with long coherence time in cold atoms,” *Optica*, vol. 3, pp. 100–107, Jan 2016.

[19] G. Heinze, C. Hubrich, and T. Halfmann, “Stopped Light and Image Storage by Electromagnetically Induced Transparency up to the Regime of One Minute,” *Physical Review Letters*, vol. 111, no. 3, p. 033601, 2013.

[20] M. Zhong, M. P. Hedges, R. L. Ahlefeldt, J. G. Bartholomew, S. E. Beavan, S. M. Wittig, J. J. Longdell, and M. J. Sellars, “Optically addressable nuclear spins in a solid with a six-hour coherence time,” *Nature*, vol. 517, pp. 177–180, Jan 2015. Letter.

[21] Y.-F. Hsiao, P.-J. Tsai, H.-S. Chen, S.-X. Lin, C.-C. Hung, C.-H. Lee, Y.-H. Chen, Y.-F. Chen, I. A. Yu, and Y.-C. Chen, “EIT-based photonic memory with near-unity storage efficiency,” *ArXiv 1605.08519*, May 2016.

[22] M. Fleischhauer, A. Imamoglu, and J. P. Marangos, “Electromagnetically induced transparency: Optics in coherent media,” *Rev. Mod. Phys.*, vol. 77, pp. 633–673, Jul 2005.

[23] M. Fleischhauer and M. D. Lukin, “Dark-state polaritons in electromagnetically induced transparency,” *Phys. Rev. Lett.*, vol. 84, pp. 5094–5097, May 2000.

[24] C. Liu, Z. Dutton, C. H. Behroozi, and L. V. Hau, “Observation of coherent optical information storage in an atomic medium using halted light pulses,” *Nature*, vol. 409, pp. 490–493, Jan 2001.

[25] L. V. Hau, S. E. Harris, Z. Dutton, and C. H. Behroozi, “Light speed reduction to 17 metres per second in an ultracold atomic gas,” *Nature*, vol. 397, pp. 594–598, Feb 1999.

[26] Y.-F. Hsiao, H.-S. Chen, P.-J. Tsai, and Y.-C. Chen, “Cold atomic media with ultrahigh optical depths,” *Phys. Rev. A*, vol. 90, p. 055401, Nov 2014.

[27] U. Schnorrberger, J. D. Thompson, S. Trotzky, R. Pugatch, N. Davidson, S. Kuhr, and I. Bloch, “Electromagnetically induced transparency and light storage in an atomic mott insulator,” *Phys. Rev. Lett.*, vol. 103, p. 033003, Jul 2009.

[28] M. Greiner, O. Mandel, T. Esslinger, T. W. Hansch, and I. Bloch, “Quantum phase transition from a superfluid to a mott insulator in a gas of ultracold atoms,” *Nature*, vol. 415, pp. 39–44, Jan 2002.

[29] J. Nunn, I. A. Walmsley, M. G. Raymer, K. Surmacz, F. C. Waldermann, Z. Wang, and D. Jaksch, “Mapping broadband single-photon wave packets into an atomic memory,” *Phys. Rev. A*, vol. 75, p. 011401, Jan 2007.

[30] B. Sparkes, *Storage and Manipulation of Optical Information using Gradient Echo Memory in Warm Vapours and Cold Ensembles.* PhD thesis, The Australian National University, 2013.

[31] D.-S. Ding, W. Zhang, Z.-Y. Zhou, S. Shi, B.-S. Shi, and G.-C. Guo, "Raman quantum memory of photonic polarized entanglement," *Nature Photonics*, vol. 9, pp. 332–338, May 2015. Article.

[32] M. Hosseini, *Quantum Optical Storage and Processing Using Raman Gradient Echo Memory.* PhD thesis, The Australian National University, 2012.

[33] L.-M. Duan, M. D. Lukin, J. I. Cirac, and P. Zoller, "Long-distance quantum communication with atomic ensembles and linear optics," *Nature*, vol. 414, pp. 413–418, Nov 2001.

[34] A. Kuzmich, W. P. Bowen, A. D. Boozer, A. Boca, C. W. Chou, L.-M. Duan, and H. J. Kimble, "Generation of nonclassical photon pairs for scalable quantum communication with atomic ensembles," *Nature*, vol. 423, pp. 731–734, Jun 2003.

[35] J. Simon, H. Tanji, J. K. Thompson, and V. Vuletić, "Interfacing collective atomic excitations and single photons," *Phys. Rev. Lett.*, vol. 98, p. 183601, May 2007.

[36] X.-H. Bao, A. Reingruber, P. Dietrich, J. Rui, A. Duck, T. Strassel, L. Li, N.-L. Liu, B. Zhao, and J.-W. Pan, "Efficient and long-lived quantum memory with cold atoms inside a ring cavity," *Nature Physics*, vol. 8, pp. 517–521, Jul 2012.

[37] M. Hosseini, B. M. Sparkes, G. Campbell, P. K. Lam, and B. C. Buchler, "High efficiency coherent optical memory with warm rubidium vapour," *Nature Communications*, vol. 2, no. 1, 2011.

[38] M. Hosseini, B. M. Sparkes, G. Hetet, J. J. Longdell, P. K. Lam, and B. C. Buchler, "Coherent optical pulse sequencer for quantum applications," *Nature*, vol. 461, pp. 241–245, Sep 2009.

[39] E. D. Black, "An introduction to Pound Drever Hall laser frequency stabilization," *American Journal of Physics*, vol. 69, no. 1, 2001.

[40] D. Schroeder, *An Introduction to Thermal Physics.* Addison Wesley, 2000.

[41] B. M. Sparkes, J. Bernu, M. Hosseini, J. Geng, Q. Glorieux, P. A. Altin, P. K. Lam, N. P. Robins, and B. C. Buchler, "Gradient echo memory in an ultra-high optical depth cold atomic ensemble," *New Journal of Physics*, vol. 15, no. 8, p. 085027, 2013.

[42] L.-S. Yang, B.-T. Han, D.-S. Hong, T. A. Mohamed, and D. J. Han, "Loading and compression of a large number of rubidium atoms using a semi-dark type magneto-optical trap," *Chinese Journal of Physics*, vol. 45, pp. 606–615, Dec 2007.

[43] G. Labeyrie, F. Michaud, and R. Kaiser, "Self-sustained oscillations in a large magneto-optical trap," *Phys. Rev. Lett.*, vol. 96, p. 023003, Jan 2006.

[44] J. A. Greenberg and D. J. Gauthier, "Steady-state, cavityless, multimode superradiance in a cold vapor," *Phys. Rev. A*, vol. 86, p. 013823, Jul 2012.

[45] R. H. Dicke, "Coherence in spontaneous radiation processes," *Phys. Rev.*, vol. 93, pp. 99–110, Jan 1954.

[46] H. Schadwinkel, U. Reiter, V. Gomer, and D. Meschede, "Magneto-optical trap as an optical lattice," *Phys. Rev. A*, vol. 61, p. 013409, Dec 1999.

Matlab code for temperature analysis

Below is an example of the Matlab code used to extract temperature and density measurements from sets of absorption images. This code was used to extract data from a simple trapping frequency sweep. Note that variations can be easily added to accommodate for images taken on multi-variable sweeps.

```
file_list1 = ls('Sweep0ms');    %Reads the list images before expansion
file_list2 = ls('Sweep5ms');    %Reads the list images after expansion
initialtime = 0;
finaltime = 0.005;              %Expansion duration
iteration = 10;                 %Number of repetitions
calibration = 3.05372*10^(-5);  %Calibration factor
[n1,~] = size(file_list1);      %Number of images
[n2,~] = size(file_list2);
dark_image(:,:) = double(imread('dark_image.bmp')); %Reads dark image
[dim1,dim2] = size(dark_image);     %Dimensions of images
imagesinitial = zeros(n1,dim1,dim2);%Creates empty arrays to load image data
imagesfinal = zeros(n2,dim1,dim2);


%%%%%%Reading in the image files as arrays and extracting paramter information
    from file names
for i = 1:n1 %For images before expansion

    tokens = regexp(file_list1(i,:), '(\(Trap Freq\.\_\d\.\d\)\(Scope Trig_1\.0
        \)\d\d\d\d\d).bmp', 'tokens');
    tokens1 = regexp(file_list1(i,:), '(\(Trap Freq\.\_\d\.\d\d\)\(Scope Trig_1
        \.0\)\d\d\d\d\d).bmp', 'tokens');
    if ~isempty(tokens)
        fn1 = fullfile(cd,'Sweep0ms',file_list1(i,:));  %Image directory
        trappingfreq(i,:) = str2double(file_list1(i,13:15)); %Extract parameter
            value from file name
        imagesinitial(i,:,:) = imread(fn1); %Reads image into array
    end
    if ~isempty(tokens1)
        fn1 = fullfile(cd,'Sweep0ms',file_list1(i,:));
        trappingfreq(i,:) = str2double(file_list1(i,13:16));
        imagesinitial(i,:,:) = imread(fn1);
    end
end
```

```
trappingfreqmean = arrayfun(@(i) mean(trappingfreq(i:i+iteration-1)),1:
    iteration:length(trappingfreq)-iteration+1)';

for i = 1:n2 %For images after expansion

    tokens = regexp(file_list2(i,:),  '(\(Trap Freq\.\_\d\.\d\)\(Scope Trig_0\
        .0\)\d\d\d\d\d)|(\(Trap Freq\.\_\d\.\d\d\)\(Scope Trig_0\.0\)\d\d\d\d\d
        ).bmp', 'tokens');

    if ~isempty(tokens)
        fn2 = fullfile(cd,'Sweep5ms',file_list2(i,:)); %Image directory
        imagesfinal(i,:,:) = imread(fn2); %Reads image into array
    end
end

%%%%%% Fitting the cross section profile of dark image
j = 250;
columnstart = j; %Starting column of integration
columnend = j+10; %Ending column of integration
ydark = transpose(sum(dark_image(:,columnstart:columnend),2)); %integration
x = linspace(1,dim1,dim1);
fdark = fit(x.',ydark.','gauss1'); %Fitting Gaussian to cross section
coeffvalsdark = coeffvalues(fdark);
darkcenter = coeffvalsdark(2); %Extracting center of Gaussian

%%%%%%Removing background of images through modelling and fitting Gaussian to
    the cloud profile
%%%%%For the absorption images before expansion
for i = 1:n1
    tokens = regexp(file_list1(i,:), '(\(Trap Freq\.\_\d\.\d\)\(Scope Trig_1\.0
        \)\d\d\d\d\d)|(\(Trap Freq\.\_\d\.\d\d\)\(Scope Trig_1\.0\)\d\d\d\d\d)
        .bmp', 'tokens');
    if ~isempty(tokens)
            k1 = squeeze(imagesinitial(i,:,:));
            y1 = transpose(sum(k1(:,columnstart:columnend),2)); %integration
            y1end = y1(single(dim1-150):dim1);  %Taking only the last 150
                pixels
            xend = linspace(double(dim1-150),dim1,151);
            options = fitoptions(strcat('a1*exp(-((x-',num2str(darkcenter),')/
                c1)^2)'), 'StartPoint', [coeffvalsdark(1) coeffvalsdark(3)]); %
                Parameter starting point of background fits
            f1 = fit(xend.',y1end.',strcat('a1*exp(-((x-',num2str(darkcenter),'
                )/c1)^2)'), options);   %Forcing background model to have same
                center as model of dark image
            imagesnobg = transpose(f1(x) - y1.'); %Subtracting image from
                background model
            gauss1options = fitoptions('gauss1', 'lower', [0 0 0]);
            f1nobg = fit(x.',imagesnobg.','gauss1', gauss1options); %Fitting
                Gaussian to cloud profile
            coeffvals1 = coeffvalues(f1nobg);
            sigmainitial(i,:) = coeffvals1(3); %Extracting width of fitted
                Gaussian
            integrateinitial(i,:) = sum(f1nobg(x)); %Integrating over Gaussian
    end
end
sigmainitialstd = arrayfun(@(i) std(sigmainitial(i:i+iteration-1)),1:iteration:
    length(sigmainitial)-iteration+1)'; %Average Gaussian widths
sigmainitialaveraged = arrayfun(@(i) nanmean(sigmainitial(i:i+iteration-1)),1:
    iteration:length(sigmainitial)-iteration+1)'; %Standard deviation of
```

```
    Gaussian widths
integrateinitialaveraged = arrayfun(@(i) nanmean(integrateinitial(i:i+iteration
    -1)),1:iteration:length(integrateinitial)-iteration+1)'; %Average integral
    of Gaussians
integrateinitialstd = arrayfun(@(i) std(integrateinitial(i:i+iteration-1)),1:
    iteration:length(integrateinitial)-iteration+1)'; %Standard deviation of
    integrals



%%%%%The above is repeated for the expanded absorption images below
for i = 1:n2

    tokens = regexp(file_list2(i,:),  '(\(Trap Freq\.\_\d\.\d\)\(Scope Trig_0\
        .0\)\d\d\d\d\d)|(\(Trap Freq\.\_\d\.\d\d\)\(Scope Trig_0\.0\)\d\d\d\d\d
        ).bmp', 'tokens');

    if ~isempty(tokens)

            k2 = squeeze(imagesfinal(i,:,:));
            y2 = transpose(sum(k2(:,columnstart:columnend),2));
            y2end = y2(single(dim1-150):dim1);
            xend = linspace(double(dim1-150),dim1,151);
            options = fitoptions(strcat('a1*exp(-((x-',num2str(darkcenter),')/
                c1)^2)'), 'StartPoint', [coeffvalsdark(1) coeffvalsdark(3)]);
            f2 = fit(xend.',y2end.',strcat('a1*exp(-((x-',num2str(darkcenter),'
                )/c1)^2)'), options);
            imagesnobgf = transpose(f2(x) - y2.');
            gauss1options = fitoptions('gauss1', 'lower', [0 0 0]);
            f2nobg = fit(x.',imagesnobgf.','gauss1', gauss1options);
            coeffvals2 = coeffvalues(f2nobg);
            sigmafinal(i,:) = coeffvals2(3);
            integratefinal(i,:) = sum(f2nobg(x));
    end
end

sigmafinalstd = arrayfun(@(i) std(sigmafinal(i:i+iteration-1)),1:iteration:
    length(sigmafinal)-iteration+1)';
sigmafinalaveraged = arrayfun(@(i) nanmean(sigmafinal(i:i+iteration-1)),1:
    iteration:length(sigmafinal)-iteration+1)';
integratefinalaveraged = arrayfun(@(i) nanmean(integratefinal(i:i+iteration-1))
    ,1:iteration:length(integratefinal)-iteration+1)';
integratefinalstd = arrayfun(@(i) std(integratefinal(i:i+iteration-1)),1:
    iteration:length(integratefinal)-iteration+1)';
nsigma = min(length(sigmainitialaveraged),length(sigmafinalaveraged)); %The
    number of unrepeated measurements

for i = 1:nsigma

    Temperature(i,:) = ((1.4192261*10^(-25))/(1.38064852*10^(-23)))*((
        sigmafinalaveraged(i)*calibration)^2 - (sigmainitialaveraged(i)*
        calibration)^2)/((finaltime-initialtime)^2); %Temperature calculation

end

Temperature(Temperature<0)=0; %Removing temperature values that make no sense
    for images that have weak absorption signal

%%%%%%Pushing all the raw values into a csv filed
```

```
ndata = length(trappingfreq);
datamatrix = zeros(ndata,6);
%datamatrix(:,1) = trappingamp;  %Used for multiparameter sweeps
datamatrix(:,2) = trappingfreq;
datamatrix(:,3) = integrateinitial;
datamatrix(:,4) = integratefinal;
datamatrix(:,5) = sigmainitial;
datamatrix(:,6) = sigmafinal;
csvwrite('Parameterraw.csv',datamatrix); %Csv file name

%%%%%%Pushing all the averaged values into a csv filed
ndataav = length(trappingfreqmean);
datamatrix1 = zeros(ndataav,11);
%datamatrix1(:,1) = trappingampmean;
datamatrix1(:,2) = trappingfreqmean;
datamatrix1(:,3) = integrateinitialaveraged;
datamatrix1(:,4) = integrateinitialstd;
datamatrix1(:,5) = integratefinalaveraged;
datamatrix1(:,6) = integratefinalstd;
datamatrix1(:,7) = sigmainitialaveraged;
datamatrix1(:,8) = sigmainitialstd;
datamatrix1(:,9) = sigmafinalaveraged;
datamatrix1(:,10) = sigmafinalstd;
datamatrix1(:,11) = Temperature;
csvwrite(strcat('Parametermean.csv'),datamatrix1); %Csv file name
```

Appendix B

Parameter sweeps of Rb-85

Below are plots of the two dimensional parameter sweeps in Trapping frequency detuning and repump intensity on a cloud of Rb-85 atoms similar to the ones done to Rb-87 in chapter 7.

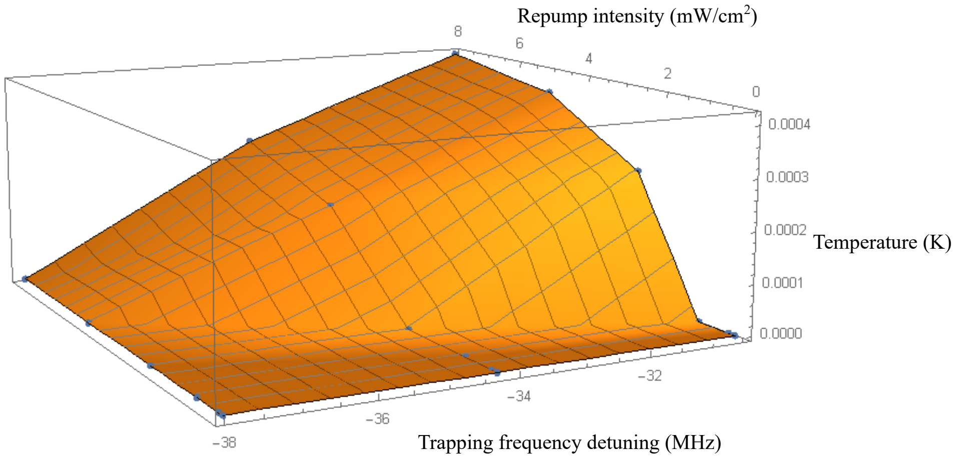

Figure B.1: Two dimensional parameter sweep of trapping frequency and repump intensity on MOT temperature for a cloud of Rb-85 atoms.

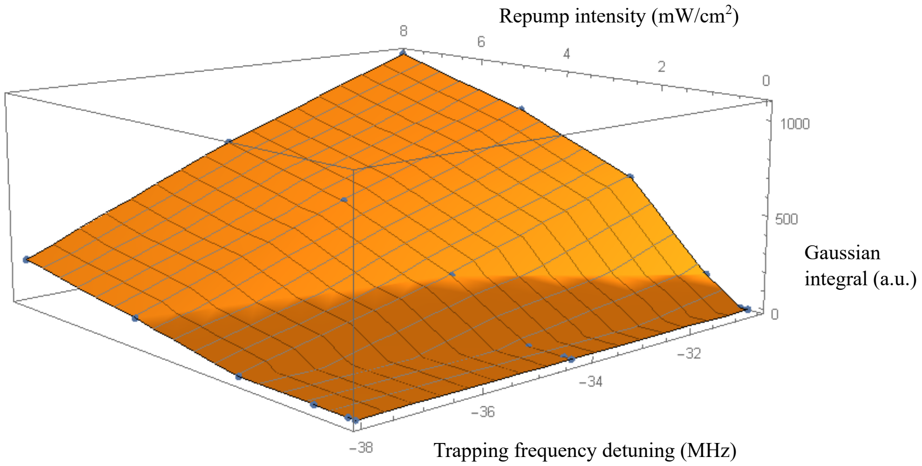

Figure B.2: Two dimensional parameter sweep of trapping frequency and repump intensity on MOT density for a cloud of Rb-85 atoms.